

The Structure of the Interstellar Medium of Star Forming Galaxies

Philip F. Hopkins^{*}¹, Eliot Quataert¹, & Norman Murray^{2,3}

¹*Department of Astronomy and Theoretical Astrophysics Center, University of California Berkeley, Berkeley, CA 94720*

²*Canadian Institute for Theoretical Astrophysics, 60 St. George Street, University of Toronto, ON M5S 3H8, Canada*

³*Canada Research Chair in Astrophysics*

Submitted to MNRAS, October 14, 2011

ABSTRACT

We develop and implement numerical methods for including stellar feedback in galaxy-scale numerical simulations. Our models include simplified treatments of heating by Type-I and Type-II supernovae, gas recycling from young stars and AGB winds, heating from the shocked stellar winds, HII photoionization heating, and radiation pressure from stellar photons. The energetics and time-dependence associated with the feedback are taken directly from stellar evolution models. We implement these stellar feedback models in smoothed particle hydrodynamic simulations with pc-scale resolution, modeling galaxies from SMC-like dwarfs and Milky-way analogues to massive $z \sim 2$ star forming disks. Absent stellar feedback, gas cools rapidly and collapses without limit into dense sub-units, inconsistent with observations. By contrast, in all cases with feedback, the interstellar medium (ISM) quickly approaches a statistical steady state in which giant molecular clouds (GMCs) continuously form, disperse, and re-form, leading to a multi-phase ISM. In this paper, we quantify the properties of the ISM and GMCs in this self-regulated state. In a companion paper we study the galactic winds driven by stellar feedback.

Our primary results on the structure of the ISM in star forming galaxies include:

1) Star forming galaxies generically self-regulate so that the cool, dense gas maintains Toomre's $Q \sim 1$. Most of the volume is occupied by relatively diffuse hot gas, while most of the mass is in dense GMC complexes created by self-gravity. The phase structure of the gas and the gas mass fraction at high densities are much more sensitive probes of the physics of stellar feedback than integrated quantities such as the Toomre Q or gas velocity dispersion.

2) Different stellar feedback mechanisms act on different spatial (and density) scales. Radiation pressure and HII gas pressure are critical for preventing runaway collapse of dense gas in GMCs. Shocked supernovae ejecta and stellar winds dominate the dynamics of the volume-filling hot gas. However, this gas primarily vents out of the star-forming disk and contributes only modestly to the mid-plane ISM pressure.

3) The galaxy-averaged star formation rate is determined by feedback, with different mechanisms dominating in different galaxy types. For a given feedback efficiency, restricting star formation to molecular gas or modifying the cooling function has little effect on the star formation rate in the galaxies we model (including an SMC-mass dwarf). By contrast, changing the feedback mechanisms or assumed feedback efficiencies directly translates to shifts off of the observed Kennicutt-Schmidt relation.

4) Self-gravity leads to GMCs with an approximately self-similar mass function $\propto M^{-2}$, with a high mass cutoff determined by the characteristic Jeans/Toomre mass of the system. In all of our galaxy models, GMCs live for a few dynamical times before they are disrupted by stellar feedback. The net star formation efficiency in GMCs ranges from $\sim 1\%$ in dwarfs and MW-like spirals to nearly $\sim 10\%$ in gas-rich rapidly star forming galaxies. GMCs are approximately virialized, but there is a large dispersion in the virial parameter for a given GMC mass and lower mass GMCs tend to be preferentially unbound.

Key words: galaxies: formation — star formation: general — galaxies: evolution — galaxies: active — cosmology: theory

1 INTRODUCTION

The Kennicutt-Schmidt (KS) law for star formation in galaxies implies a gas consumption time of ~ 50 dynamical times (Kennicutt 1998); comparably long gas consumption times are inferred even on the scale of giant molecular clouds (GMCs) and other dense

* E-mail: phopkins@astro.berkeley.edu

Table 1. Galaxy Models

Model	ϵ_g [pc]	m_i [M_\odot]	M_{halo} [M_\odot]	c	V_{max} [km s^{-1}]	M_{bary} [M_\odot]	M_b [M_\odot]	a [kpc]	M_d [M_\odot]	r_d [kpc]	h [pc]	M_g [M_\odot]	r_g [kpc]	f_{gas}	t_{dyn} [Myr]
HiZ	3.5	1700	1.4e12	3.5	230	1.07e11	7e9	1.2	3e10	1.6	130	7e10	3.2	0.49	12
Sbc	2.5	130	1.5e11	11	86	1.05e10	1e9	0.35	4e9	1.3	320	5.5e9	2.6	0.36	22
MW	2.5	220	1.6e12	12	190	7.13e10	1.5e10	1.0	4.73e10	3.0	300	0.9e10	6.0	0.09	31
SMC	0.7	25	2.0e10	15	46	8.9e8	1e7	0.25	1.3e8	0.7	140	7.5e8	2.1	0.56	45

Parameters describing our galaxy models, used as the initial conditions for all of the simulations:

(1) Model name: shorthand for models of a high-redshift massive starburst (**HiZ**); local gas-rich galaxy (**Sbc**); MW-analogue (**MW**); and isolated SMC-mass dwarf (**SMC**). (2) ϵ_g : gravitational force softening in our highest-resolution simulations. (3) m_i : gas particle mass in our highest-resolution simulations. New star particles formed have mass = $0.5 m_i$, disk/bulge particles $\approx m_i$, and dark matter halo particles $\approx 5 m_i$. (4) M_{halo} : halo mass. (5) c : halo concentration. Values lie on the halo mass-concentration relation at the appropriate redshift ($z = 0$ for SMC, Sbc, and MW; $z = 2$ for HiZ). (6) V_{max} : halo maximum circular velocity. (7) M_{bary} : total baryonic mass. (8) M_b : bulge mass. (9) a : Hernquist (1990) profile scale-length for bulge. (10) M_d : stellar disk mass. (11) r_d : stellar disk scale length. (12) h : stellar disk scale-height. (13) M_g : gas disk mass. (14) r_g : gas disk scale length (gas scale-height determined so that $Q = 1$). (15) f_{gas} : average gas fraction of the disk inside of the stellar R_e ($M_g[< R_e]/(M_g[< R_e] + M_d[< R_e])$). The total gas fraction, including the extended disk, is $\sim 50\%$ larger. (15) t_{dyn} : gas disk dynamical time at the half-gas mass radius.

star-forming regions (e.g. Krumholz & Tan 2007). Moreover, the total fraction of the gas turned into stars in GMCs over their lifetime is only a few percent (Zuckerman & Evans 1974; Williams & McKee 1997; Evans 1999; Evans et al. 2009). By contrast, absent stellar feedback, GMCs experience runaway collapse to densities much higher than observed, and eventually turn a near-unity fraction of their gas into stars (Hopkins et al. 2011a; Tasker 2011; Bournaud et al. 2010; Dobbs et al. 2011; Krumholz et al. 2011; Harper-Clark & Murray 2011). An analogous problem occurs in cosmological models of galaxy evolution without strong stellar feedback: gas cools efficiently, collapsing into clumps that runaway to high densities on a few dynamical times and produce an order of magnitude more stars than is observed (e.g. Katz et al. 1996; Somerville & Primack 1999; Cole et al. 2000, and references therein).

Neither thermal pressure nor turbulence in and of itself can stave off collapse in the ISM: cooling is rapid, so that thermal support is quickly lost, and turbulent support dissipates on a single crossing time (e.g., Ostriker et al. 2001). Some mechanism must therefore continuously inject energy and momentum into the gas on both GMC and galactic scales, in order to prevent runaway collapse to arbitrarily high densities. Moreover, it is not enough to simply slow down the collapse of gas; if that were the case, the gas would eventually turn into stars on long timescales. Instead, mass must actually be expelled from both GMCs and galaxies as a whole.

A number of physical mechanisms have been proposed as sources of random motions in the ISM and GMCs: these include photo-ionization, stellar winds, radiation pressure from both UV and IR photons, proto-stellar jets, cosmic-rays created in supernova shocks, and supernovae themselves (this is not an exhaustive list!). An alternative class of models suggests that the turbulence is not explicitly produced by star formation, but comes from gravitational cascades from larger scales or instabilities that can tap into the differential rotation in galaxies. (see e.g. Mac Low & Klessen 2004; McKee & Ostriker 2007, and references therein, for reviews of ISM turbulence and stellar feedback).

Making a realistic comparison between models of the ISM and observations ultimately requires numerical simulations, since the systems of interest are highly non-linear, chaotic, and time-dependent, with a large number of competing physical processes and a huge dynamic range in space and time. However, most numerical experiments have traditionally been restricted to idealized simulations of single star-forming regions or sub-regions of single GMCs. There are good reasons for doing so, since these

calculations are critical for studying the physics of star formation. They cannot, however, address a large number of observational constraints such as the balance of phases in the ISM; the origin of the *global* Schmidt-Kennicutt relation; and observations of GMC/galaxy scaling relations, such as mass functions and the linewidth-size relation. Likewise, the lifetimes of GMCs and their internal structure cannot be addressed in detail without a model that self-consistently incorporates continuous GMC formation, dissolution, and re-formation. In short, addressing these questions requires *galaxy-scale* simulations that also self-consistently follow feedback from sub-GMC through super-galactic scales.

There are at least two major challenges that numerical simulations must confront to model feedback and GMC-level phase structure explicitly. First, simulations must actually resolve the formation of GMCs and the phase structure of the ISM (spatial resolution ~ 1 pc; although in massive gas-rich galaxies GMCs can be much larger, \sim kpc in size). Numerical simulations of isolated galaxies, galaxy mergers, and cosmological “zoom-in” simulations of individual halos can now reach this resolution, but it remains prohibitive in full cosmological simulations.

The second challenge facing simulations is that a wide range of processes appear to be important sources of feedback and turbulence in the ISM of galaxies: e.g., protostellar jets, HII regions, stellar winds, radiation pressure from young stars, and supernovae. It is therefore unlikely that the full problem, which spans many orders of magnitude in spatial, mass, and time scales, can be treated with just a single simple prescription, without including multiple physical processes. In particular the physics of the dense ISM is clearly very different from that of the diffuse ISM, and different feedback processes likely dominate in each case. Thus far, however, many calculations that model stellar feedback explicitly have invoked *only* thermal heating via supernovae (e.g. Thacker & Couchman 2000; Governato et al. 2007; Ceverino & Klypin 2009; Teyssier et al. 2010; Colín et al. 2010; Avila-Reese et al. 2011; Pilkington et al. 2011). The thermal energy, however, tends to be rapidly radiated away, especially in dense sub-regions of GMCs. Perhaps even more importantly, the actual time required for SNe to explode (a few Myr) is *longer* than the observed “lifetime” of low-mass GMCs and so supernovae cannot be the dominant mechanism unbinding GMCs in local galaxies (Evans et al. 2009).

In Hopkins et al. (2011a) (hereafter Paper I) we developed a new numerical model for the effects of the momentum injection from massive stars on small scales in star-forming regions. Us-

ing galaxy-scale simulations with pc-scale resolution to resolve the formation of individual GMCs, we accounted (approximately) for the momentum deposited as gas and dust in the vicinity of young stars absorbs the stellar radiation. We showed that this feedback mechanism alone can dramatically suppress runaway star formation, disrupting collapsing GMCs once a few percent of their mass is turned into stars, and naturally producing galaxies on the observed Schmidt-Kennicutt relation. This is, however, just a first step towards a more complete model of the ISM.

In this paper, we therefore extend the models in Paper I to include HII photo-ionization heating and the momentum injection, gas heating (energy injection) and mass recycling from supernovae (Types I and II) and stellar winds (both early fast winds and late, AGB winds).¹ We also extend the radiation pressure model to include not just the small-scale radiation pressure force from multiply-scattered IR photons in GMCs, but also the long-range radiation pressure force produced by the diffuse interstellar UV through IR radiation field. Our models of these feedback processes are physically motivated and tied to stellar evolution calculations; they are, however, also necessarily simplified and approximate given the range of spatial scales and processes we consider. In addition to an improved treatment of stellar feedback, we also extend our cooling and star formation models to include explicit models for molecular chemistry, allowing for the suppression of star formation via photo-dissociation and inefficient molecule formation. These are all processes that have been discussed analytically in the literature, and in some cases explored in idealized simulations that focus on an individual physical effect. However, by including all of these processes together, our study allows us to assess the relative importance of different feedback mechanisms and the interplay between the different feedback and star formation processes in a given galaxy model. Towards this end, we have implemented this star formation and feedback physics in a range of idealized, observationally-motivated galaxy models that span low-redshift dwarfs, Milky Way-like systems, and nearby starbursts through to extremely massive, high-redshift starburst galaxies.

The remainder of this paper is organized as follows. In §2 we describe the galaxy models and our method of implementing feedback from the various mechanisms outlined above. The Appendix contains tests of the numerical methods. In §3 we discuss how each feedback mechanism singly and in combination effects the observed galaxy morphologies in both gas and stars, for a range of different galaxy properties. In §4 we consider the star formation histories of each model and show how they are influenced by each feedback mechanism separately and in concert. We investigate the role of molecular chemistry in §5 and show that it has little effect on galaxy properties or global star formation (for the galaxy models we consider). We examine the global properties of the ISM in §6, including gas disk velocity dispersions, scale heights, and Toomre parameters, and we illustrate how different feedback mechanisms contribute to supporting turbulence and maintaining marginal disk stability. We consider the phase structure of the ISM in §7, and show how the presence of these feedback mechanisms together naturally gives rise to a multi-phase ISM (with cold molecular, warm ionized, and hot diffuse components). In §8 we examine the properties of the cold dense gas in the simulated GMC population: GMC mass functions, densities, velocity dispersions and scaling laws, virial parameters, lifetimes, and star formation effi-

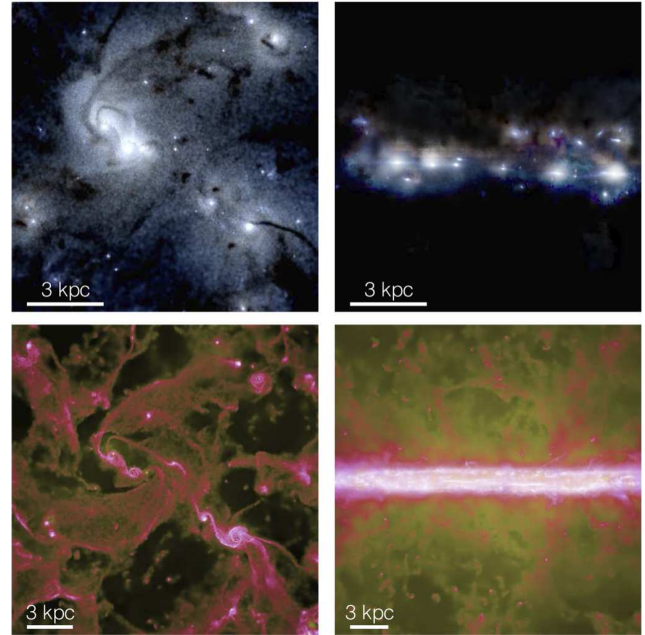


Figure 1. Morphology of the gas and stars in a standard simulation of a HiZ disk model, a massive, $z \sim 2-4$ starburst disk with $\dot{M}_* > 100 M_\odot \text{ yr}^{-1}$, with all feedback mechanisms enabled. The images are shown at ~ 2 orbital times after the beginning of the simulation when the disk is in a feedback-regulated steady-state. We show face-on (*left*) and edge-on (*right*) projections. *Top:* Stars. The image is a mock *ugr* (SDSS-band) composite, with the spectrum of all stars calculated from their known age and metallicity, and dust extinction/reddening accounted for from the line-of-sight dust mass. The brightness follows a logarithmic scale with a stretch of ≈ 2 dex. *Bottom:* Gas. Brightness encodes projected gas density (logarithmically scaled with a ≈ 4 dex stretch); color encodes gas temperature with blue being $T \lesssim 1000$ K molecular gas, pink $\sim 10^4 - 10^5$ K warm ionized gas, and yellow $\gtrsim 10^6$ K hot gas. Gravitational collapse forms massive kpc-scale star cluster complexes that give rise to the clumpy morphology (edge on, similar to “clump-chain” galaxies) that is further enhanced in the optical by patchy extinction. Violent outflows are present, emerging both from the complexes and the disk as a whole, driven by the massive starburst. These outflows maintain a thick gas disk and disrupt many of the clumps, which continuously re-form.

ciencies. We compare each of these properties to observations and show how they are affected by the presence or absence of different feedback mechanisms. Finally, in §9 we summarize our results and discuss their implications.

These results presented in this paper provide an explanation for disruption of GMCs and the observed slow rate of star formation in galaxies, but they do not address the question of why galaxies have a baryon fraction well below that of the universe as a whole. In a companion paper we show that the combined effects of radiation pressure and supernovae drive powerful galaxy scale winds, ejecting baryons from star forming galaxies.

2 THE SIMULATIONS

The initial conditions and numerical details of the simulations used here are described in detail in Paper I (see their Section 2 and Tables 1-3). However we briefly summarize some basic properties of the models here. The simulations were performed with the parallel Tree-SPH code GADGET-3 (Springel 2005). They include stars, dark matter, and gas, with cooling, shocks, star formation, and stellar feedback.

¹ Movies of these simulations are available at <https://www.cfa.harvard.edu/~phopkins/Site/Research.html>

Table 2. Feedback Physics for Simulations Used in This Paper

Simulation Name	Physics Included						
	Star Formation & Molecular Gas	Gas Cooling	Mass Recycling (SNe & Winds)	Radiation Pressure (Local/Long-Range)	SNe (Types I & II) (Energy/Momentum)	Stellar Winds (Energy/Momentum)	HII Photo- Ionization
Standard	✓	✓	✓	✓/✓	✓/✓	✓/✓	✓
No Feedback	✓	✓	✓	×/×	×/×	×/×	×
No Feedback or SF	×	✓	×	×/×	×/×	×/×	×
No Heating	✓	✓	✓	✓/✓	×/✓	×/✓	×
No Rad. Mom.	✓	✓	✓	×/×	✓/✓	✓/✓	✓
Rad. Mom. Only	✓	✓	✓	✓/✓	×/×	×/×	×
No Stellar Wind	✓	✓	✓	✓/✓	✓/✓	×/×	✓
No HII Heating	✓	✓	✓	✓/✓	✓/✓	✓/✓	×
Molecular Model A	Mod	✓	✓	✓/✓	✓/✓	✓/✓	✓
Molecular Model B	✓	✓	✓	✓/✓	✓/✓	✓/✓	✓
Molecular Model C	Mod	Mod	✓	✓/✓	✓/✓	✓/✓	✓
Enforced SED (§ A)	✓	✓	✓	✓/Mod	✓/✓	✓/✓	✓
Paper I Simulations	Mod	✓	×	✓/×	×/×	×/×	×

Summary of the physics included or excluded in the simulations shown throughout this paper. The implementation of each set of physics is described in § 2. A ✓ means the given “module” was included, × means it was excluded. Mod=“Modified” runs are described in the text. The Enforced SED models modify the calculation of the long-range radiation pressure and are discussed in the Appendix. Paper I simulations use the SF model of Molecular Model A.

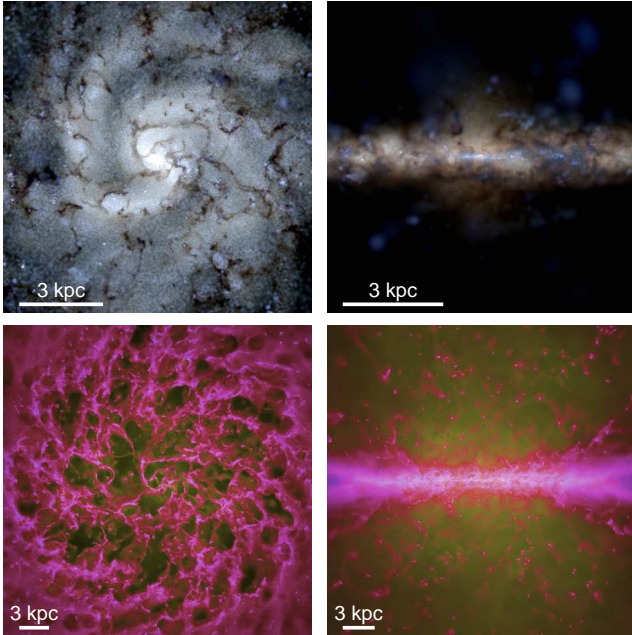


Figure 2. Stellar and gas images as in Figure 1, but for the Sbc model, a dwarf starburst galaxy. The disk is again clumpy, but the clumps are relatively much smaller than those in the HiZ model, and do not gravitationally dominate – the global disk structure more clearly traces spiral structure albeit with a disturbed, filamentary and irregular pattern in the gas. There is a stellar bar in the central few kpc and a bright starburst, but the disk is quite dusty, especially edge-on. Strong outflows arise from the central few kpc, producing a clumpy, multi-phase wind.

Gas follows a standard atomic cooling curve but in addition can cool to $< 100\text{K}$ via fine-structure cooling. This allows it to collapse to very high densities, and star formation occurs in dense regions above a threshold $n > 1000\text{cm}^{-3}$, with a rate $\dot{\rho}_* = \epsilon \rho / t_{\text{ff}}$ where t_{ff} is the free-fall time and $\epsilon = 1.5\%$ is an efficiency taken from observations of star-forming regions with the same densities (Krumholz & Tan 2007, and references therein). In Paper I we show

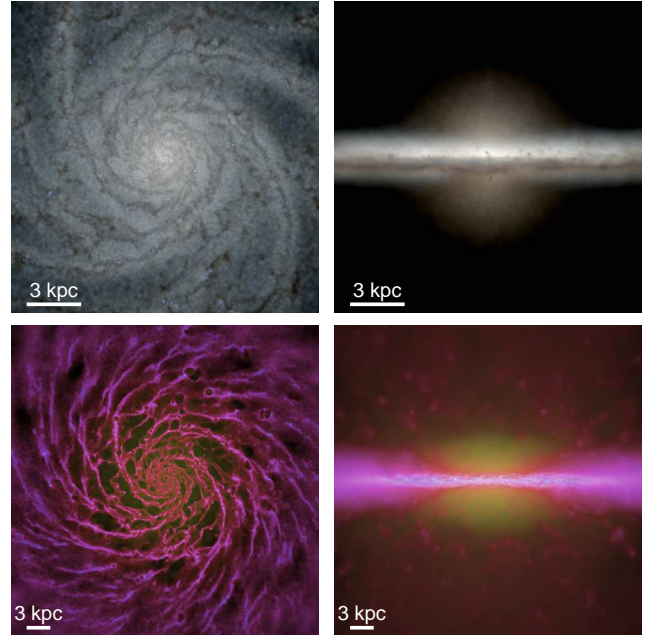


Figure 3. Stellar and gas images as in Figure 1, but for the Milky Way model. These images are for a model with a slightly higher dark matter fraction than our standard MW model, such that a bar does not form. The resulting morphology in gas and stars is a canonical spiral (compare e.g. M101), with dust lanes along the spiral arms, flocculent morphology and features such as spurs/feathers in the outer arms. The star formation is still concentrated in star clusters (visible as small blue knots, largely along the arms) – but these are relatively much smaller than the giant clumps in Figure 1, owing to the much smaller Jeans mass. SNe-driven bubbles/holes are clear in the outer gas disk.

that the equilibrium structure and SFR are basically independent of the small-scale star formation law (robust to order-of-magnitude variations in the threshold and efficiency, and changes in the power-law index $\dot{\rho} \propto \rho^{1-2}$) because it is feedback-regulated (so clumps simply form stars until sufficient feedback halts further collapse).

The feedback models are implemented in four distinct initial

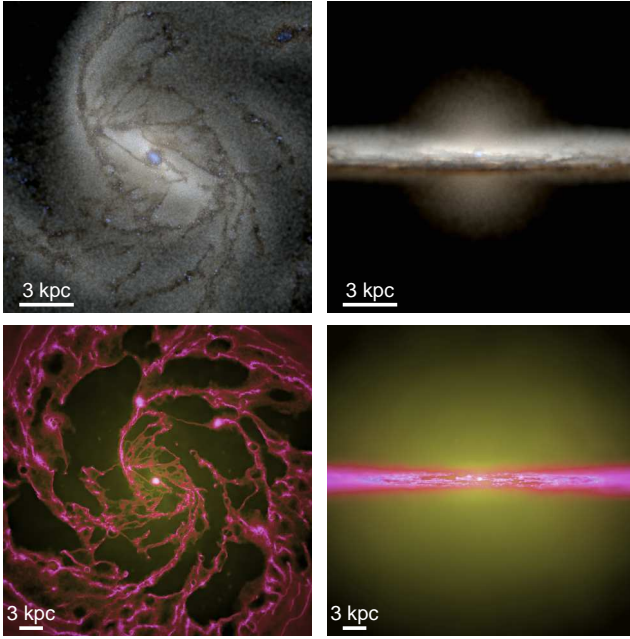


Figure 4. Stellar and gas images for our standard Milky Way model after it develops a strong bar (compare with Fig. 3, which is our MW model for a somewhat higher dark matter halo mass, which does not develop a bar). The morphology is that of a typical barred spiral (compare e.g. NGC1097). Star cluster formation is enhanced along the bar, with a small nuclear concentration of star formation driven by inflows along the bar.

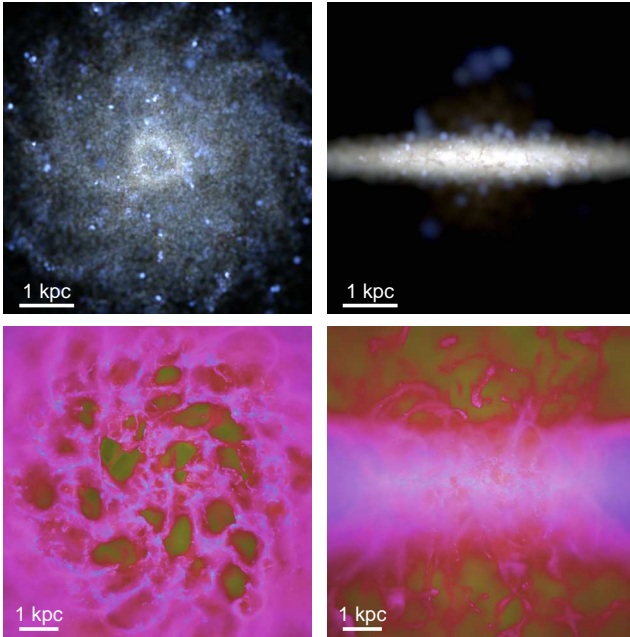


Figure 5. Stellar and gas images as in Figure 1, but for the SMC model, an isolated SMC-mass dwarf galaxy. The morphology is here that of an irregular galaxy, with a puffy/thick disk of mostly ionized gas, irregularly distributed star formation, and large SNe bubbles driven by overlapping SNe explosions. Despite a very low absolute star formation rate, a wind is plainly evident with a mix of hot gas and entrained cold/warm material, with various filaments/loops/arcs driven by the hot gas bubbles as well as directly venting hot gas.

disk models, designed to represent a range of characteristic galaxy types. Each initial disk has a bulge, stellar and gaseous disk, halo, and central BH (although to isolate the role of stellar feedback, models for BH growth and feedback are disabled); they are initialized in equilibrium so that in the absence of cooling, star formation, and feedback there are no significant transients. The gaseous disk is initially vertically pressure-supported, but this cools away in much less than a dynamical time and the emergent vertical structure depends on feedback (changing the initial support to turbulent dispersion does not change our results). Our “low” resolution runs (used to evolve the simulations for several Gyr, to ensure steady-state behavior) use $\approx 3 \times 10^6$ particles, with $\approx 10^6$ particles in the disk, giving SPH smoothing lengths of ~ 10 pc in the central few kpc of a MW-like disk (scaling linearly with the disk size/mass scale). Our “standard” resolution cases use ~ 30 times as many particles, and correspondingly reach up to $\sim 1 - 5$ pc smoothing lengths and particle masses of $500 M_\odot$, and are run for a few orbital times each. A couple of ultra-high resolution runs used for convergence tests employ $\sim 10^9$ particles, with sub-pc resolution on kpc scales.

The disk models include:

(1) SMC: an SMC-like dwarf, with baryonic mass $M_{\text{bar}} = 8.9 \times 10^8 M_\odot$ and halo mass $M_{\text{halo}} = 2 \times 10^{10} M_\odot$ (concentration $c = 15$), a Hernquist (1990) profile bulge with mass $m_b = 10^7 M_\odot$, and exponential stellar ($m_d = 1.3 \times 10^8 M_\odot$) and gas disks ($m_g = 7.5 \times 10^8 M_\odot$) with scale-lengths $h_d = 0.7$ and $h_g = 2.1$ kpc, respectively. Table 1 gives the maximum circular velocity. The initial scale-height is $z_0 = 140$ pc and the stellar disk is initialized such that the Toomre $Q = 1$ everywhere.

(2) MW: a MW-like galaxy, with halo (M_{halo}, c) = $(1.6 \times 10^{12} M_\odot, 12)$, and baryonic ($M_{\text{bar}}, m_b, m_d, m_g$) = $(7.1, 1.5, 4.7, 0.9) \times 10^{10} M_\odot$ with scale-lengths (h_d, h_g, z_0) = $(3.0, 6.0, 0.3)$ kpc.

(3) Sbc: a LIRG-like galaxy (i.e. a more baryon-dominated gas-rich spiral characteristic of those observed at low redshifts), with halo (M_{halo}, c) = $(1.5 \times 10^{11} M_\odot, 11)$, and baryonic ($M_{\text{bar}}, m_b, m_d, m_g$) = $(10.5, 1.0, 4.0, 5.5) \times 10^9 M_\odot$ with scale-lengths (h_d, h_g, z_0) = $(1.3, 2.6, 0.13)$ kpc.

(4) HiZ: a high-redshift massive starburst disk, chosen to match the properties of the observed non-merging but massively star-forming SMG population, with halo (M_{halo}, c) = $(1.4 \times 10^{12} M_\odot, 3.5)$ and a virial radius appropriately rescaled for a halo at $z = 2$ rather than $z = 0$, and baryonic ($M_{\text{bar}}, m_b, m_d, m_g$) = $(10.7, 0.7, 3, 7) \times 10^{10} M_\odot$ with scale-lengths (h_d, h_g, z_0) = $(1.6, 3.2, 0.32)$ kpc.

The salient galaxy properties are summarized in Table 1, reproduced from Paper I. The feedback and ISM physics we include in different runs is summarized in Table 2.

2.1 Stellar Feedback

2.1.1 Local Momentum Flux from Radiation Pressure, Supernovae, & Stellar Winds

First, we consider the radiation pressure produced on a sub-GMC scale from young star clusters. This feedback mechanism is that presented and discussed extensively in Paper I, but we briefly summarize its properties here. At each timestep, gas particles identify the nearest density peak (via a friends-of-friends algorithm averaged over a scale of a couple smoothing lengths), representing the center of the nearest star-forming “clump” or GMC-analog. The gas then lies at some point \mathbf{R}_{cl} from the cloud center. The summed luminosity from the simulation star particles inside the radius $L(<$

R_{cl}) is determined from each star’s known age and metallicity according to the STARBURST99 model (Leitherer et al. 1999). Assuming this is equally distributed to all gas inside the cloud, the rate of momentum deposition is then just $\dot{P}_{\text{rad}} \approx (1 + \tau_{\text{IR}})L_{\text{incident}}/c$, where the term $1 + \tau_{\text{IR}}$ accounts for the fact that most of the initial optical/UV radiation is absorbed and re-radiated in the IR; $\tau_{\text{IR}} = \Sigma_{\text{gas}} \kappa_{\text{IR}}$ is the optical depth in the IR, which allows for the fact that the momentum is boosted by multiple scatterings in optically thick regions. Here Σ_{gas} is calculated as the local optical depth towards the identified clump, with $\kappa_{\text{IR}} \approx 5 (Z/Z_{\odot}) \text{g}^{-1} \text{cm}^2$ approximately constant over the relevant physical range of dust temperatures. The imparted acceleration is directed away from the clump, along \mathbf{R}_{cl} . There is *no* “free-streaming” or “turnoff” of cooling or other physics for particles affected by the feedback. For a detailed discussion of the normalization, resolution effects, effects of photon “leakage,” and choice of whether the momentum is applied as a continuous acceleration or discrete “kicks,” we refer to Paper I, but note that essentially all of our conclusions are robust to these and other small variations in the model implementation.

There is also direct momentum injection from supernovae, stellar winds, and protostellar jets. We include this in the same manner, but with the appropriate momentum injection rates using $\dot{P} = \dot{P}_{\text{rad}} + \dot{P}_{\text{SNe}} + \dot{P}_{\text{w}}$, where $\dot{P}_{\text{SNe}}(t, Z)$ and $\dot{P}_{\text{w}}(t, Z)$ are tabulated as a function of time and metallicity for each star particle from STARBURST99. We emphasize that this is the direct momentum from ejecta only – where SNe are important, they typically impart much greater momentum from pressure-driven expansion of hot regions, which we wish to model directly. The direct ejecta momentum of SNe and stellar winds are usually small relative to the radiation pressure (they have a magnitude $\sim L/c$, but do not receive the “boost” of $\sim \tau_{\text{IR}}$, which is typically at least a few in GMCs). The contribution from protostellar jets can in principle also be added explicitly, but when integrated over the IMF, their contribution is $\sim 10 - 20\%$ that from stellar winds alone; protostellar jets are probably important in regions of low-mass star formation, but they have little global effect relative to the contribution of massive stars.

2.1.2 Supernova Shock-Heating

In addition to providing momentum in ejecta, the gas shocked by supernovae can be heated to high temperatures, generating bubbles and filaments of hot gas; the resulting over-pressurized regions can then hydrodynamically accelerate nearby gas. The model in § 2.1.1 already accounts for the direct *momentum* of SNe ejecta; but not necessarily the full post-shock heating/energy budget (or the momentum generated by the pressure-driven expansion of bubbles). We therefore add an explicit model for this thermal heating.

We know the age, mass, and metallicity for each star particle in the simulation, so for a given timestep $t \rightarrow t + \Delta t$, we can calculate the total mechanical energy produced by Type-II SNe explosions. We do so using a pre-tabulated $E(t)$ (which we compile from the STARBURST99 package, for a Kroupa 2002 IMF; Leitherer et al. 1999). This gives an expected input ΔE . However, on very short time/mass scales SNe are discrete events with a roughly fixed individual energy, so we actually determine the expected number of SNe per star particle in a given timestep assuming a canonical $E_0 = 10^{51}$ erg per SNe, and then randomly determine the number of SNe in the timestep drawing from a Poisson distribution with the calculated expectation value; this ensures the total SNe energy comes out correctly. In fact, the time steps in our simulations are typically short enough ($\sim 100 - 1000$ yr) to resolve individual SNe events. We also include SNe Type-I, for which we adopt an empir-

ical fit to a simple “prompt+delayed” model fitted to the observed SNe rates in Mannucci et al. (2006): the prompt component is a narrow Gaussian at a few 10^7 yr, and the delayed component has a constant rate. However, since the systems we consider here are all star-forming, Type-I SNe make little difference and the energy input is dominated by the Type-II population.

We wish to explicitly resolve the energy-conserving (Sedov) phase of the resulting SNe expansion. We therefore directly deposit the SNe energy in the local SPH smoothing kernel (nearest ~ 32 neighbors), weighted by the kernel – essentially the smallest meaningful length in the simulation. In this case, there is no implicit or sub-grid assumption about even the earliest SNe expansion.²

Unlike most models of supernova feedback, we do *not* artificially turn off gas cooling after injecting thermal energy into the ambient gas. Because other feedback processes (radiation pressure, photoionization heating, etc.) typically expel the dense gas in star-forming regions back out into the more diffuse ISM prior to when SNe explode, the effects of SNe on the ISM are significantly larger than in models that only include thermal SNe feedback.

2.1.3 Gas Return and Stellar Wind Shock-Heating

Stellar evolution returns gas to the ISM from SNe and stellar winds. This is implemented following the methodology of Torrey et al. (2012), with a few minor modifications. Every star has a known age, mass, and metallicity; for a given timestep Δt we determine the total mass-loss rate of the particle (treated as a single stellar population) $\dot{M}(t)$ (tabulated from STARBURST99 for both SNe and stellar wind mass losses assuming a Kroupa IMF), which gives an expected recycled mass $\Delta M = \dot{M}(t) \Delta t$. This mass is then distributed among local gas particles in the SPH smoothing kernel, weighted by the kernel. Gas recycled in SNe ejecta is returned discretely only in SNe (to the same gas heated by those events); gas recycled by stellar winds is returned continuously (in every time step).³ Integrated over a Hubble time, the total mass fraction returned according to the tabulated models is ≈ 0.3 .

The injected/recycled gas has the same gross properties (momentum, location, etc) as the star from which it spawns. However, the initial thermal state must be specified. For the SNe ejecta the gas carries the ejecta energy discussed above. We assume that the stellar wind gas shocks, so that it has an initial specific energy

² Some other simulations (Katz et al. 1996; Stinson et al. 2006) inject the energy instead into a larger “blastwave radius” around star particles, with

$$R_E = 55 E_{51}^{0.32} n_0^{-0.16} \bar{P}_{04}^{-0.20} \text{pc} \quad (1)$$

(Chevalier & Gardner 1974; McKee & Ostriker 1977), where $E_{51} = \Delta E/10^{51}$ erg, n_0 is the density in cgs, and $\bar{P}_{04} = 10^{-4} P/[\text{erg cm}^{-3}] k_{\text{B}}^{-1}$, intended to reflect the radius of the energy-conserving (Sedov) phase of the blastwave (often much larger than our softening length). Because we wish to resolve this expansion as opposed to assuming it in sub-grid fashion, we do not use this approximation. However, we have re-run our simulations using this approximation instead of coupling the energy inside of h_{sm} . For some individual blastwaves it can make a significant difference to their expansion history, but on average the behavior is similar where the densities are low and bubbles can expand. The final statistical properties of our simulations do not depend on the injection radius within a modest range, either with this formula or adopting fixed physical radii $\sim 1 - 10$ pc and/or fixed neighbor number = 16 – 320.

³ Models in which the gas is stochastically returned by allowing an individual star particle to be turned back into a gas particle (“recycled”) with probability $p = \Delta M/m_i$ give nearly identical results, but are subject to greater shot noise, especially on sub-GMC scales.

(and corresponding entropy/temperature) set by the wind properties as a function of time. This is again tabulated from STARBURST99 as a function of age and metallicity. Integrated over their history, the winds have an energy-flux-weighted average temperature $T_w \approx 3 \times 10^7 K$, reflecting the fact that most of the energy is in early “fast” winds with speeds $\gtrsim 500 \text{ km s}^{-1}$; at late times, however, the energies and temperatures are much lower because AGB winds with velocities $\sim 10 \text{ km s}^{-1}$ dominate. As before, we do not modify the cooling or hydrodynamics of these gas particles.

2.1.4 Photoionization-Heating of HII Regions

On small scales around young stars, direct photoionization-heating by ionizing photons maintains gas in a warm $\sim 10^4 K$ ionized state, which can in principle be an important source of pressure in low-density systems. A rigorous solution for the effects of this heating would involve on-the-fly radiation transport. This is probably important for the study of the formation of the first stars and for detailed studies of GMC disruption in lower mass molecular clouds, but is more detailed than is possible given the goals of the feedback model we are developing. Moreover, as we shall show, photoionization feedback is important, but not dominant, for the more massive, evolved systems we model. We approximate the key effects of photoionization on ambient gas with the following simple model.

Each star particle produces ionizing photons at a rate \dot{N}_i , which we again tabulate as a function of the age and mass of the star particle from the STARBURST99 models. We then allow these ionizing photons to ionize a region around the star as follows. First consider the gas particle nearest the star. If it is already ionized (either because it is at sufficiently high temperature $> 10^4 K$ or because it is already a part of another HII region), we move to the next nearest gas particle. If it is not ionized, then we calculate the rate of ionizing photons needed to maintain the gas as fully ionized, as $\Delta \dot{N} = N(H)_j \beta n_e$, where $N(H)_j = M_j / \mu m_p$ is the number of atoms in the particle, $\beta \approx 3 \times 10^{-13} \text{ cm}^3 \text{ s}^{-1}$ is the recombination rate coefficient, and n_e is the average electron density of the particle when fully ionized. If $\dot{N}_i > \Delta \dot{N}_j$, the particle is tagged as being within an HII region, and the remaining photon production rate is tabulated as $\dot{N}_i \rightarrow \dot{N}_i - \Delta \dot{N}_j$. The process is then repeated for the next nearest particle. Once we reach a point where $\dot{N}_i > 0$ and $\dot{N}_i < \Delta \dot{N}_j$, we determine whether or not to ionize the particle randomly, with probability $p = \dot{N}_i / \Delta \dot{N}_j$, and consume the remaining photon budget, ending the chain.

This procedure determines the Stromgren sphere around the particle, but allows for the resolved inhomogeneous density distribution and overlapping ionized regions. In low-density regions, the ionized material can extend to very large radii; because we also account for a uniform extragalactic ionizing background, we also truncate the ionizing region if we reach a radius at which the flux density from the ionizing source falls below the ionizing background (for background flux density u_ν , this is the r where $L_\nu / 4\pi r^2 c = u_\nu$). Gas particles flagged as being within an HII region are not allowed to cool below an effective temperature $t_{\text{HII}} \approx 10^4 K$ in that timestep (i.e. until they are flagged as outside of such a region), and are immediately heated to t_{HII} if their temperature lies below this value.

Although the HII regions estimated for individual star particles can be quite small (as the stellar masses can be as low as $100 M_\odot$), this method allows for nearby star particles to generate overlapping HII regions, creating large HII bubbles of sizes $\sim 0.1 - 1 \text{ kpc}$, similar to what is observed in many galaxies. Of course, if the densities around stars are much higher than what is

resolved, this model could artificially over-ionize the surrounding region; however, given our ability to resolve dense clumps with $n > 10^6 \text{ cm}^{-3}$ (inside of which the Stromgren radii are negligible), we do not see much resolution dependence until we go to quite low resolutions (lower than our “standard” cases). Moreover, a non-trivial fraction of photons escape their birth environments, particularly late in the life of the most massive stars, as they disrupt their natal GMCs.

2.1.5 Long-Range Radiation Acceleration

Stellar feedback on small scales can disrupt GMCs via the mechanisms summarized above. On larger scales, galactic-scale outflows can be continuously accelerated as well. There are two basic mechanisms that can do this. First, pressure forces from hot gas can drive outflows. This should be captured explicitly in our modeling, as part of the hydrodynamics, given the heating from photoionization, stellar winds, and supernovae. In addition, gas can be accelerated outwards by the net radiation pressure produced by all of the stars in the galaxy. (Cosmic rays can also contribute to such acceleration but are not modeled here.)

In principle, the physics of radiative acceleration by the cumulative stellar radiation field is very similar to that associated with the local radiation pressure force discussed in § 2.1.1; but in practice, the model in § 2.1.1 reflects the acceleration of gas particles by radiation pressure from only the nearest star cluster. These are often dense regions in which even the infrared photons are trapped so that the *local* momentum deposition is $\sim \tau_{\text{IR}} L/c$.

Properly accounting for the full radiative acceleration by all of the stars is a formidable calculation, in particular because of the possibility of diffusion/scattering in the infrared. Here we make the approximation that the dominant acceleration on relatively large scales (ie., outside of the dense environments of star clusters and their natal GMCs) is due to the optical and UV photons, whose flux we can estimate using simple attenuation along the line of sight between the gas and star particles. Altogether, the total momentum imparted via this absorption/scattering will often be less than the momentum imparted locally from the trapped IR photons in the star-forming cloud, but the escaping UV/optical photons have the ability to accelerate gas at arbitrarily large distances from their origin. Moreover, gas above the midplane of the stellar disk “sees” the entire surface flux from the disk. Thus the light from many star clusters acts together, and can produce a large vertical acceleration, in principle launching the gas parcel out of the galaxy entirely.

For a single stellar source the flux incident on a given SPH particle is

$$\mathbf{F} = \frac{L}{4\pi r^3} \mathbf{r} \quad (2)$$

where $\mathbf{r} = \mathbf{r}_{\text{gas}} - \mathbf{r}_{\text{source}}$ and we have temporarily ignored absorption and re-radiation. This radiation flux corresponds to a momentum flux per unit area of $d\mathbf{P}/dAdt = \mathbf{F}/c$. This is incident on a mass m_i , area πh_i^2 and surface density $\Sigma_i = m_i / [\pi h_i^2]$ (here $h_i = 1.07 N_{\text{sml}}^{-2/3} h_{\text{sml}}$ is related to the SPH smoothing kernel, assuming all N_{sml} particles in the kernel are distributed uniformly over the volume and averaging over the kernel mass profile). The momentum flux imparted to the gas is just the area times the fraction of the flux absorbed or scattered per unit area, i.e. $\dot{\mathbf{P}}_i = (d\mathbf{P}/dAdt) \pi h_i^2 (1 - \exp(-\kappa \Sigma_i))$. The acceleration is then $m_i \mathbf{a} = \dot{\mathbf{P}}_i$, or

$$\mathbf{a} = \frac{L}{4\pi r^3 c} \mathbf{r} \frac{\pi h_i^2}{m_i} (1 - \exp(-\kappa \Sigma_i)) \quad (3)$$

This generalizes to a range of wavelengths using:

$$L(1 - \exp(-\kappa \Sigma_i)) \rightarrow \int L_\nu (1 - \exp(-\kappa_\nu \Sigma_i)) d\nu \quad (4)$$

If the column through any individual particle is optically thin (typical at high resolution), this simply reduces to the standard optically thin force term $d\mathbf{P}/dt = \kappa F/c$, and if the column is optically thick, it reduces to the assumption that all radiation incident on the surface $\delta A = \pi h_i^2$ is absorbed.

In general, L_ν seen by a given gas particle is not simply the un-absorbed spectrum from each star. It is, however, prohibitive to solve the full radiative transfer equations on the fly. The key approximation we make is to assume that most of the absorption and re-emission happens in the vicinity of each source. The optical depth towards a star scales as $\tau \propto \int \rho d\ell \sim \Sigma$; for realistic density profiles the optical depth is often dominated by the contribution from small radii near the star, justifying our local approximation.

In this limit, we can replace L_ν in equation 3 with an effective \tilde{L}_ν , which represents the emission of a given source after local absorption and reprocessing has been accounted for. The revised \tilde{L}_ν is modified by local radiative transfer effects on the SED and by the fact that reprocessing alters the effective size and geometry of the emitting region. To represent this geometric effect, we spread the emission out over a region of length scale ϵ_L with the softening kernel (we choose ϵ_L to be the maximum of the local gas smoothing or gravitational softening, so it represents both the local gas distribution and implicit stellar mass distribution). We have checked that this approximation, in terms of the *locations* of the flux origin, gives good agreement with the results of a full radiative transfer calculation including scattering and re-emission performed with SUNRISE (Jonsson et al. 2009).

The reprocessing and attenuation also effects the emergent SED of a given source j via:

$$\tilde{L}_\nu^j = L_\nu^j \exp(-\kappa_\nu \Sigma_{\text{column}}^j) \quad (5)$$

where L_ν^j is the intrinsic (un-obscured) spectrum from the stellar population (tabulated as a function of age from the STARBURST99 models), and Σ_{column} is the total column density (integrated to the absorbing particle) from the source. We show in § A1 that we can approximate the total column reasonably well by

$$\langle \Sigma_{\text{column}}^j \rangle \equiv \rho_j h_{\text{eff}} \approx \rho_j \left[\tilde{\alpha} h_j + \frac{\rho_j}{|\nabla \rho_j|} \right] \quad (6)$$

where ρ_j is the local gas density evaluated at the stellar source, h_j is the local smoothing length, and the characteristic scale-height of the density is given by $\rho_j/|\nabla \rho_j|$. Note that this second term makes the result for Σ_{column} independent of resolution. If the gas density around each source fell off with a smooth profile equation 6 would be exact, with $\tilde{\alpha} \sim 1$ a geometric factor that depends on the density profile shape (we adopt $\tilde{\alpha} = 0.95$ which corresponds to a linear density profile smoothed over the SPH smoothing kernel).

Because we are only interested in the integrated absorbed momentum, it is not necessary to treat L_ν as a finely-resolved spectrum. Instead, we integrate the SED over three broad frequency intervals in the UV ($\lambda < 3600 \text{ \AA}$), optical/near-IR ($3600 \text{ \AA} < \lambda < 3 \mu$), and mid/far-IR ($\lambda > 3 \mu$). The “initial” luminosity of a star particle L_ν is given by the corresponding L_{UV} , L_{Opt} , L_{IR} tabulated from the STARBURST99 models as a function of age and metallicity. The opacities κ_ν are then replaced by the corresponding flux-mean opacities κ_{UV} , κ_{Opt} , κ_{IR} , which we take to be constant = (1800, 180, 5) Z/Z_\odot , respectively.⁴ In general, the opacity will

also be a function of the thermodynamic state of the gas, e.g., because dust can be destroyed by sputtering in hot gas. These effects are not taken into account in our model.

Given the above model, it is relatively straightforward to implement the resulting radiation force on all of the gas in the simulation. Because the acceleration follows an inverse-square law with sources of luminosity L instead of mass M , the computation of the acceleration is implemented with exactly the same tree structure as the existing gravity tree. Of course the force acts only on gas particles, with the final normalization coefficient including the terms dependent on particle properties (eq. 3).

In Appendix A we present several tests and calibration studies of this model. For example, we show that the approximate treatment just described recovers the results of full (post-processing) radiative transfer calculations of the SED reasonably well. We also show that if we were to simply model the radiation field as that empirically observed in typical galaxies of each type we consider, we obtain very similar results for the momentum absorbed.

We stress that our model of the acceleration by the diffuse radiation field does not “double count” when combined with the radiation pressure included locally in § 2.1.1; the radiation pressure term there was $(1 + \tau_{\text{IR}})L/c$. The factor “1” comes from the initial extinction applied here in equations 5 and 3, $\exp(-\kappa_\nu \Sigma_{\text{column}}^j)$, i.e., the local absorption of the initial UV/optical photons. In equation (3), this factor does not add momentum to the gas, rather it attenuates the “initial” spectrum—effectively reducing the momentum carried by the UV photons emitted by young stars. It is true that we slightly over-count when we approximate the absorbed fraction of un-reprocessed radiation by unity in § 2.1.1, particularly if the actual optical depth $\kappa_\nu \Sigma_{\text{column}}^j < 1$. However, since the dust opacity to the initial radiation (which is mostly in the optical/UV) is large, this is rarely the case for the models we consider. In fact, we have implemented a more accurate model that allows for UV optically thin sight lines in the ‘local’ (to star clusters) radiation force calculation, and find that it produces no measurable differences.

2.2 Molecular Chemistry

Another potentially important element in modeling star formation is the determination of where gas can or cannot become molecular. Stars form only from molecular gas – albeit not all molecular gas, only that at the very highest densities. We have therefore also implemented several models which allow for explicit estimates of the molecular gas fraction f_{H_2} at each point in the simulation.

In § 5 we compare three different models for the molecular fraction f_{H_2} and molecular chemistry:

Molecular Model A: assume $f_{\text{H}_2} = 1$ always in regions above the SF density threshold.

Molecular Model B: the model in Krumholz & Gnedin (2011), which gives a simple fitting function for f_{H_2} as a function of the local column density ($\approx \rho h_{\text{sm}}$) and metallicity.

Molecular Model C: the model in Robertson & Kravtsov (2008), where both the molecular fraction f_{H_2} and the cooling function $\Lambda(T)$ at temperatures $\lesssim 10^4 \text{ K}$ are varied as a function of the

shape, but we choose these frequency intervals in part because the resulting κ are insensitive (changing by $< 10\%$) to the spectral shape for a wide range of stellar population ages 1 – 1000 Myr and degrees of dust reddening. The specific values used here are the average flux mean opacity of a solar-composition dust distribution in full radiative transfer calculations of the galaxy types modeled here (see Appendix A).

⁴ In detail, the effective κ for each band will depend on the exact SED

local density, metallicity, and radiation field to match the results of CLOUDY calculations.

In each case we allow only molecular gas to form stars by multiplying the calculated SFR in each particle by f_{H_2} .

We show in § 5 that the choice of models (A)-(C) has no effect on our results. This is because we only allow star formation in very dense regions (above a threshold $n > 100 - 1000 \text{ cm}^{-3}$), and the galaxies we model here are already substantially metal-enriched (even the SMC model has $Z \sim 0.1 Z_\odot$). Thus the more complex models ultimately return the result that the gas in potential star-forming regions is overwhelmingly molecular – typical optical depths to photo-dissociating radiation are $\sim 10^4$, so they are strongly self-shielding.

At sufficiently low metallicities, however, $Z \lesssim 10^{-3} - 10^{-2} Z_\odot$, molecule formation will be inefficient even at high densities and cooling times will become comparable to dynamical times. The formation of the first stars, and the lowest-mass dwarf galaxies (galaxy stellar masses $< 10^6 M_\odot$), are in this regime, where the explicit treatment of the molecular fraction above may be important (Kuhlen et al. 2011).

3 GALAXY MORPHOLOGIES

3.1 With Feedback

Figures 1-5 show the morphologies of each galaxy model, in our standard case where all feedback mechanisms are present.

We show both the gas and stars, face-on and edge-on, at times after the systems have reached a quasi-steady state equilibrium. The gas maps show the projected gas density (intensity) and temperature (color, with blue representing cold molecular gas at $T \lesssim 1000 \text{ K}$, pink representing the warm ionized gas at $\sim 10^4 - 10^5 \text{ K}$, and yellow representing the hot, X-ray emitting gas at $\gtrsim 10^6 \text{ K}$). The stellar maps show a mock three-color observed image, specifically a $u/g/r$ composite. The stellar luminosity in each band is calculated from each star particle according to the STARBURST99 model given its age, mass, and metallicity (and smoothed over the appropriate kernel). We then attenuate the stars following the method of Hopkins et al. (2005): we calculate the total dust column (from the simulated gas) along the line-of-sight to each star particle for the chosen viewing angle (assuming a constant dust-to-metals ratio, i.e. dust-to-gas equal to the MW value times Z/Z_\odot), and apply a MW-like extinction and reddening curve (as tabulated in Pei 1992).

The dramatic differences between the different galaxy models are obvious. The HiZ models result in disks with massive ($> 10^8 M_\odot$) $\sim \text{kpc}$ -scale clumps, which form massive star cluster complexes. The gas densities are sufficiently high that extinction can lead to a clumpy optical morphology as well (by entirely extinguishing out regions in the galaxy). The clumpiness is more prominent in the gas, but remains visible in the optical images. Seen edge-on, the gas can resemble a “clump-chain” morphology. Violent outflows arise from throughout the disk, driven by a massive starburst with $\text{SFR} > 100 M_\odot \text{ yr}^{-1}$.

The Sbc models also produce clumpy disk structure, but the individual clumps and star forming regions are relatively much smaller, and the global structure more clearly traces spiral arms and global gravitational instabilities. As a low-mass starburst (the galaxy has a SFR of $\sim 1 - 5 M_\odot \text{ yr}^{-1}$, despite being an order of magnitude less massive than the MW), the irregular gas morphology and thick disk more closely resemble dwarf starbursts in the local Universe such as NGC 1569 or 1313. A clumpy, multi-phase

super-wind is clearly evident, arising from the high specific star formation rate.

The MW models have a familiar spiral and barred spiral morphologies. But with our high resolution and realistic modeling of the ISM, individual star clusters and structure within the spiral arms – dust lanes, feathering, and SNe-powered bubbles are evident. Edge-on, the dust lanes and moderate/weak outflows of hot gas are also evident, but without the violence of the HiZ case.

The SMC models resemble typical irregular galaxies. The ISM is extremely patchy, with distributed molecular clouds and large, overlapping SNe bubbles. Edge-on, shells of cold material accelerated by winds out of the disk appear as blue “loops” at large scale heights, while direct venting of the hot gas is similarly apparent. The disk is “puffy” and thick, and the stars are distributed in the characteristic irregular fashion that defines the morphological class. The outer disk is clearly not star-forming; being low-density, this is maintained as an extended ionized disk by HII heating (from both the inner stellar disk and the UV background).

3.2 Effects of Each Feedback Mechanism in Turn

Having seen the typical galaxy morphologies in the case where feedback *is* present, we now consider the galaxy morphologies (and star formation histories, discussed later) with different feedback mechanisms de-activated in turn.

Figure 6 shows this for the HiZ and SMC models. We show the morphologies (at fixed time and spatial scale) and star formation histories of a few models which are otherwise identical but include or exclude different feedback mechanisms. Qualitatively, in the HiZ model, the clumpy morphology is present in all cases – since the galaxy is violently unstable, it is primarily gravity (not feedback) that dictates the gas morphology. But there are major differences between different feedback models. Most strikingly, without local momentum deposition from radiation pressure, the characteristic sizes of the individual clump cores are much smaller (this is difficult to see by eye – the central regions of each clump that appear near-white in the other images are single white pixels in this case!) This occurs because the long-range photon momentum, supernovae momentum, and stellar wind momentum are not sufficiently strong to resist the collapse of clumps beyond a critical threshold.

The effectiveness of the radiative feedback in the HiZ model results from the fact that, as shown in Paper I, the IR optical depths reach $\tau_{\text{IR}} \sim 50$. The photon momentum L/c (neglecting the boost of τ_{IR}), or the direct SNe momentum (also $\sim L/c$) are lower than that produced by the IR radiation by an order of magnitude. Hot gas (from the SNe, stellar winds, and HII regions) is clearly insufficient to prevent collapse – not surprising since the average density in the clumps is $> 100 \text{ cm}^{-3}$, so the cooling time is extremely short ($\sim 100 \text{ yr}$).

Turning off sources of hot gas, the morphologies in the HiZ galaxy is similar to the standard, all feedback case – the differences being mostly in the diffuse inter-clump gas and diffuse (volume-filling) phase of the wind. This gas is much cooler (note the absence of yellow gas), and without SNe and stellar winds the clumps and spiral arms in the gas appear much smoother (the irregular edge morphology and occasional bubbles are largely due to SNe). But the absolute wind mass is fairly similar – most of it is in the warm-phase gas clumps. Heating from HII regions is negligible – unsurprising since $\sim 10 \text{ km s}^{-1}$ is significantly less than the turbulent velocities generated by the other sources of feedback.

We do not show the Sbc and MW cases explicitly (their salient properties are shown below), but they are qualitatively similar to the

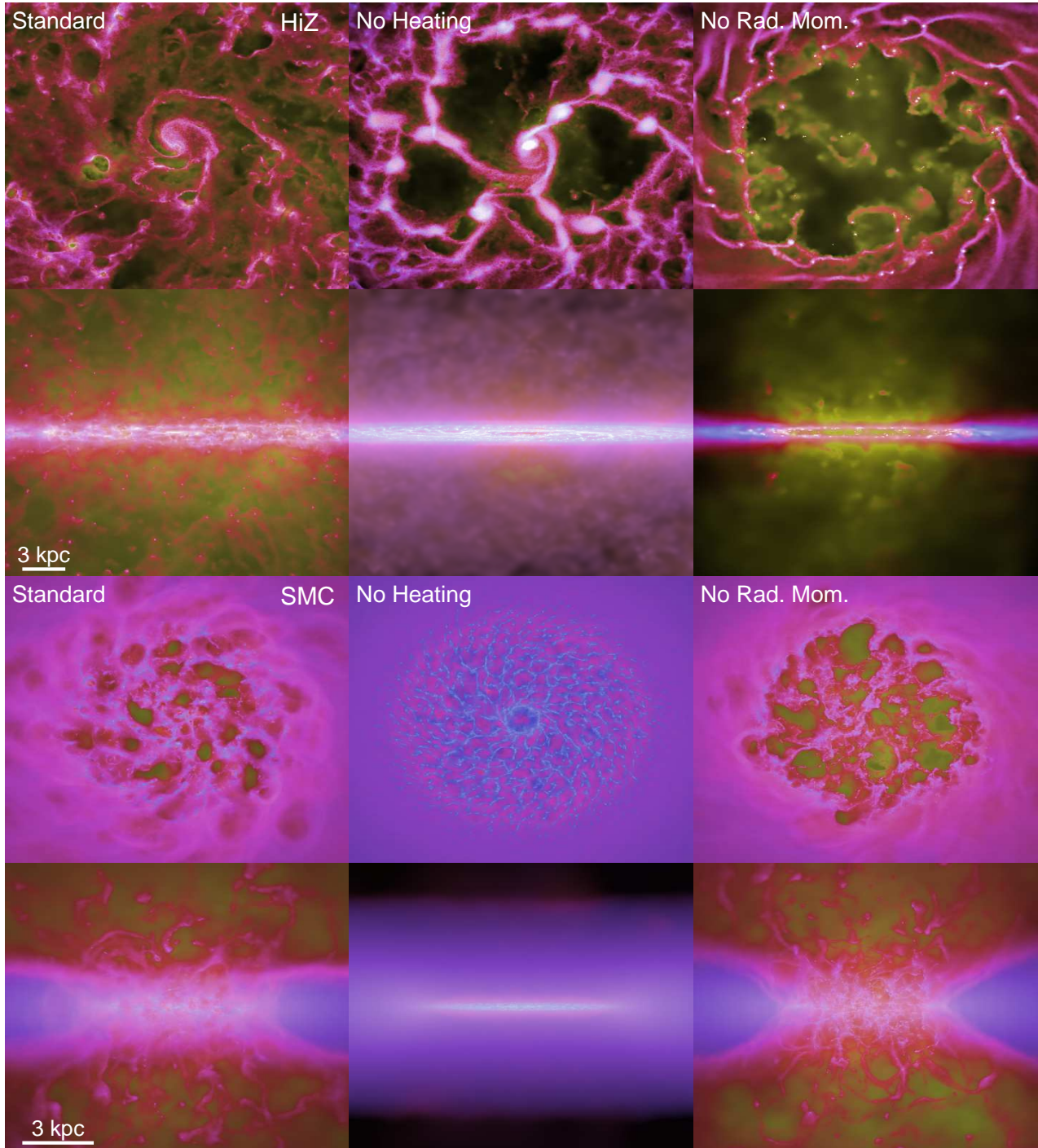


Figure 6. Face-on and edge-on gas morphologies of the HiZ (*top*) & SMC (*bottom*) galaxy models with different feedback mechanisms enabled and disabled; the stretch and color scale are the same as in Figure 1. *Left:* Standard model (all feedback on). *Middle:* No heating: energy injection from SNe, shocked stellar winds, and HII photoionization-heating is disabled (gas recycling from these mechanisms remains, but is “cold”). In the HiZ case, the “hot” volume-filling ISM is greatly diminished but the global morphology remains similar. In the SMC case, the morphology is dramatically different with the heating mechanisms turned off – there is no wind and the morphology lacks the characteristic irregular/patchy structure. *Right:* No radiation pressure (local or long-range). In the HiZ case, the hot medium is present, but individual GMC complexes ($\sim 0.1 - 1$ kpc-scale white blobs at *left*) collapse without limit (to single pixels here) and much of the cold wind mass is absent. In the SMC case, GMCs and dense ionized regions also collapse further (leading to the apparently larger filling factor of hot gas), but the wind and disk thickness are not strongly affected.

HiZ result. In the MW-analogue without radiation pressure, GMCs and star-forming “knots” again collapse to significantly smaller sizes, although the runaway is not quite as severe (early “fast” stellar winds and HII heating are able to somewhat suppress runaway collapse). Removing the sources of heating does not much change the global gas morphology, but eliminates the volume-filling “hot” gas and leaves the ISM as a whole much more cold, with a larger fraction of material in dense clouds. The Sbc case is lower-mass than the MW but more strongly self-gravitating and gas rich, so lies as expected somewhere between the MW and HiZ cases in these properties.

However, when we repeat the experiment for the SMC-like model (in the bottom half of Figure 6), the results are strikingly different. The key difference from the other three types of galaxy is that the average gas density is much lower, $n \lesssim 0.1 \text{ cm}^{-3}$, approaching the regime where the cooling time is non-negligible even near young stars. Moreover, with a lower column density and metallicity, the IR optical depths can be much lower so photon momentum is boosted little beyond $\sim L/c$. Turning off the sources of photon momentum (both local and long-range) has a relatively weak effect on the morphology (some GMCs do collapse further, but many are disrupted by SNe and stellar winds).

Turning off all of the “heating terms” from SNe, stellar winds, and HII photoionization however, has a large effect – the volume filling hot gas “bubbles” disappear and the gas clearly collapses along more global gravitational structures into a filamentary morphology reminiscent of fragmenting very large- m spiral arms, quite different from what is observed in real dwarf galaxies. Considering the three heating terms in turn, any one of them is able to prevent this complete over-cooling, leading to a morphology more reminiscent of the “standard” case. Quantitatively, however, SNe appear to be the most important heating mechanism on large scales: without SNe, there are still some hot regions created by stellar winds, but the integrated energy input in the winds is a factor ~ 8 lower. Turning off stellar wind heating has similar but less noticeable effects. HII regions and the warm gas pressure they provide are most important inside of individual GMCs; they can produce some suppression of structure but no “hot” gas, and when SNe and stellar winds are present, the addition of photoionization-heating has little effect on the global gas morphology in the star-forming disk.

4 STAR FORMATION HISTORIES

Figure 7 shows the corresponding star formation history for each model discussed in § 3.2 with different feedback effects included or excluded. For reference, we show both no-feedback models (in which case nothing stops catastrophic collapse) and the standard all-feedback models for each galaxy type.

In each galaxy type, with no feedback, the disk experiences a runaway collapse leading to the consumption of a large fraction of the gas in a single dynamical time ($\dot{M}_* \sim M_{\text{gas}}/t_{\text{dyn}}$). This gives much higher peak SFRs ($\approx 2500, 70, 40, 3 M_{\odot} \text{ yr}^{-1}$ for the HiZ, Sbc, MW, and SMC models, respectively) than observed in the real systems the simulations are designed to model, and violates the observed Kennicutt relation by factors of $\sim 10 - 100$ (see Paper I). The SFR declines only owing to gas exhaustion.

With the standard feedback model enabled, each galaxy type reaches a much lower equilibrium SFR where feedback balances gravity. These models remain in quasi steady-state for many dynamical times. In Paper I we show these SFRs agree well with the observed Kennicutt relation, as is clear from the fact that they

are in close agreement with the star formation rates observed in galaxies of each type, i.e., $\dot{M}_* \sim 100 - 300, 1 - 5, 1 - 2, 0.01 - 0.03 M_{\odot} \text{ yr}^{-1}$, respectively.

How does this self-regulation depend on the inclusion or exclusion of different feedback mechanisms? In most cases the different SFHs parallel the differences in morphology discussed in § 3.2. For the HiZ model, including or excluding heating from SNe, stellar winds, and HII regions has a negligible effect on the SFH (removing all three together is similarly negligible). Excluding either of the local momentum or long-range radiation pressure forces increases the peak SFR by a factor of $\sim 2 - 3$. Removing both leads to a runaway burst similar to the no-feedback case, with a peak SFR $\sim 1000 M_{\odot} \text{ yr}^{-1}$ and then a falloff from gas exhaustion. The system is then an order-of-magnitude above the SFR predicted by the observed Kennicutt-Schmidt relation. Clearly the critical physics are the cold radiation sources of momentum.

In the MW-like case, the SFHs are again most strongly affected by the local momentum deposition and long-range radiation pressure, but the effects of SNe heating are non-negligible. Removing both local momentum deposition and long-range radiation pressure forces leads to a near-runaway consumption of gas with a peak SFR $> 10 M_{\odot} \text{ yr}^{-1}$ in the earlier stages of the simulation evolution. This is again in excess of the observed Kennicutt-Schmidt relation.

Removing *all* nuclear powered sources of heating (SNe, shocked stellar winds, and HII photoionization) is somewhat more complex: the SFR for the first few dynamical times remains low, but then rapidly rises above the “standard” case by a factor $\sim 3 - 10$. The effect is quite non-linear, and in particular non-local. It arises from the fact that stellar mass loss is present in the model, but is now “cold” (the returned mass is injected at $\lesssim 10^4 \text{ K}$ and cools rapidly). Because the MW is quite gas-poor, this cold recycled gas can easily double the available (cold) gas mass supply at small radii (the central couple kpc) over the first $\sim 0.5 \text{ Gyr}$; what we see is actually that the gas lost by stars in the bulge (where the MW is observed and by construction initialized to have very little gas) builds up until a $\sim \text{kpc}$ -scale gas bar appears and drives a nuclear starburst at about $\sim 0.5 \text{ Gyr}$. Unlike the “no-feedback” case, the radiation pressure terms are sufficient to ensure that the model remains on the observed Kennicutt-Schmidt relation at all times: the SFR is high because that excess gas becomes compact and builds up a large mass, so the system moves along, rather than off, the relation. This explains why, in Paper I, with no recycling of stellar gas, we saw that the “radiation pressure alone” case was sufficient to maintain the MW at a steady-state SFR $\sim 1 M_{\odot} \text{ yr}^{-1}$ for several Gyr.

Among the sources of gas heating, SNe are the most important. If we just turn off shock-heating from stellar winds (“No Stellar Wind”; recall this retains stellar mass loss but it is cold), the equilibrium SFR is higher but only by a factor $\sim 1.2 - 2$. This is not surprising, since the integrated SNe energy deposition is ~ 8 times larger than that in stellar winds. Turning off HII heating also has only a small impact on the equilibrium SFR (when other mechanisms are still present). The HII heating has some effect on the evolution of individual star-forming regions (aiding in their dissociation at early times, if they are relatively low-density), but does not strongly affect the global balance of feedback versus collapse.

As in § 3.2, the Sbc-like case generally falls between the MW and HiZ cases. Heating from SNe feedback has a significant effect, but weaker than radiation pressure by a factor of ~ 3 or so.

In the SMC-like case, we see the importance of hot gas reflected in the SFHs. Removing HII heating has a negligible effect on the SFH, and removing hot stellar winds increases the peak SFR by a small factor. Removing both the local momentum

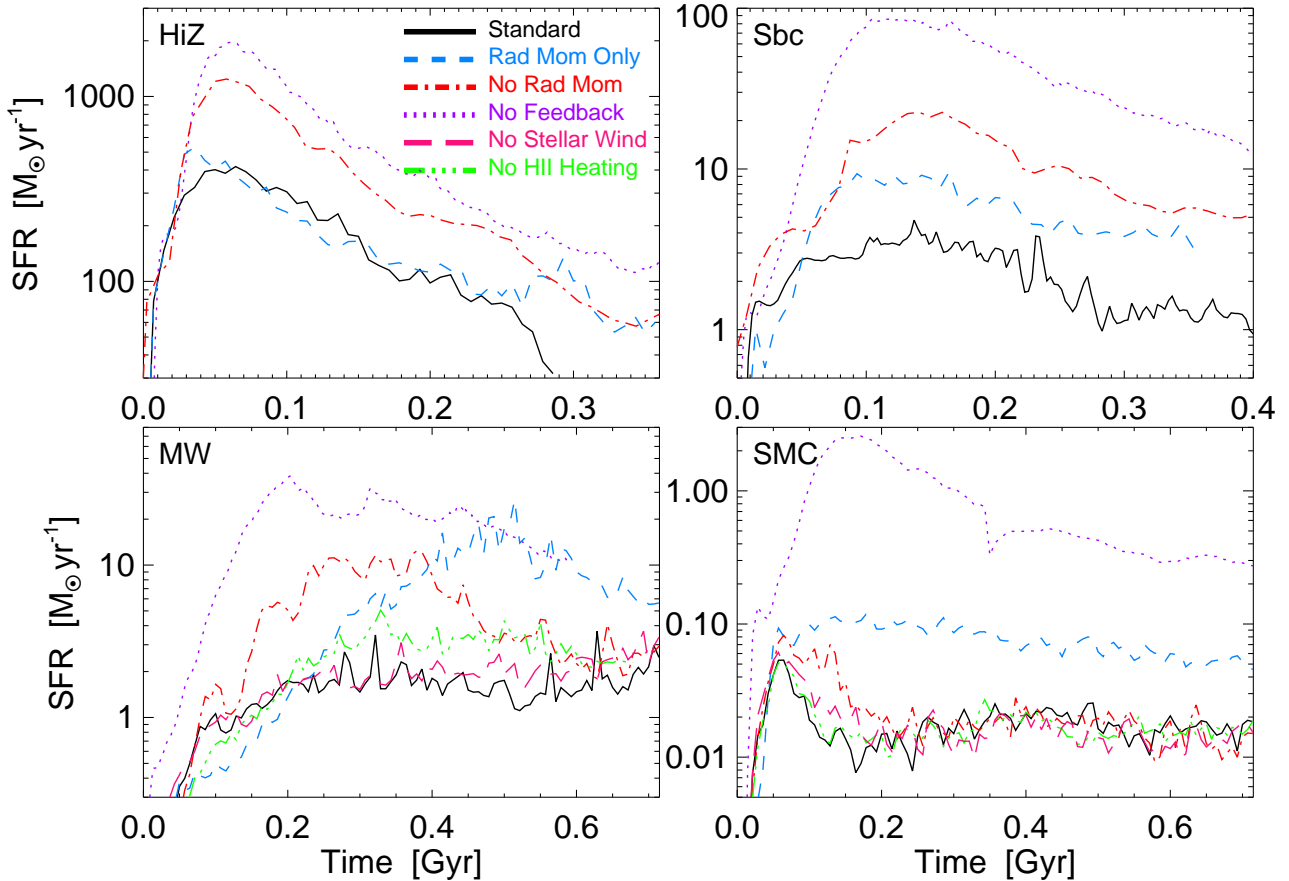


Figure 7. Star formation histories (total SFR versus time) for each of the galaxy models discussed in § 2, with no feedback (dotted line), all feedback mechanisms enabled (the “standard” model, solid line), and various mechanisms turned on and off in turn. In every galaxy type, with no feedback the disk collapses into GMCs that turn into stars in runaway fashion, leading to enormous SFRs exceeding the Kennicutt-Schmidt relation by $\sim 10 - 100$. These enormous SFRs decline over time, but only because most of the gas is consumed into stars. By contrast, with all feedback enabled, the disks reach an equilibrium SFR and maintain a quasi steady, feedback-regulated equilibrium (the star formation still declines with time in the HiZ and Sbc models because of gas exhaustion). *Top Left:* HiZ disk. Radiation pressure dominates the regulation of the SFR; turning off all heating mechanisms (dashed line) makes a small $\sim 20\%$ impact on the SFR. *Top Right:* Sbc starburst disk. Radiation pressure is still very important, but hot gas pressure makes a significant contribution to self-regulation. Removing all the explicit heating mechanisms (dashed line) leads to factor ~ 3 higher equilibrium SFR; removing radiation pressure (dot-dashed line) leads to factor ~ 10 higher SFR. *Bottom Left:* MW-like disk. The interplay between the different feedback mechanisms is more subtle in this case – see the main text (§4) for a detailed discussion. *Bottom Right:* SMC-like isolated dwarf. Here, SNe heating is the most important mechanism regulating the galaxy-scale star formation.

and long-range radiation pressure forces only increases the median SFR by a significant but not dramatic factor ~ 2 at early times. In contrast, removing SNe increases the typical SFR by a factor of $\sim 5 - 8$. It is worth noting that even after this increase, the SFR is still much less than it would be with no feedback ($\sim 0.1 M_{\odot} \text{ yr}^{-1}$ versus $\sim 3 M_{\odot} \text{ yr}^{-1}$), so there are important contributions to self-regulation from *all* sources of feedback, but SNe are the most important among them.

5 THE (NEGLIGIBLE) ROLE OF MOLECULAR CHEMISTRY

It is well-established that stars form only from molecular gas – albeit not *all* molecular gas, but only a small fraction at the highest densities. Hence a number of groups have attempted to model galactic star formation using various schemes to estimate the molecular fraction in a large volume of gas in a simulation (see Robertson & Kravtsov 2008; Ostriker et al. 2010; Kuhlen et al.

2011). Given our inclusion of a wide range of feedback physics, does chemistry matter?

We test this by re-running our standard models with all feedback present, but with different explicit models for the molecular fraction in gas. First (Molecular Model A), we make the crude assumption that the molecular fraction is always unity in all regions above our density threshold for star formation.

Second (Molecular Model B), we adopt the prescription in Krumholz & Gnedin (2011, eqn. 1-4 therein), which approximates the results of full radiative transfer calculations with a simple analytic fitting function that gives f_{H_2} (the fraction of gas mass in a given particle which is molecular) as a function of the local column density and metallicity. We approximate the local column as the integral across the SPH smoothing kernel ($\propto \rho h$, analogous to what is done with the AMR experiments therein).⁵ We then allow only

⁵ This is a conservative assumption because, if the integral column over large spatial scales is much larger, then it will further self-shield the gas, which only strengthens our conclusions below.

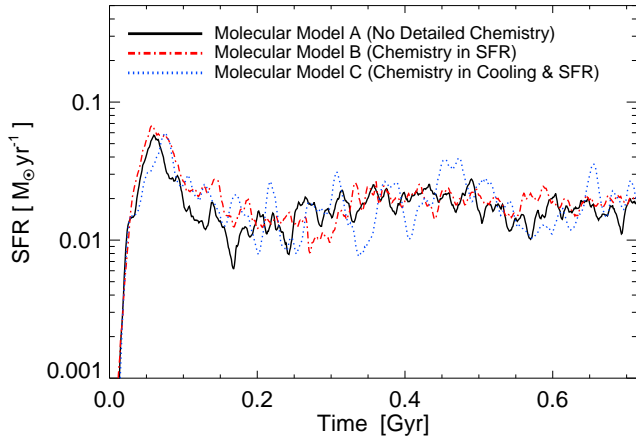


Figure 8. Star formation history for SMC models with different treatments of the molecular chemistry of the gas; all of the simulations have all of our feedback mechanisms enabled. The SMC model is the most sensitive of our galaxy models to the molecular chemistry because of its lower surface density and metallicity. (A): We use our standard cooling curve (see §2) and assume that all gas above the star-forming threshold ($n \gg 100 \text{ cm}^{-3}$) is molecular (the H_2 molecular fraction $f_{\text{H}_2} = 1$) and so can turn into stars at an assumed efficiency per dynamical time of 1.5%. (B): We use the fitting functions in Krumholz & Gnedin (2011) for f_{H_2} as a function of local column density and metallicity for each gas particle and only allow star formation in molecular gas. (C): We use the model in Robertson & Kravtsov (2008), in which the molecular fraction f_{H_2} and the cooling function $\Lambda(T)$ at low temperatures $\lesssim 10^4 \text{ K}$ are a function of the local gas density, metallicity, and radiation field (based on CLOUDY calculations); star formation again only occurs in molecular gas. Overall, the treatment of the molecular chemistry has a negligible effect on the star formation history. This is because star formation only occurs in high density gas, $n \gtrsim 100 - 1000 \text{ cm}^{-3}$, and at the SMC’s metallicity of $Z \sim 0.1 Z_{\odot}$, the molecular fractions in the dense, star-forming gas are always near unity (average $f_{\text{H}_2} > 0.998$ for models (B) and (C)). In test calculations, only at extremely low metallicity, $Z \ll 10^{-2} Z_{\odot}$, does the molecular chemistry begin to have a measurable effect on the star formation history.

the molecular gas to form stars – multiplying the SFR our standard code would estimate by f_{H_2} .

Third (Molecular Model C), we adopt a more detailed treatment motivated by that in Robertson & Kravtsov (2008). We allow the cooling function Λ to be a function not just of temperature but also the local gas density, metallicity, and radiation field, where the latter is approximated by the sum of the cosmic background ($z = 0$ value) and the local SFR (taking the instantaneous SFR in the local gas and assuming the continuous SF limit) with the SEDs tabulated in STARBURST99. Specifically the cooling functions are tabulated from Figure 1 of Robertson & Kravtsov (2008) (on a simple grid in density, metallicity, and radiation field) and we interpolate logarithmically. We then calculate the local molecular fraction in each particle as a function of column density, metallicity, and also ionizing field strength from the fitting function in Krumholz & Gnedin (2011). As before, we then only allow SF from the “molecular” gas.

Figure 8 shows that modeling the molecular gas fractions has no effect on our results. If we plot the morphology of each system (or any other measurable quantity presented in this paper), we find the same.

Why do we find that detailed chemistry is essentially irrelevant, while other authors have found it is critical? The key is the scales that we resolve and on which we allow star formation to proceed. In previous models where the molecular fraction is estimated and makes a large difference, it is usually the molecular fraction in

a large volume of the ISM that is being estimated – radii at least $> 100 \text{ pc}$ and as large as several kpc, with bulk volume densities of $\sim 0.1 - 10 \text{ cm}^{-3}$. Essentially, then, the “molecular” model is really an implicit model for the fraction of dense gas within the patch. In contrast, our simulations explicitly resolve dense regions, and only allow star formation in them; our typical threshold for star formation is a local density of $n > 100 - 1000 \text{ cm}^{-3}$. At these densities, the gas is overwhelmingly molecular, so explicitly accounting for a molecular fraction and allowing only that gas to form stars is essentially identical to our existing prescription. In fact, we know the typical optical depths through the star-forming patches of gas (from our local momentum-driving model) and in the optical and UV wavelengths, they are typically $\sim 10^4$, so there is no question that the gas can self-shield. In fact, when we implement the model of Krumholz & Gnedin (2011), we find the average estimated molecular fraction in the gas we would allow to form stars is $> 99.8\%$.

Furthermore, in Paper I, we show explicitly that the *global* star formation history is independent of the small-scale star formation law, because the star formation rate is set by the requirement that feedback from young stars maintain marginal stability. This requirement of vertical pressure support implies that allowing only molecular gas to form stars on a constant timescale within these high density regions will give the same star formation rate.

We also have tested, in Appendix A of Paper I, that changing the cooling curve shape dramatically – for example, changing its normalization by a factor of several, or changing its shape to a simple constant from $10 - 10^4 \text{ K}$ – has no impact on our results, because in each case the cooling time in the gravitationally collapsing dense regions is still shorter than the dynamical time by a factor $\approx 10^4 - 10^5$ at densities near the threshold for star formation (at least down to $\approx 100 \text{ K}$, at which point the thermal pressures are totally negligible compared to gravity, and so subsequent cooling has only weak effects).

Glover & Clark (2012) study star formation on small scales with a variety of different chemical and cooling models, and reach the same conclusion we do here. They show that the molecular fraction under otherwise identical densities and metallicities is causally irrelevant to the collapse of dense gas, since cooling via C^+ fine-structure and dust emission is nearly as efficient as CO – the presence of CO is very tightly correlated with, but does not *drive* the collapse of gas to high densities.

Thus it is only if cooling and the formation of metals, dust, and molecules are dramatically suppressed that the explicit chemistry will become important for any of the quantities we model. This occurs at metallicities below $Z \sim 10^{-3} - 10^{-2} Z_{\odot}$. Specifically, this is the metallicity at which the molecular fraction begins to fall below unity in gas near our threshold density; this is also the metallicity at which the cooling time can become comparable to, or longer than, the dynamical time (see e.g. Robertson & Kravtsov 2008). The formation of the first stars, and the lowest-mass dwarf galaxies (galaxy stellar masses $< 10^6 M_{\odot}$) are within this regime and will be strongly influenced by the ability of the gas to form molecules even at high densities. But the more massive systems we model here (even the SMC) are safely in the regime in which the dense gas is almost all molecular and thus so long as star formation is restricted to the dense gas, an explicit treatment of the molecular chemistry is not important.

6 GLOBAL PROPERTIES: DISK VELOCITY DISPERSION AND SUPPORT

We now examine the structural properties of our model disks, as a function of time and radius, with different feedback mechanisms enabled and disabled.

Figure 9 plots a number of disk structural properties as a function of time. We are particularly interested in the properties of the star-forming disk, as opposed to e.g. the extended ionized HI disk (which is obviously not strongly affected by feedback), so we calculate all values as gas-mass weighted averages in each radial annulus at each time, then plot the SFR-weighted average over radial annuli (the results reflect the value near $\sim R_e$, but do not vary rapidly in radius). First, the resolved vertical velocity dispersion σ_z (specifically, half the 15–86% interval in v_z , to minimize the bias from large “tails” of outflowing material at high- v_z). Second, the ratio σ_R/σ_z , between the in-disk plane radial velocity dispersion and vertical dispersion (the azimuthal dispersion $\sigma_\phi \approx \sigma_R$ in all cases). Third, the (fractional) disk scale height h/R , where the scale-length h of the disk fit to a vertical sech^2 profile. Fourth, the Toomre Q parameter,

$$Q \equiv \frac{\delta_{VR} \kappa}{\pi G \Sigma} \quad (7)$$

where δ_{VR} is the effective radial dispersion of the gas, $\equiv \sqrt{\sigma_R^2 + c_s^2} \approx \sigma_R$ (because the thermal sound speed $c_s \ll \sigma_R$ in the dense gas, in all cases), κ is the epicyclic frequency ($\approx \sqrt{2}\Omega$ for nearly constant- V_c disks here), and Σ is the gas+stellar disk surface density. Finally, the disk gas fraction, defined locally as $f_{\text{gas}} \equiv \Sigma_{\text{gas}}/(\Sigma_{\text{gas}} + \Sigma_*)$.

The very early time behavior is a result of the initial conditions: these include large vertical support for the disks, which quickly vanishes as the disks cool, then dense GMCs form and begin to produce stars. After about an orbital time, the systems reach a quasi-equilibrium state, which can clearly be seen (at least in cases with feedback) in the flat or slow subsequent time dependence. Once in this regime, details of the initial conditions (e.g. whether the initial disks are supported by turbulent or thermal velocities) have no significant effects.

6.1 Dispersions and Gas Fractions

6.1.1 Comparison to Observations

For the cases with all feedback mechanisms enabled (our “standard” model), the values generally agree with observed disks at similar mass and redshift to the analogs in each model. The HiZ disks have SFRs of $\sim 70 - 300 M_\odot \text{ yr}^{-1}$, a morphology of massive clumps, purely vertical velocity dispersions of $\sim 30 - 40 \text{ km s}^{-1}$ and sightline-averaged dispersions of $\sim 50 - 100 \text{ km s}^{-1}$, giving typical $V/\sigma \sim 5$ or so given their maximum circular velocity $V_{\text{max}} \approx 230 \text{ km s}^{-1}$, and high gas fractions $\sim 30 - 60\%$ for most of their lifetimes,⁶ all in good agreement with observed properties of the most massive star-forming disks (Genzel et al. 2008; Förster Schreiber et al. 2006; Erb et al. 2006; Tacconi et al. 2010).

The Sbc disks also maintain high gas fractions, low $V/\sigma \sim 5 - 8$, with large dispersions and puffy scale heights. In both of these cases, the specific star formation rate is high, and the disks are

clumpy and self-gravitating; feedback and gravity therefore maintain large dispersions in the gas.

The MW-like runs maintain the canonical observed $\sim 8 - 15 \text{ km s}^{-1}$ dispersion, which with $V_{\text{max}} \approx 220 \text{ km s}^{-1}$ gives $V/\sigma \sim 20 - 30$, and gas fractions $\approx 10\%$ – because they are much more stable (with large dark matter halos), and have low gas fractions (and low specific star formation rate), these disks are thinner, relative to the starburst systems.

The SMC-like runs show a similar moderate dispersion $\sim 6 - 8 \text{ km s}^{-1}$, giving $V/\sigma \sim 5 - 15$, and maintain very high gas fractions $\sim 70 - 80\%$; these properties all agree very well with typical properties for $\sim 10^9 M_\odot$ dwarf galaxies (see e.g. Bell & de Jong 2001; McGaugh 2005). Here, the self-gravity, star formation rate, and corresponding dispersion are low, but the potential is very shallow, so even small dispersions maintain relatively “puffy” gas disks, as observed. Gas fractions are generally larger at large radii as the disks have some bulge and a more extended gas versus stellar disk; there are some small flares at large radii but these are weak. There is a rise in V/σ at large radii as the gas at these radii is very low-density and has a low specific star formation rate, hence low feedback support and low σ . In these outer regions the disk is supported in part supported by thermal pressure, maintained by external radiation, either from the interior of the disk or from the cosmic background ultraviolet radiation.

We have also measured the full turbulent velocity power spectrum in these simulations, and find its shape – essentially consistent with equal power on all scales (with a break below the disk scale-height where the system transitions from being effectively two-dimensional to three-dimensional) – varies little across simulations (with normalization just set by σ and the scale-lengths here). This is expected: since the bulk gas motions are super-sonic and gravity is the dominant force, the turbulence should be largely scale-free. This is true even if motions are “pumped” by stellar feedback, because the fraction of the time that *direct* feedback forces are dominant over gravity and bulk hydrodynamic forces as the force on a given gas parcel is small. For this reason, we do not see strong imprints of the input feedback injection or velocity scale – quite unlike a case where gas is “held up” in some hydrostatic sense by feedback forces.

6.1.2 Failings of Feedback-Free Models

There are important differences if we compare runs with feedback to the no-feedback cases. Most obviously, without feedback the gas fractions plummet extremely quickly, as essentially the entire galaxy gas supply collapses into dense regions and is turned into stars in a single global dynamical time.

The *vertical* dispersions (and as a consequence, scale heights) are also significantly lower (at least for most of each run) in the cases without feedback. This is despite the fact that the rapid gas depletion should make it much easier for non-feedback (and non-nuclear powered) mechanisms to maintain large dispersions in the remaining gas. In the HiZ and Sbc cases, the systems are strongly gravitationally unstable, with large clumps scattering off each other and massive inflows along bars and spiral arms. However, almost all of this gravitational potential energy goes into maintaining the in-plane dispersions. The in-plane dispersions can be maintained at large values by global gravitational instabilities (sinking clumps, bars, and spiral arms) that avoid rapid shocks and dissipation precisely because they are global structures. In contrast, the vertical motions drive shock heating on the local dynamical time, so σ_z rapidly drops to a low value.

⁶ Recall this is essentially f_{gas} at the effective radius of star formation, which evolves weakly in time as gas can be depleted at small radii (giving the slow decline in SFR seen in Figure 7).

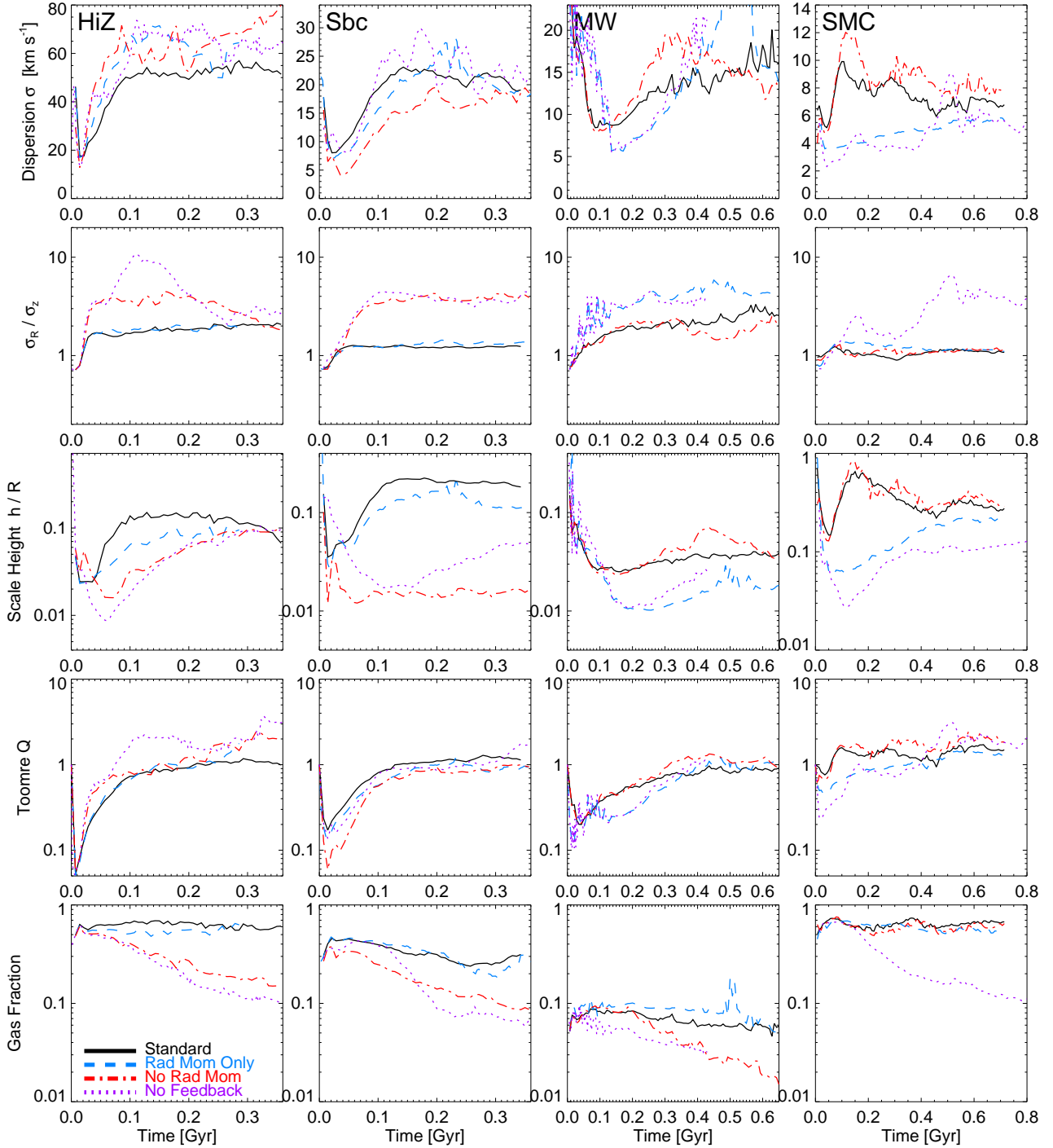


Figure 9. Global galaxy structural properties in *gas* (not stars) as a function of time, in otherwise identical simulations of each galaxy model with various feedback effects enabled (different lines – see Table 2). Each quantity is the weighted average over the star-forming disk. *Top:* Sightline-averaged one-dimensional gas velocity dispersion σ . *Second from Top:* Velocity (an)isotropy: ratio of in-plane radial dispersion σ_R to vertical dispersion σ_z . *Middle:* Vertical scale height-to-radius ratio h/R . *Second from Bottom:* Toomre Q in the gas ($\sigma_R \kappa / \pi G \Sigma$). *Bottom:* Gas fraction $M_{\text{gas}} / (M_{\text{gas}} + M_*)$. With all feedback enabled, values agree well with those observed: f_{gas} evolves slowly, feedback preserves stability ($Q \approx 1$, with σ driven to the appropriate observed value for each galaxy) and isotropizes the dispersions ($\sigma_R \approx \sigma_z$, giving $h/R \approx \sigma_z / V_c$). With no feedback, runaway star formation consumes the gas. Dispersion and Q still increase, but only because all high-density (rapidly cooling, $Q < 1$) gas is totally exhausted. In the HiZ and Sbc cases, removing radiation pressure yields results similar to the “no feedback” case (SNe, stellar winds, and photoionization-heating cannot prevent runaway dissipation in dense gas). In the SMC case, gas heating by SNe is more important than radiation pressure for the disk structure. In the MW case, all mechanisms contribute comparably.

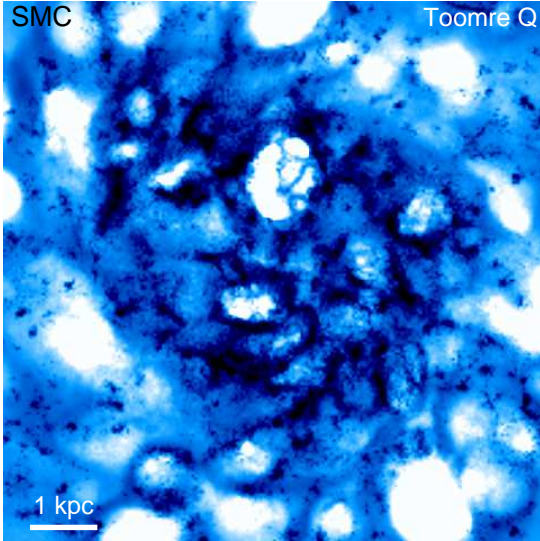


Figure 10. Face-on map of the Toomre Q parameter (eqn. 7) for the gas within the disk averaged over ~ 10 pc annuli. Intensity is scaled logarithmically with Q from $Q \leq 0.1$ (black) to $Q \geq 10$ (white). We show the SMC model as Fig. 5. Despite the robust global convergence to $Q \sim 1$ in Fig. 9, there are large local variations in Q , as some regions have dissipated their support and are collapsing (on their way to forming stars) while others have just experienced strong local bursts of stellar feedback and are rapidly expanded and/or heated.

At late times in both the HiZ and Sbc cases σ_z begins to rise, but the models have a gas fraction of just a few percent at the time, and that gas is mostly being “dragged” by a few super-massive stellar clumps, and undergoing mergers at the galaxy center.

The SMC case is physically quite different from the HiZ and Sbc models: the system requires only small dispersions, but it is so gravitationally *stable* (owing to the large dark matter to disk ratio) that it does not develop large turbulent motions in the absence of feedback. Again, though, it shows a large σ_R/σ_z without feedback, from the moderate spiral structure in place. The MW model, interestingly, is in some ways a “worst-case” system for discriminating the effects of feedback (the differences are minimized) – this is because it has a low gas fraction, requires a low gas dispersion for vertical pressure equilibrium, and is marginally unstable to e.g. spiral arm formation.

6.1.3 Effects of Each Feedback Mechanism In Turn

Now consider cases with different feedback mechanisms included or excluded. For the HiZ and Sbc-like cases, removing the sources of “hot” gas (e.g. SNe feedback, stellar wind shock-heating, and HII heating) has relatively little effect on any of the quantities plotted in Figure 9. Removing the radiation pressure (momentum feedback acting on cold, dense gas) however, leads to much more rapid star formation and hence a runaway decrease in f_{gas} . The full dispersion, $\sigma_R^2 + \sigma_\phi^2 + \sigma_z^2$, is essentially the same for any combination, or lack, of feedback. As we argued in the previous paragraph, global gravitational instabilities (powered by accretion through the disk) can maintain σ_ϕ and σ_R . But clearly the no-feedback and radiative momentum models are “failed” in the sense that they did not prevent runaway star formation and, at a fixed gas fraction f_g , the vertical velocity dispersion σ_z is too small.

For the SMC case, “hot” feedback is much more important, since the average densities are much lower and opacities and specific star formation rates (important for radiation pressure) much lower as well. Removing all the hot gas sources, but keeping radiation pressure in place, moderate but slightly lower vertical dispersions $\sim 5 - 6 \text{ km s}^{-1}$ can be maintained, and star formation efficiencies are still much lower than the no-feedback case (by a factor ~ 10 , see Paper I and §4) but they are higher than the case with hot gas sources by a factor of several. Supernovae are most important source of hot gas in the SMC model (as we saw for the SFR above and winds in Hopkins et al. 2011b). Removing stellar winds or HII heating has very little effect on the dispersions or other properties if SNe feedback is still included; however, if SNe are absent, they are able to maintain comparable dispersions.

Finally the properties of the MW-like model lie in between the HiZ and Sbc models on the one hand, and the SMC model on the other, as expected. As noted above, in the MW model all the feedback mechanisms seem to contribute comparably, making it difficult to distinguish the effects of different feedback mechanisms.

6.2 Toomre Q and Disk Stability

All of the systems modeled here equilibrate at a Toomre $Q \sim 1$, and maintain this over the disk surface. In the feedback-regulated cases, this must happen: $Q < 1$ regions will collapse and begin forming stars, which leads to a super-linear feedback (in that the further collapse proceeds, the more rapid the SF and hence momentum/energy injection becomes), until it arrests further collapse (which by definition is when it re-equilibrates to $Q \sim 1$). If $Q > 1$, then there is no collapse, hence no dense regions form and no star formation takes place; without feedback to hold up the disk, the cooling time is much less than the dynamical time, and so it radiates away its support in at most a crossing time (the dissipation time for turbulent support).

Fig. 10 illustrates how this global equilibrium is maintained, by showing a map of the local values of Q (calculated within 10 pc annuli) for the SMC model (the other models are qualitatively similar). Although the disk maintains an average $Q \sim 1$ there are large local variations from $Q \sim 0.1 - 10$, corresponding at low- Q to the regions which have begun to collapse, and at high- Q to regions which have recently formed massive stars and are being disrupted and heated by feedback. The characteristic spatial and time scales, therefore, for these fluctuations, are closely associated with the Jeans scale and associated crossing times.

However, even the feedback-free systems also equilibrate at $Q \sim 1$. The reason is simple: nothing can prevent runaway collapse and star formation in $Q < 1$ regions, so all the gas that can reach $Q < 1$ does so, and then turns into stars, leaving only $Q \gtrsim 1$ gas remaining. Thus $Q \sim 1$ can be maintained, but at the expense of runaway gas consumption. Quantitatively, we make a crude analytic estimate of the dispersions that can be maintained by inflow and instabilities. The vertical velocity dispersion dissipates on a vertical crossing time, $H/\sigma_z = r/V_c$, where the second expression follows from the assumption that the turbulence provides the vertical support against gravity required to maintain the vertical scale height H . The luminosity dissipated by turbulence is then $L_{\text{urb}} = \eta \sigma_z^2 \Omega M_g$, where M_g is the gas mass of the disk and η is a constant of order unity. In the absence of feedback, this luminosity must be supplied by global gravitational instabilities (sinking clumps, bars, spiral arms), ultimately powered by accretion of gas through the disk. (We assume that the accretion energy is converted into isotropic

turbulence). The accretion luminosity is $L_{acc} = 2\dot{M}_{acc}V_c^2$.⁷ We can find a lower limit to \dot{M}_{acc} assuming the disk is in a quasi-steady state, so that the mass accretion rate must exceed the star formation rate, given by the Kennicutt-Schmidt relation, $\dot{\Sigma}_* = \epsilon\Sigma_{gas}\Omega$, with $\epsilon = 0.017$. Averaging over the disk, $\dot{M}_* = \epsilon\nu^{-1}\dot{M}_g\Omega$ where Ω is evaluated at the disk effective radius, and $\nu \approx 2$ depends on the surface density profile. Combining these relations, we find

$$\frac{\sigma_z}{V_c} = \left(\frac{3\epsilon}{2\eta\nu}\right)^{1/2}. \quad (8)$$

Using this estimate for σ_z in the expression for the Toomre parameter,

$$Q_{grav} \approx \left(\frac{\sigma_R}{V_c}\right) \frac{2\tilde{\kappa}}{\nu f_{gas}} \approx f_{gas}^{-1} \left(\frac{2\kappa}{\nu\Omega}\right) \left(\frac{3\epsilon}{2\nu\eta}\right)^{1/2} \approx \frac{0.1}{f_{gas}} \quad (9)$$

so we expect $Q \sim 1$ as f_{gas} depletes below $\lesssim 0.1$, which is roughly what the simulations show.

Even in simulations with no star formation, and hence no gas consumption (“No Feedback or SF” in Table 2), the systems quickly reach $Q \sim 1$. In these models, the gas collapses and cools until it is essentially all in extremely dense clumps, $n > 10^6 \text{ cm}^{-3}$ in Fig. 3 of Paper I – corresponding to $\sim \text{kpc}$ -scale patches collapsing to $\sim \text{pc}$. This makes the gas effectively collisionless! The gas “nuggets” (which internally continue to dissipate, but are long-lived and rarely collide) scatter and develop $Q \sim 1$ just as the stars do.

7 ISM PHASE STRUCTURE

7.1 Mass and Volume of Phases with Feedback

Figure 11 shows the density distribution in three of our “standard” simulations with all feedback implemented normally. For each, we present the distribution in three ways. First, we consider the total mass-weighted density distribution ($dm_{gas}/d\log n$), for *all* gas in the simulation. This covers a very wide dynamic range in both density and spatial scale, and is not directly comparable to the typical “ISM density distribution” from galaxy studies. To see this, we divide the gas into three categories: the star-forming disk (defined as gas within the projected radius that encloses 90% of the total star formation and within one vertical scale height of the disk inside that radius), the extended disk+halo gas (gas outside the disk, but not in the wind defined below), and the wind/outflow material (gas above a scale height, with large radial outflow velocity $v_r/|v| \geq 0.75$ and $v_r > 100 \text{ km s}^{-1}$). The star-forming disk (radii $\sim 8, 4, 10, 3 \text{ kpc}$ in the HiZ, Sbc, MW, and SMC case) extends out to a couple optical scale-lengths, and (unsurprisingly) includes almost all of the dense gas ($n \gtrsim 1 \text{ cm}^{-3}$). The extended disk and halo cover intermediate densities: this includes the initial extended gas disks, which extend to very low densities and tend to be ionized hydrogen disks with $T_{eff} \sim 10^5 \text{ K}$, and material which is pushed out of the disk by feedback but does not contain enough energy/momentum to drive an outflow (the “halo” – recall there is no initial extended gaseous halo in these simulations). This contains a large fraction of the gas mass in all cases, most of which is out at several optical disk scale lengths. The wind material extends to the lowest densities – since there is no IGM, in principle escaped material can reach arbitrarily

low densities – and although it contains some cold, dense clumps (visible in the density distribution or in Figures 1-5), it contains most of the hot gas with $T_{eff} \gtrsim 10^6 \text{ K}$. Much of this material is out at very large radii of order the virial radius.

We next consider the phase structure of the star-forming disk in detail, since this is the traditional region in which the ISM phases are defined and where stellar feedback has the greatest impact. Specifically, we show the mass-weighted density distribution ($dm/d\log n$) and volume-weighted density distribution ($dV/d\log n$; where the volume of each particle is proportional to its smoothing length cubed), within the star-forming disk identified above (since there is no outer boundary to the simulation, the “total” volume-weighted density distribution diverges at low densities with the material at the furthest edges of the simulation). We divide the gas into three traditional phases with a simple temperature cut: “cold atomic+molecular” gas ($T < 2000 \text{ K}$), “warm ionized” gas ($2000 < T < 4 \times 10^5 \text{ K}$) and “hot” gas ($T > 4 \times 10^5 \text{ K}$). The exact temperature cuts are arbitrary but the qualitative comparison does not change if we shift them by moderate amounts. Unsurprisingly, the high-density gas ($> 1 \text{ cm}^{-3}$) is predominantly cold, the intermediate-density gas ($0.01 - 1 \text{ cm}^{-3}$) primarily warm, and the low-density gas ($< 0.01 \text{ cm}^{-3}$) hot. The temperature structure also explains the features seen in the total density distribution, arising from the separate components – the total distribution is crudely log-normal, but each component individually is more clearly so.

By mass, the cold/molecular phase dominates, but with a comparable contribution from the warm/ionized phase, and the ratio of the warm-to-cold gas increases as we move to lower-mass, low-average density systems ($M_{warm}/M_{cold} \sim 0.3, 0.5, 0.7$ in the HiZ, MW, and SMC-like cases, respectively). The “hot” phase constitutes at most a few percent of the total mass budget within the star-forming disk ($\approx 1 - 3\%$ in each case). By volume, however, the results are reversed. The “hot” phase has a near-unity volume filling factor in each case. The “warm” phase has a non-trivial filling factor ($\sim 0.3, 0.5, 0.7$ in the HiZ, MW, and SMC-like cases), but it can be significantly less than unity. Recall from Figures 1-5 that the “warm” phase is still often concentrated in dense structures such as the spiral arms (or in the HiZ case, in giant cloud complexes) as well as loops and shells blown by hot bubbles (although again, most of the warm gas is in the extended ionized disk). The cold phase has a very small filling factor of a few percent ($\sim 3 - 10\%$).

The warm and hot phases of the ISM have similar thermal pressure $P \approx 5 \times 10^{-13} \text{ erg cm}^{-3}$, which for the warm material reflects gas with $n \sim 0.1 - 0.4$ and $T \sim 1 - 5 \times 10^4$ and for the hot gas $n \sim 0.003$ with $T \sim 10^6 \text{ K}$. Both include a tail of material with pressures up to ~ 100 times larger, much of which is recently-heated material that is venting out of the disk, but some of which is recently photo-ionized dense gas that is “breaking out” of GMCs. As expected, the thermal pressure of the cold gas is lower than the ambient medium by a factor of $\sim 10 - 30$. However, the turbulent pressure of the clouds is much larger, $P \sim 10^{-10} - 10^{-9} \text{ erg cm}^{-3}$ – this is consistent with their being marginally bound (discussed below), for which $P \sim G\Sigma_{cloud}^2 \sim 10^{-9} \text{ erg cm}^{-3} (\Sigma_{cloud}/100 M_\odot \text{ pc}^{-2})^2$. The warm/hot pressure increases as well if we include the turbulent ram pressure, but by order-unity factors; they satisfy $Q \sim 1$ hence $P \sim G\langle\Sigma\rangle^2$, so the pressure ratio is approximately the squared ratio of GMC to disk-average surface densities. The cold clouds are therefore clearly not typically pressure-confined, but held together by self-gravity.

⁷ The factor of four ($2 = 4 \times 1/2$) comes from the energy transported by the torques causing the accretion; this factor is larger (by 4/3) in a constant- V_c disk than that in a Keplerian disk.

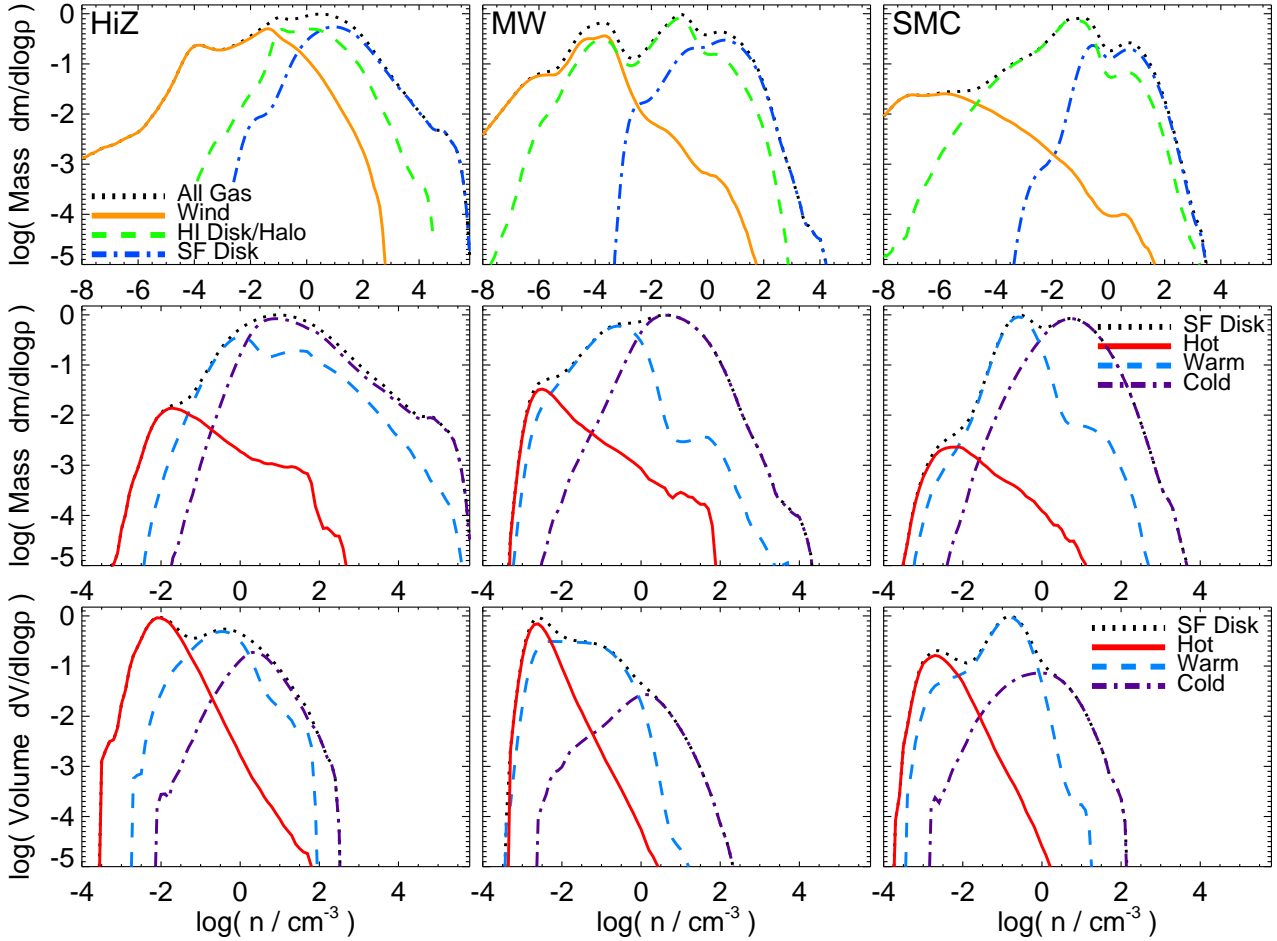


Figure 11. Density distribution of different ISM phases, for different galaxy disk models (HiZ, MW, and SMC), at times after they reach feedback-regulated steady-state. Variation in time after the first orbital time is modest. *Top:* Mass-weighted density PDF ($dm_{\text{gas}}/d\log n$), i.e. the mass fraction per logarithmic interval in density n . We show the distribution for all gas in the simulation (black), the gas within the (multi-phase) star-forming disk (blue), the gas in the extended, ionized non-star forming HI disk and halo (green), and wind/outflow material (orange). These trace the material at low, intermediate, and high densities, respectively (as expected). Each density PDF has a very broad density distribution. *Middle:* Mass-weighted density PDF within the star-forming disk – i.e. the traditional multi-phase ISM. We show the density PDF for all of the gas in the disk (black), the “cold/molecular” phase (purple; $T < 2000$ K), the “warm ionized” phase (cyan; $2000 < T < 4 \times 10^5$ K), and the “hot diffuse” phase (red; $T > 4 \times 10^5$ K). Most of the mass is in the cold phase (which dominates at high densities), but with a non-negligible ($\sim 20 - 30\%$) contribution from the warm medium (the hot phase contributing $\sim 5 - 10\%$). There is also a weak trend towards the cold phase being more important in more massive, gas-rich disks (HiZ versus SMC). Note that the multi-modal nature of the total density PDF is a consequence of the strong phase separation. *Bottom:* Volume-weighted density PDF ($dV_{\text{gas}}/d\log n$) for the star forming disk. The hot diffuse phase dominates, with a moderate ($\sim 20 - 40\%$) volume filling fraction for the warm phase, and a small ($\sim 1 - 5\%$) volume filling fraction of cold clouds.

7.2 Dependence on Feedback Mechanisms

It is useful to identify observational tests which discriminate between different feedback mechanisms, and in this section we explore some candidates. In Figure 12, we consider how the distribution of cold and hot gas depends on the various feedback mechanisms implemented. With no feedback, there is runaway collapse in the cold gas with a large secondary peak at $n \rightarrow 10^6 \text{ cm}^{-3}$ (the highest densities we can resolve). Turning off *all* heating mechanisms (SNe, stellar winds, and HII photoionization-heating) together leads to a modest increase in the amount of high-density $n \gtrsim 10^4 \text{ cm}^{-3}$ material in the MW and SMC models (these mechanisms are also responsible for heating the small tail of “cold” material at $n \sim 0.01 - 1 \text{ cm}^{-3}$ which appears when feedback is turned off). But in all models, turning off radiation pressure yields a much more dramatic increase in the amount of very dense material. In other words, even where global self-regulation can be set by SNe

heating, the dense material at $n \gtrsim 10^4 \text{ cm}^{-3}$ is regulated by radiation pressure. This should not be surprising – even in a low-density galaxy like the SMC, the optical depths at these densities are large in the infrared; and the cooling times for a SNe remnant in such high-density material are $\sim 10^4$ times shorter than the dynamical time, so pure gas heating is ineffective.

With no feedback, there is essentially no hot gas, in any model – pure gravitational turbulence and shocks alone can maintain some gas at $\sim 10^4$ K or so, but not $> 10^6$ K. Without gas “heating” from SNe and shocked stellar winds the mass of hot gas drops by a large factor of $\sim 10 - 100$, even in the HiZ and Sbc cases. The turbulent motions in the disk driven by radiation pressure have velocities comparable to the escape velocity from massive star clusters – tens of km s^{-1} , so shocks between them produce little “hot” material. HII photoionization-heating obviously does not produce temperatures in this range. As we have shown above, most of the hot gas comes from SNe (the integrated hot gas energy in stellar winds

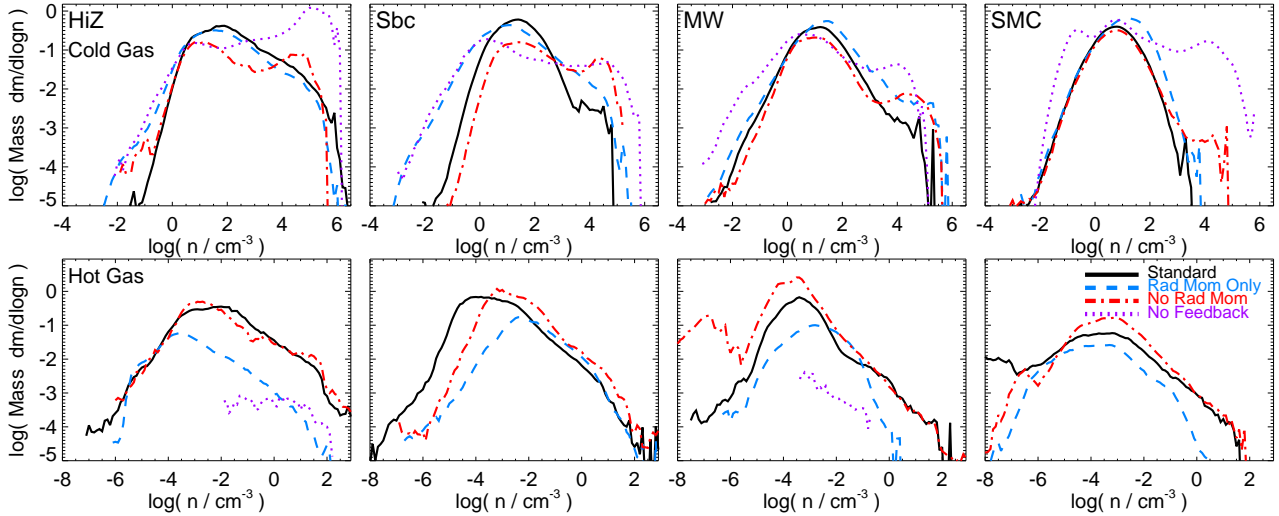


Figure 12. *Top:* Mass-weighted density distribution of “cold” gas ($T \lesssim 1000$ K) for models with different feedback enabled (as in Fig. 7 and Table 2). *Bottom:* Mass-weighted density distribution for the “hot” gas ($T \gtrsim 10^6$ K). Without feedback, gas piles up at $\gtrsim 10^5 \text{ cm}^{-3}$, and there is essentially no hot gas. Removing radiation pressure leads to a similar pile-up at very high densities, even in the MW & SMC cases (in which SNe heating alone can regulate *global* properties). Removing gas heating (by SNe and stellar winds) leads to more low-density cold gas and dramatically suppresses the hot gas mass.

being smaller by a factor ~ 8 , even though their instantaneous luminosity in the OB phase can be higher).

The large variation in the amount and average density of the dense gas in Figure 12, and the deviations from log-normality, are striking, given that we showed in Figure 9 that the different feedback models all produce nearly identical velocity dispersions and self-regulation at $Q \approx 1$. They *all* maintain large-scale turbulence, in other words, even though some experience runaway collapse (which is then reflected in the much larger SFRs for these models). But it is commonly assumed in various star-formation models that maintaining large-scale turbulence alone is sufficient to prevent runaway collapse (e.g. Ballesteros-Paredes et al. 2007; Tasker & Tan 2009; Krumholz & McKee 2005). Moreover many high-resolution studies of idealized, turbulent boxes have found that “pumping” the global modes in the box with momentum equivalent to $Q \sim 1$ establishes a lognormal density PDF (with a dispersion that scales very weakly with mach number $\propto \sqrt{\ln(1 + 3\mathcal{M}^2/4)}$; e.g. Vázquez-Semadeni 1994; Padoan et al. 1997; Scalo et al. 1998; Ostriker et al. 1999; Federrath et al. 2008; Price et al. 2011) and prevents runaway collapse/star formation (Vázquez-Semadeni et al. 2003; Li et al. 2004; Li & Nakamura 2006).

However, there are two major differences between our simulations and many idealized turbulence models. First, the typical idealized box simulation realizes only a sub-region of one cloud: with a mass of a few tens typically measured in units of the thermal Jeans mass ($\sim c_s^3 G^{-3/2} \rho^{-1/2}$); as such the statistics only extend to the $\sim 10\%$ level (i.e. to $\sim 1\sigma$ in the distribution), and “lognormality” is seen only on a linear scale. Indeed, even in these simulations, hints have often appeared of non-lognormal “tails” in the distribution (see Ballesteros-Paredes et al. 2011). But with such sampling, it is not possible for a large sub-region (itself containing many Jeans masses) to detach from the global flow, dissipate, and collapse. In contrast our simulations here sample $> 10^7$ thermal Jeans masses, and so can easily probe such fluctuations.

Second, we include cooling and self-gravity, which are not always followed self-consistently in idealized simulations. This is critical for “runaway.” Turbulence does tend to drive the distribution to a lognormal. But the tails converge very slowly (with the

Poisson error) – according to the central limit theorem, convergence to lognormality in a given portion of the distribution requires a number of “events” such that $N^{-1/2} \ll 1$, i.e. for each Jeans mass region (here more properly defined in terms of the turbulent Jeans mass), $N_{\text{crossing times}}^{-1/2} \ll 1$. But if cooling is fast relative to the dynamical time, a self-gravitating region collapses on a single crossing time. Outside of $\sim 1 - 2$ standard deviations from the core of the lognormal, then, a region cannot be “held up” or dissociated by cascades of turbulence from large scales “mixing” it back to low densities before it collapses. Regions will instead be continuously “pumped” to randomly cross this threshold, at which point they detach and collapse, building up the excess at large densities. It is therefore critical to invoke a feedback mechanism that can act *directly* on the gas at very high densities to dissociate these collapsing regions before they completely run away, and re-mix them into the larger-scale medium.

And this is exactly what we see: the fact that all the simulations maintain similar velocity dispersions is the reason that the median/peak density (around $\sim 10 - 100 \text{ cm}^{-3}$) in the dense gas is similar in all cases, and within $\sim 1\sigma$ of this peak, they almost all appear reasonably well-behaved lognormal distributions. But the radiation pressure and other feedback acting in the dense gas is critical to suppress the runaway “tails” seen in the no-feedback runs, and in the “No Radiative Momentum” runs in the three more massive galaxy models. It is these tails which in turn contribute the gas that is actually forming stars (densities $> 10^4 \text{ cm}^{-3}$), and hence lead to runaway star formation.

8 THE PROPERTIES OF GMCs

Having considered the global properties of the ISM above, we now turn to the sub-structure predicted: specifically, the properties of giant molecular clouds. Figure 13 shows an illustrative example of a region near the center of the SMC simulation, with GMC structure resolved down to $\sim \text{pc}$ scales. It is clear that the GMCs formed exhibit considerable structure, with filamentary large-scale molecular gas and dense knots and clumps (the star-forming regions) embed-

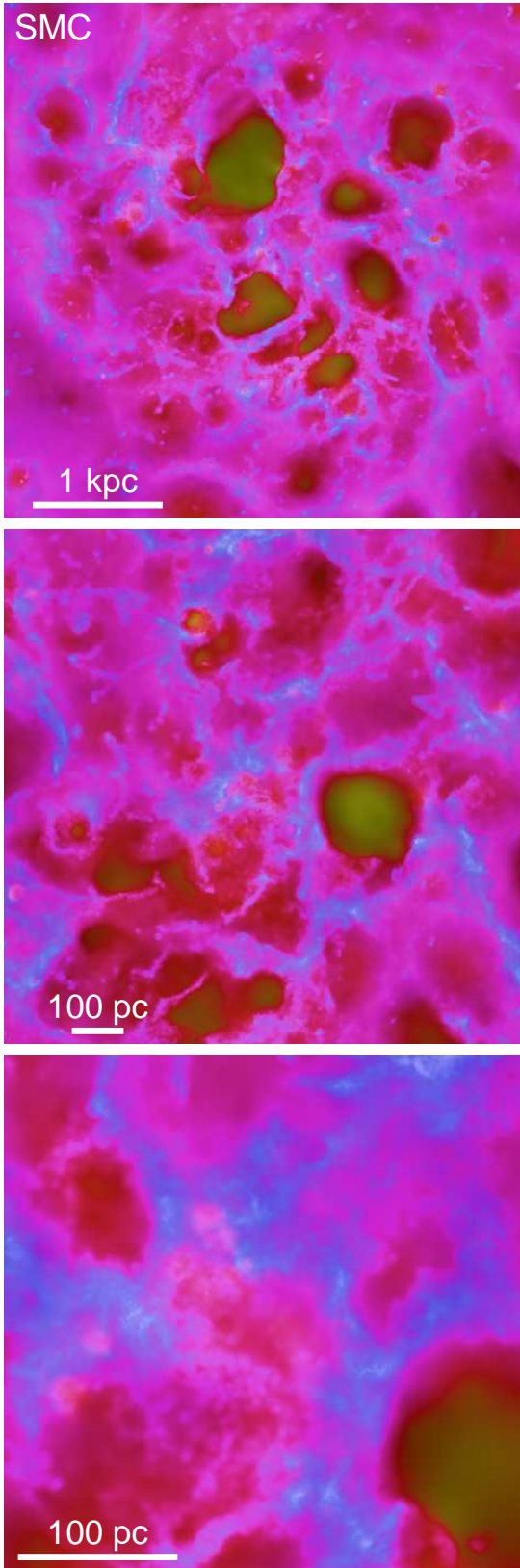


Figure 13. Zoom-in of regions with a large concentration of GMCs in the SMC simulation. As in Figure 1, brightness encodes projected gas density (logarithmically scaled with a ≈ 4 dex stretch) and color encodes gas temperature, with blue being $T \lesssim 1000$ K molecular gas, pink $\sim 10^4 - 10^5$ K warm ionized gas, and yellow $\gtrsim 10^6$ K hot gas. The filamentary nature of clouds, with dense cores (bright white-blue regions) and diffuse molecular material (diffuse blue regions), and < 10 pc-scale structure are evident.

ded throughout. The irregular, clumpy, and triaxial morphology of these clouds is very similar to typical observed GMCs. They are *not* “small disks,” which is the typical case when “GMCs” are formed in simulations with weak feedback (a point we will discuss in more detail below).

To identify individual clouds (especially given their complex morphology), we follow a procedure motivated by observational studies, but taking advantage of the full simulation data. Specifically, we consider each simulation output snapshot and apply the sub-halo finder SUBFIND, which employs a friends-of-friends linking algorithm with an iterative unbinding procedure to robustly identify overdensities (for details and tests, see Springel et al. 2001). The routine is modified to run on the disk gas (instead of dark matter) and with softenings and linking lengths appropriately rescaled for the mean gas densities within the disk effective radius. Visual inspection confirms that this correctly identifies the obvious clumps, and binding criteria (discussed below) also support the identifications. Changing the linking lengths and other numerical quantities has a weak effect on most properties, but we explicitly note where the GMC properties are sensitive to the algorithm. This tends to occur in the most massive clumps in each simulation, as these are often located at global critical points (e.g. along spiral arms or bars) and have their own sub-structure, so deciding whether or not to break them into sub-units is sometimes ambiguous. This same uncertainty, however, applies to observational studies as well – we discuss its possible effects where they may be important below, but these few cases do not affect our qualitative conclusions.

8.1 GMC Mass Functions

Figure 14 shows the resulting GMC mass function, for our different galaxy models with feedback enabled. The results converge to a quasi-steady state, despite the fact that (we will show) individual clumps are short-lived, so the mass function reflects continuous dissociation and re-formation. The shape in all cases is an approximate power law with a steep (exponential or log-linear) cutoff at some high mass, so one could fit the usual truncated power-law or Schechter functions:

$$N(> M) = N_0 \left(\frac{M}{M_0} \right)^{-\alpha+1} \exp(-M/M_0) \quad (10)$$

we choose this form so that α corresponds to the logarithmic slope of dN/dM , standard in observational studies. Observed values tend to lie within the range $-2.1 \lesssim \alpha \lesssim -1.5$ shown in the Figure 14, with the “canonical” value of -1.8 very close to the typical slope we find (fitting the function above to all simulation timesteps, we find an average $\alpha \approx -1.75 \pm 0.2$).

We show this explicitly by comparing the observed GMC mass functions for the MW (from Williams & McKee 1997, corrected to represent the total MW population, since we consider all GMCs in the simulation), appropriate to compare to our MW-like simulations, and for the LMC (from Rosolowsky 2005), appropriate to compare to the SMC-like simulation. Of course the normalization N_0 of the observed and simulated populations is arbitrary and depends on the total gas mass, but for these comparisons the total gas mass is similar. We expect the Sbc case to be qualitatively similar to these but with different normalization and zero point. For the high-redshift case, the total gas mass and most massive clump mass are much larger than local systems, so there is no direct comparison available, but observations have indicated that typical systems similar to our HiZ model have approximately $\sim 5 - 10$ clumps

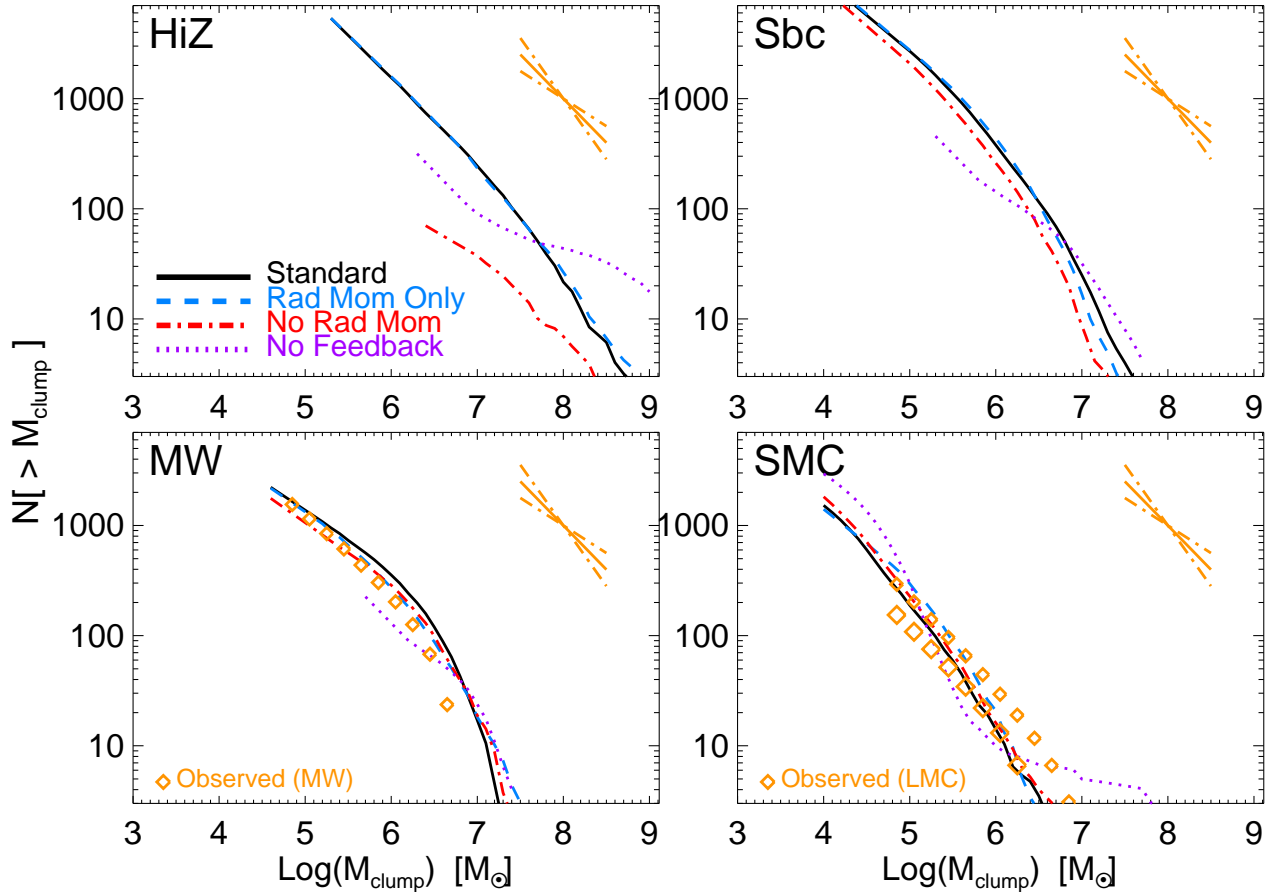


Figure 14. Predicted mass function of GMCs in the simulations (see §8 for a discussion of how we identify GMCs). We show the different galaxy models, each with runs that include different feedback mechanisms (see Table 2). The distributions can all be fit by a power-law with a cut-off at high mass (eqn. 10). For the MW model and dwarf/SMC model, we compare with the observed MW and LMC mass functions, respectively (Williams & McKee 1997; Rosolowsky 2005, orange diamonds). Characteristic slopes in *observed* systems are also shown for comparison (orange lines for $\alpha = -1.5, -1.8, -2.1$, where $N(> M) \propto M^{-\alpha+1}$). In all models, the predicted slope is similar to that observed: it follows generically from gravitational collapse (with super-sonic flows). The cutoff mass traces the Jeans mass in each model (eqn. 11); since all reach $Q \sim 1$, the high mass cutoff is weakly sensitive to feedback, primarily through more/less efficient gas exhaustion ($f_{\text{gas}}(R)$). With weak/absent feedback, the very high-mass tail is enhanced even though typical clouds are less massive; this is because massive clouds along global ISM structures (e.g., spiral waves) do not disrupt but accrete continuously.

in the $\gg 10^8 M_\odot$ range, similar to the number predicted (Förster Schreiber et al. 2011).

The mass function slope appears fairly generic. To see this, we compare models with different feedback mechanisms enabled and disabled, as in § 6. The characteristic or maximum masses may shift by small amounts without certain feedback included, but the slope α is similar in all cases. We have also checked this within each feedback model, for example, arbitrarily multiplying or dividing the strength of the momentum coupling from radiation pressure by a factor of 5. A mass function slope close to $\alpha \sim -2$ tends to emerge generically in any system dominated by gravitational collapse (e.g. Press & Schechter 1974; Bond et al. 1991); the location of the high-mass cutoff and exact deviation from -2 depend on details of e.g. the power spectrum, non-gravitational terms, and Jeans conditions (if the medium is gaseous), but the low-mass slope must be close to -2 because gravity is scale-free.⁸ This explains

⁸ Implicit here is the assumption that motions are super-sonic, so the thermal properties do not set a preferred length scale, but this is easily satisfied in the simulations and observations, down to scales well below what we resolve ($\lesssim 0.03$ pc).

why simulations with very different physics included recover similar behavior (compare our runs and e.g. Audit & Hennebelle 2010; Tasker 2011).

The cutoff mass M_0 appears to be simply related to the turbulent Jeans mass in each disk:

$$M_J = \frac{\sigma^4}{\pi G^2 \Sigma} = 4\pi \Sigma h^2 \approx \left(\frac{\nu Q}{2}\right)^2 f_{\text{gas}}^2 M_{\text{gas}}(< R) \quad (11)$$

where the latter expression includes the Toomre $Q \sim 1$ and the parameter $\nu = 1 - 2$ which depends on the mass profile, and f_{gas} refers to the fraction of gas mass relative to the *total* enclosed mass. Evaluated at R_e for the typical conditions of each galaxy model seen in Figure 9, this gives $M_J \sim (1 - 5 \times 10^6, 0.5 - 2 \times 10^7, 1 - 4 \times 10^7, 0.3 - 1 \times 10^9) M_\odot$ for the SMC, MW, Sbc, and HiZ cases. Of course, the exact values will change with time and the precise location in the disk, and mergers and agglomerations can grow clumps beyond this limit. But it appears to be a quite good approximation to the ‘‘cutoff’’ in the integrated mass functions.

When we compare models with different feedback mechanisms enabled or disabled, the slope is similar, but there are some

small shifts in the “cutoff” mass. At low/intermediate masses, models with less efficient feedback are shifted to slightly lower GMC masses. This is most noticeable when we remove radiation pressure in the HiZ or Sbc cases, remove hot gas in the SMC case, or remove all feedback in any case – just what we expect, since we already saw these have the largest effects in Figure 9. Recall, we showed above that all the models tend to $Q \sim 1$, so this primarily reflects somewhat more efficient gas exhaustion lowering M_{gas} and so the Jeans mass.

However at the very highest masses the behavior is perhaps unexpected; despite these shifts the extreme high-mass “tail” of the mass function extends to higher maximum masses. Two effects drive this. First, the most massive clumps tend to be massive clump-complexes along e.g. spiral arms, which are linked by intermediate-density material. Without being able to fully dissociate this material, the friends-of-friends GMC finder tends to link these into single “super-clumps.” This alone is ambiguous – it is well known in observations that at high masses the assignment of “clump mass” is quite sensitive to the exact clump identification and linking criterion (see Pineda et al. 2009). We err on the side of over-linking rather than missing real clumps, but if this alone drove the effect seen we would not assign it much meaning. However there is also a robust physical effect: clumps survive longer with weak feedback. The same most massive clumps, located along global structures, can then accrete large quantities of gas, growing beyond the Jeans mass. This leads to the odd shapes of the high-mass mass function in these cases, where the high-mass end does not rapidly fall off, but “turns up” in a manner not observed to date.

8.2 Density Distributions

8.2.1 Three-Dimensional Densities

The distribution of three-dimensional densities n in clouds is more or less the distribution of “cold gas” shown in Figure 12. As discussed above, the distributions in our standard models are crudely log-normal with median $\sim 10 - 100 \text{ cm}^{-3}$ and scatter $0.25 - 0.30 \text{ dex}$, within which most of the GMC mass resides. This value increases systematically with the average density of the galaxy; fitting a mode to each lognormal gives $\approx 25 \text{ cm}^{-3}$ in the SMC model and 100 cm^{-3} in the HiZ model. This must happen: the HiZ model has an initial smooth disk-averaged $n \sim 40 \text{ cm}^{-3}$ inside R_e , so any clumps must have larger n . There are tails at the $< 10\%$ level in the distributions which include the high- n cores. This reproduces a key feature of observed GMCs: although most of the mass within e.g. the star-forming galactic disk is in “dense” gas, in the form of GMCs, most of the gas *within* those GMCs is at relatively low densities, *not* within star-forming cores that have densities $\gtrsim 10^4 \text{ cm}^{-3}$ (e.g. Williams & McKee 1997; Evans 1999, and references therein).

As noted above, these distributions remain steady-state throughout the simulations. After the initial couple dynamical times, the median densities vary (randomly) within factors $\lesssim 1.5$ and dispersions vary within 0.1 dex . This is non-trivial – as time passes, there is not a one-way collapse to high densities but self-regulation at a constant density distribution.

However, models without feedback do not have a stable density distribution, and “pile up” at the highest resolvable densities $n \gg 10^4 \text{ cm}^{-3}$ as seen in Figure 12. We saw there that this is primarily a function of the radiation pressure support. In the MW and SMC models, gas heating by stellar winds and HII photo-ionization is able to stave off complete runaway cloud collapse but without ra-

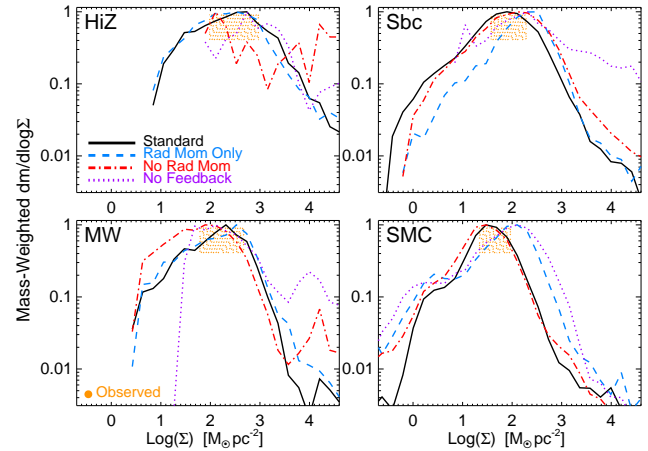


Figure 15. Distribution of average GMC surface densities $\langle \Sigma \rangle$, calculated as the mass-weighted $\langle \Sigma \rangle$ averaged over viewing angles for each cloud. We show each disk model with different feedback mechanisms enabled (see Table 2). The distributions are close to log-normal in the core, with the median surface density $\sim 50 - 300 M_{\odot} \text{ pc}^{-2}$ increasingly modestly as the average gas surface density of the star-forming disk increases. The scatter in the surface density of GMCs is small ($\approx 0.2 \text{ dex}$). For comparison, we show the observed median $\langle \Sigma \rangle$ and $\pm 1 \sigma$ range (shaded orange) inferred for SMC and MW clouds and the range for all dwarf galaxies observed for the Sbc-like run (Bolatto et al. 2008); for the HiZ run we take the estimate for $z \sim 2$ galaxies in Forster Schreiber et al. (2009). With no feedback, *local* collapse proceeds without limit (to high n), which gives rise to the high- Σ tail in the GMC surface densities seen here, but does not necessarily change the median $\langle \Sigma \rangle$. With feedback, clouds are more triaxial and short-lived and so do not globally contract by a large amount.

diation pressure the number of ultra-dense cores is enhanced. We emphasize though, that the effect of feedback is primarily on the high-density tails in Figure 12; since most of the gas is at low (non star-forming densities), its distribution is similar even in the presence of runaway local collapse and star formation.

8.2.2 GMC Surface Densities & Size-Mass Relation

A closely related metric is the average cloud surface density $\langle \Sigma \rangle$, shown in Figure 15. Here we use the mass-weighted average surface density over sightlines through the cloud $\langle \Sigma \rangle$; this is not exactly the same as the area-average $\sim M/\pi R^2$ but is well-defined even for arbitrary cloud geometry. In each model, the $\langle \Sigma \rangle$ distribution follows a relatively narrow log-normal. The median GMC surface density increases from $\approx 50 M_{\odot} \text{ pc}^{-2}$ for the SMC, to $\approx 500 M_{\odot} \text{ pc}^{-2}$ in the HiZ model, as they must given the increasing background density. The scatter is again roughly constant, only $\approx 0.2 \text{ dex}$, and the distributions in this projection are closer to exact log-normal than n . This narrow distribution in Σ means the clouds follow a size-mass relation approximately $R \propto M^{0.5}$, with a normalization consistent with the observed range (weakly increasing with galaxy surface density) and small scatter.

These surface densities (and corresponding size-mass relation) and their scatter are quite similar to those observed in MW-like and SMC-like local galaxies (Bolatto et al. 2008; Fukui et al. 2008; Wong et al. 2008; Goodman et al. 2009). Observations have even found evidence for a systematic shift in the normalization of the size-mass relation ($\langle \Sigma \rangle$) towards lower densities in SMC clouds and higher densities in dense regions of massive galaxies (Bolatto et al. 2008; Heyer et al. 2009). In fact, the properties of the most

massive clouds in our HiZ simulation agree well with those inferred for the most massive star-forming molecular “clumps” in $z \sim 2 - 3$ galaxies observed with integral field data and in some cases individually lensed (Forster Schreiber et al. 2009; Swinbank et al. 2011), which are offset towards higher $\langle \Sigma \rangle$ relative to the extrapolation of the local relation.

Our predictions are also, interestingly, similar to the predictions in higher-resolution simulations of individual GMCs with quite different physics included (e.g. ignoring radiation pressure but including magnetic fields; see Ostriker et al. 2001; Tasker 2011). This suggests that they are fairly generic. No-feedback cases do feature a larger tail towards high- Σ , but the median values are actually quite similar to the cases with feedback. This fits with the behavior we saw in § 6.1, where dissipation is efficient in the vertical direction of the disk without feedback, but there is still large radial and azimuthal motion. In detail, what we see with no feedback is often clouds collapsing, dissipating all of their energy in a crossing time, but then being arrested by residual angular momentum. They become small, rapidly rotating disks, with clumpy sub-regions collapsing further. This has been seen in other high-resolutions disk simulations without feedback, as well (Bournaud et al. 2007; Dobbs 2008; Tasker & Tan 2009). In other words, without feedback, GMCs do not collapse three-dimensionally, and so they can locally collapse to arbitrarily high densities, turning all their mass into stars in a couple crossing times, even though their surface densities are not very different from cases with efficient feedback. This behavior, and strong rotational support for highly “flattened” molecular clouds are, however, not observed (Rosolowsky et al. 2003; Imara et al. 2011). Much closer to observed systems are the models with strong feedback, which have similar local σ_z and σ_R , leading to molecular clouds which, while certainly non-spherical, are not highly flattened (they tend towards irregular, triaxial and filamentary shapes, with some preference for elongation in the galactic plane as observed; see Koda et al. 2006) and not rotationally supported (see Figure 13).

With feedback included, clouds are three-dimensional; feedback has greatly slowed collapse. Moreover, we will show that with feedback, clouds are dissociated in just a few dynamical times. As a result, the clouds can undergo little global contraction (even though over-dense regions within the clouds can collapse to very high densities and form stars). The surface densities $\langle \Sigma \rangle$ are therefore just a reflection of the average surface densities of the disk from which they form. Specifically, the peak in typical cloud surface density in Figure 15 in each model is just $\approx 2 - 5$ times the average disk surface density within the star-forming disk. In other words, the remarkable independence of the global cloud densities on the details of feedback, and apparent narrow range in densities, is just a consequence of the fact that they are dissociated after just a few dynamical times, before they can globally contract (and are slowed in that contraction even during that time). This is quite similar to what is observed: although the star-forming *cores* within GMCs reach large columns $N_H \gtrsim 10^{24} \text{ cm}^{-2}$ (optically thick in the IR), MW GMC complexes are observed to have a surface-averaged column density of just $10^{21} - 10^{22} \text{ cm}^{-2}$, similar to the average through the disk.

8.3 Linewidth-Size Relation

Closely related to the typical densities and surface densities of clouds are the Larson’s law-type scaling relations. We have already discussed the size-mass relation; in Figure 16, we plot the linewidth-size relation. For simplicity, we define the radii and ve-

locity as the rms spherical radii and velocity dispersion; because observations generally de-project to three-dimensional quantities assuming an ellipsoid in projection, this is probably a reasonable approximation at the level we consider here. We are not making a detailed mock observation of molecular gas in various states, so there will be some systematic uncertainties in the comparison, but the senses of the scalings are robust to various density limits and definitions. For clarity, we plot just a small randomly sampled subset of the clouds.

The predicted linewidth-size relation is broadly similar to that observed with an approximate $\sigma \propto R^{0.5}$ scaling, in the range where there is overlap ($\sim 5 - 300 \text{ pc}$), and continues the observed scalings beyond that to larger $\sim \text{kpc}$ clump sizes in the massive systems (we plot two characteristic points from the observations of Forster Schreiber et al. 2009; Förster Schreiber et al. 2011, for $z \sim 2$ clumpy disks). As expected from the behavior of $\langle \Sigma \rangle$, there is a normalization shift such that the HiZ systems obey a similar power-law but with higher σ at fixed R (reflecting their higher densities). The predicted values, which exhibit this shift, appear consistent with the observed massive high-redshift systems. For clarity, we have shown just our “standard” model, because the power-law scaling is similar for most of our models, with normalization offsets that follow simply from the differences in average density (above) and virial parameters (discussed below).

Again, models with a wide range of different physics included appear to capture the linewidth-size relations. As with the size-mass relation, the key point is that with feedback present, clouds are short-lived and collapse weakly. Moreover because the scaling above is based on second moments in velocity and size, it is especially sensitive to the less tightly-bound/collapsing material. As such, the observed scaling reflects the conditions of marginal self-gravity and Jeans collapse. The scale-length of Jeans collapse is just $\lambda \sim \delta v^2 / \pi G \Sigma$. So if the systems have not been able to evolve very far from their initial collapse, i.e. if they are short lived, then we simply expect $\delta v \propto \sqrt{\lambda}$ across regions with similar Σ , with a residual normalization dependence

$$\frac{\delta v}{R^{0.5}} \propto \Sigma^{0.5} \quad (12)$$

similar to what is observed and simulated.

8.4 GMC Virial Parameters

Figure 17 shows the distribution of virial parameters α of the simulated clouds, defined as the ratio of kinetic to potential energy. Observationally, this must be estimated from global cloud properties, so is commonly defined as

$$\alpha \equiv \left| \frac{2T}{V} \right| \approx \frac{a_1 M_{\text{cl}} \sigma^2 / 2}{a_2 G M_{\text{cl}}^2 / R_{\text{cl}}} \approx \frac{5 \sigma^2 R_{\text{cl}}}{G M_{\text{cl}}} = \frac{M_{\text{vir}}}{M_{\text{cl}}} \quad (13)$$

where the factor of 5 follows from common assumptions for the terms a_1 and a_2 (order-unity constants that depend on the true mass profile shape and projection), σ and R_{cl} are the average dispersion and radius,⁹ and $M_{\text{vir}} \equiv 5 \sigma^2 R / G$. With this definition (if the assumed coefficients are correct), $\alpha = 1$ would be virial equilibrium.

The “average” clumps are consistent with being marginally gravitationally bound, $\alpha \sim 1$. There is a broad dispersion of $\gtrsim 0.5$ dex about this median, reflecting both different states of various

⁹ For consistency with the observations we compare to, we take σ and R_{cl} as randomly-sampled line-of-sight and corresponding projected dispersion and half-mass-radii.

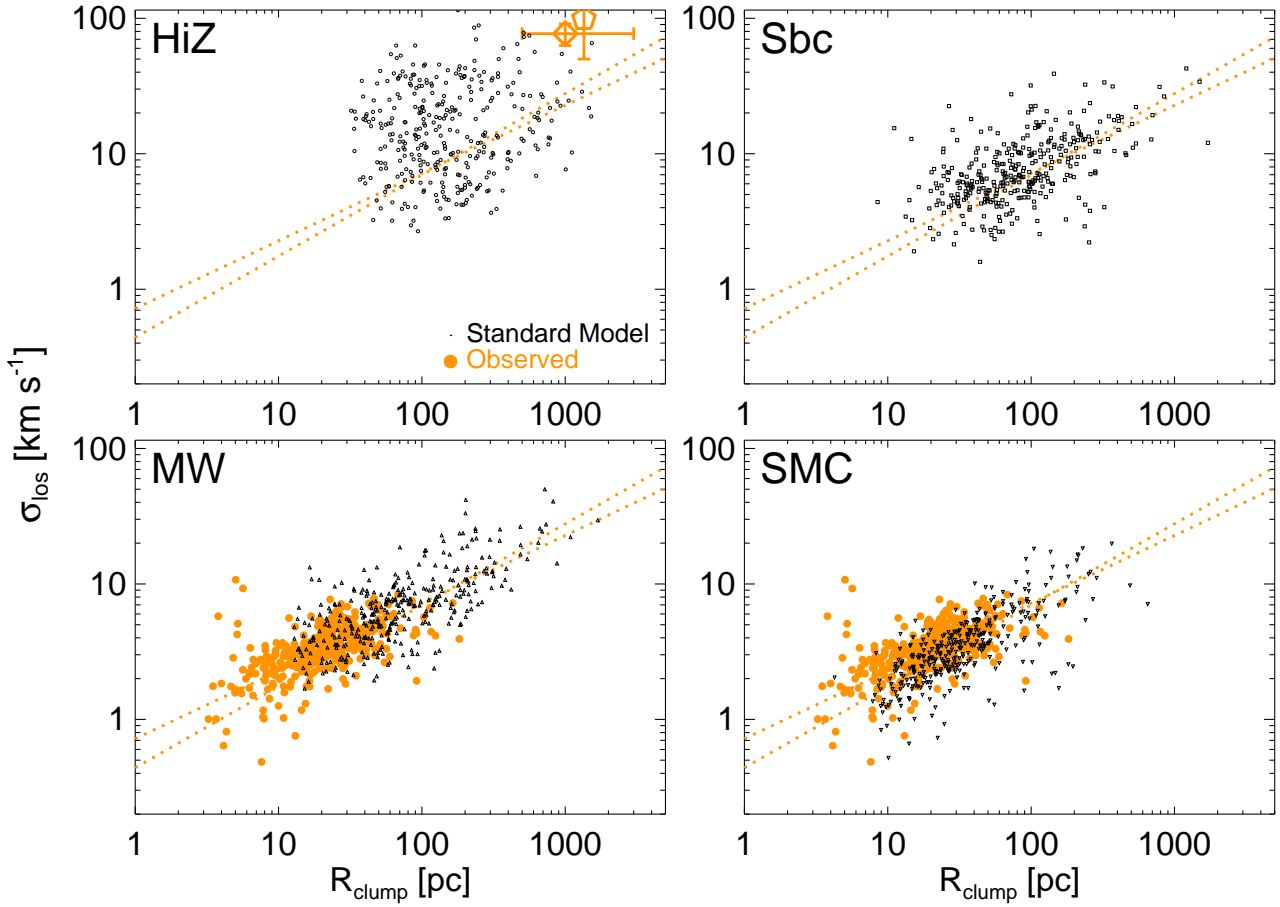


Figure 16. Linewidth-size relation of GMCs in our standard simulations of each galaxy model. We randomly sample clouds in time for each disk model. We only show clouds with > 100 member particles and sizes > 5 softening lengths (this determines the low-mass cutoff in the plots). We compare observations from local-group galaxies Bolatto et al. (2008, filled points), with typical best-fit power-laws $\sigma \propto R^{0.5-0.6}$ (dotted lines). For the HiZ case, we compare typical properties of very massive clumps observed in Förster Schreiber et al. (2009); Förster Schreiber et al. (2011) (open points). Because GMCs are short-lived, these scalings essentially reflect the initial collapse conditions, and so are relatively insensitive to feedback.

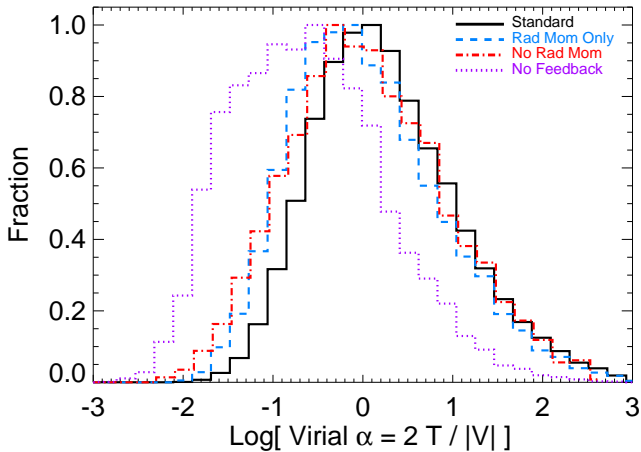


Figure 17. Predicted distribution of GMC virial parameters (the ratio of kinetic to potential energy; eqn. 13). We plot the distribution for all disk models together, since the individual results are very similar. Once sufficient feedback exists to resist collapse and make clouds relatively short-lived, all models equilibrate at marginal binding ($\alpha \sim 1$ and is only weakly correlated with feedback strength); With no feedback, however, clouds are much more tightly bound, with global $\alpha < 0.1$.

clouds, but also projection effects, since the clouds are highly non-circular. This is all expected, since we argued above that clumps dissociate before they can become strongly bound or globally contract much.

Within each cloud, there is a broad dispersion as well of “local” virial parameters. Much of the diffuse material at $\langle n \rangle$ is actually un-bound (at least \sim half the material is at $\alpha > 1$, and can reach $\alpha \sim 10 - 100$). The bulk velocity of this material, in the center of mass frame of the GMC, exceeds the cloud escape velocity. This material is associated with the clump only in a transient sense (e.g. from turbulent compression, shocks, outflows from dense regions, or convergent flows). But dense clumps with local $n > 10^4 \text{ cm}^{-3}$ (the regions that will actually form stars, but a small mass fraction) tend to be bound. This is similar to what has been inferred from observations of GMC complexes (e.g. Heyer et al. 2001). Quantitatively, we can consider the “true” α_{true} (calculated knowing the actual true kinetic and potential energy relative to the cloud center of mass for every gas particle) for two separate populations: the cloud “cores” (for convenience, gas inside the spherical half-mass radius with relative velocity below the median of the clump

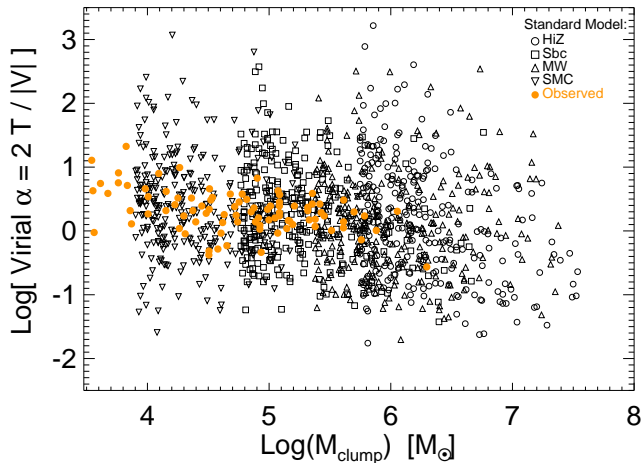


Figure 18. Correlation of the GMC virial parameter α (Figure 17) with mass for our standard simulations with all feedback mechanisms enabled. We compare the observed local group clouds from Solomon et al. (1987). The model and observations both show a weak trend in which more massive GMCs tend to be more tightly bound $\alpha \propto M_{\text{cl}}^{-0.3}$.

material), and the remaining “non-core” material; we find typical $\langle \alpha_{\text{true}} \rangle \sim 0.05 - 0.2$ and $\langle \alpha_{\text{true}} \rangle \sim 30 - 100$, respectively.¹⁰

With no feedback, clouds are at least an order-of-magnitude more tightly bound, $\alpha \sim 0.05 - 0.1$. This follows from their (largely vertical) collapse, giving smaller R and σ at the same mass (these quantities often collapse together in a way that keeps the clouds not far off the linewidth-size relation, but gives much smaller α at fixed mass). However, once sufficiently strong feedback is in place to slow/dissociate clumps, the properties are relatively insensitive to the feedback model. This is not surprising: provided sufficient energy/momentum to slow Jeans collapse and/or dissociate a cloud, objects will either globally equilibrate at marginal binding, or spend most of their lifetime at the point where infall reverses to expansion, i.e., at the maximum value of α . If the feedback operates rapidly, this minimum α will be near the value where star formation commences. This is why (as we saw with other cloud properties) models with very different assumptions and more simplified models for feedback have also seen similar characteristic α (Dobbs et al. 2011). For the HiZ case, we again find that radiation pressure momentum is most important (removing sources of hot gas has little effect). For the SMC-like case, in contrast, gas heating plays a large role in regulating the virial parameters.

Figure 18 plots the virial parameters of GMCs as a function of their mass. We show this only for our standard model, as the systematic offsets between models can easily be read off Figure 17. For comparison, we plot the observed points from Solomon et al. (1987). The simulated and observed GMCs agree well. Not only is the median α similar, but the simulations reproduce the observed weak scaling of α with M_{cl} , approximately $\alpha \propto M_{\text{cl}}^{-0.3}$, such that more massive clumps tend to be more bound (see Heyer et al. 2001). This is partly related to the fact we show below, that more massive clumps tend to have longer lifetimes. We note, however, that Figure 18 implies that large fractions of the population are really not self-gravitating – it is better in this regime to consider the

¹⁰ Note that because the “diffuse” material is a non-negligible fraction of the mass, calculating the “true” α for all cloud material often gives large values, dominated by the material which is transiently associated in shocks and has large kinetic energy.

systems as simply “molecular overdensities” rather than “clouds” in the traditional sense.

8.5 Lifetimes and Star Formation Efficiencies

We next consider typical cloud “lifetimes” and integrated star formation efficiencies. To define these, we need to link clouds in time between different snapshots. Given a specific clump p in snapshot i , we identify the descendant d of this clump (in snapshot $i + 1$) as the clump which contains the most total mass in particles from the original clump p . If no clump in snapshot $i + 1$ contains any particles from p , then the clump has no descendant (its mass becomes zero). This defines a “merger tree” for clumps with time.¹¹ To consider a “main branch” of that tree (i.e. growth of the primary clump, which may grow by accretion/inflow, or by mergers of smaller clumps), we note that if a clump d is identified with multiple progenitor clumps p , the “main progenitor” is simply the most massive. The other progenitors are marked as having “merged onto” the main branch at this time.

For each main branch, we then have a mass evolution versus time, $M_{\text{cl}}(t)$. This generally rises exponentially as the clump starts forming, then (with feedback enabled) falls rapidly as feedback unbinds the gas. We can then define other important quantities: the maximum mass of the clump (just $M_{\text{max}} = \text{MAX}(M_{\text{cl}}[t])$), and the lifetime t_{cl} . We take the latter to be the total time when the clump is above some cutoff threshold $\eta \approx 10\%$ of M_{max} – the choice is arbitrary, but because the clumps tend to grow and dissociate quickly the lifetimes are not especially sensitive to the choice so long as $\eta \ll 1$.

Figure 19 plots the distribution of the resulting clump lifetimes in our standard simulations. We plot it in absolute units and in units of the clump dynamical time, $t_{\text{dyn}} = 1/\sqrt{G\rho_{\text{cl}}}$. We do not include clumps that are lost via merger onto more massive clumps, because we cannot know how long they would have survived, but their growth/decay curves tend to be no different from main-branch clumps of similar mass and spatial locations until their merger. And we find that the majority of clouds grow primarily by accreting “smooth” gas (i.e. gas not in another massive cloud), rather than via (at least major) hierarchical mergers, so this is not a large effect.

Our simulated GMCs are short-lived: with feedback present, most live $\sim 10^6 - 10^7$ yr, $\sim 1 - 10$ free-fall times. Star formation within clouds should therefore be inefficient: we expect just a few percent of their mass will be turned into stars, but we can calculate this explicitly. We sum the SFR from all cloud particles at each time, integrated over the cloud lifetime to get the total stellar mass formed, and compare this to the maximum clump mass (defining the efficiency $M_{\text{*,formed}}/M_{\text{cloud,max}}$). The typical cloud converts $\sim 1 - 10\%$ of its peak mass into stars, similar to what has been inferred from a range of observations (Zuckerman & Evans 1974; Williams & McKee 1997; Evans 1999; Evans et al. 2009). This does not necessarily mean, however, that this fraction of all mass that enters the cloud is converted into stars. Over the cloud lifetime, mass is continuously accreted and lost, so the total mass in gas that gets processed “through” the cloud can be even larger, implying an even lower net “efficiency” of converting GMC material to stars.

¹¹ To properly sample this requires that the snapshot time spacing be less than typical clump lifetimes. We have experimented with spacings as short as 10^5 yr, and generally find converged results for the lifetime statistics presented here for spacings $\lesssim 10^6$ yr.

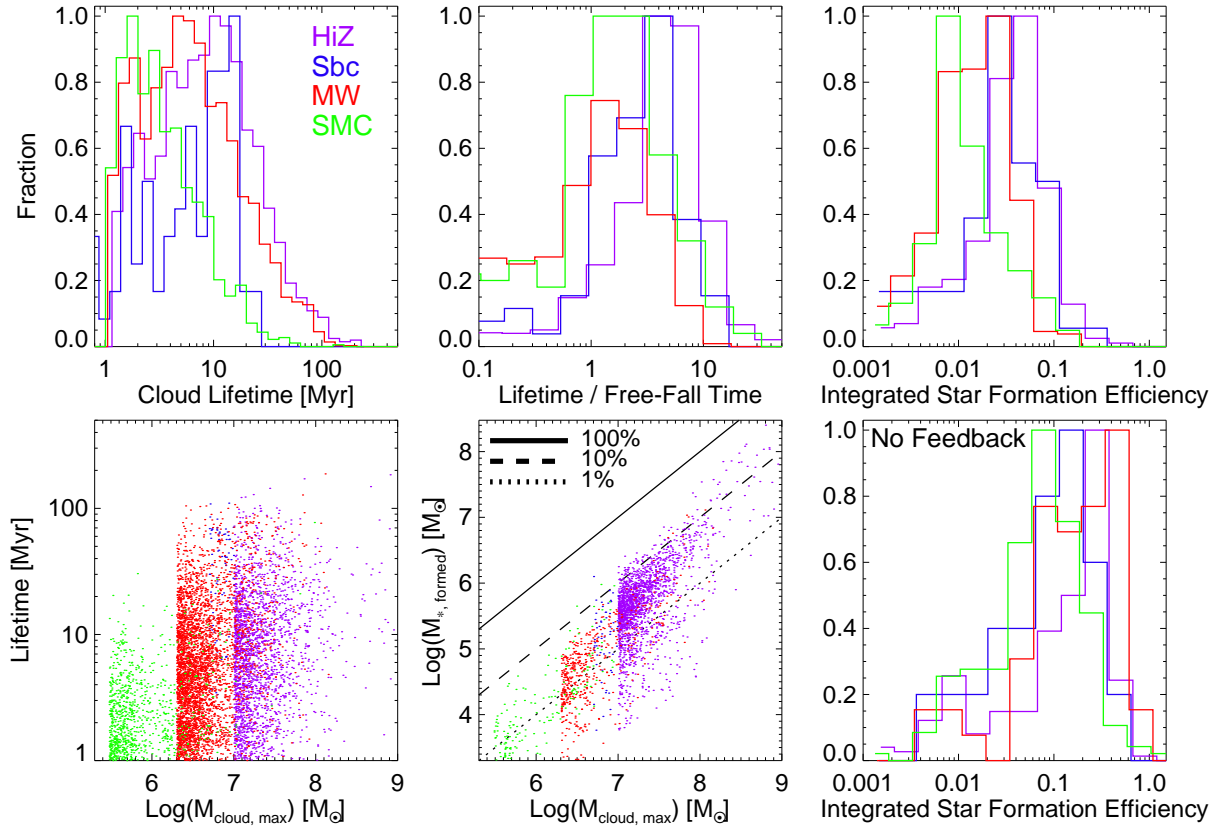


Figure 19. Statistics of cloud lifetimes and star formation efficiencies in our standard simulations with all feedback mechanisms enabled. For each simulation, we identify all clumps that can be well-resolved (> 100 particles) down to 10% of the clump mass (> 1000 particles at peak); lifetime is defined as the time above 10% the maximum cloud mass. *Top Left:* Distribution of cloud lifetimes t_{cl} for each of our galaxy models. *Top Center:* Lifetimes relative to the free-fall time t_{cl}/t_{ff} of each cloud. *Top Right:* Integrated star formation efficiency (stellar mass formed in clump over maximum cloud mass). *Bottom Left:* Lifetime versus maximum cloud mass. *Bottom Center:* Stellar mass formed versus maximum mass. Lines correspond to the different efficiencies labeled. Clouds live for a few dynamical times, and turn a few percent of their mass into stars. There is also a weak trend for more massive systems to have higher efficiencies and longer lifetimes. *Bottom Right:* Integrated star formation efficiency (as *top right*), but in models with no feedback. Without feedback, clouds persist until most of their dense gas is turned into stars, giving star formation efficiencies of $\sim 10 - 50\%$ on timescales of ~ 10 Myr.

What sets the efficiencies and lifetimes of GMCs? As we discussed above, for the *dense* gas, the most important feedback mechanism is the local radiation pressure. Therefore consider just this, for simplicity, in a spherically symmetric cloud of mass M and projected effective radius R_e . The total gravitational force in a GMC (summing over mass) is

$$F_{\text{grav}} = \frac{GM^2}{\beta_1 R_e^2} \quad (14)$$

where $\beta_1 \sim 1$ depends on the mass profile. The force from radiation pressure, integrated over the sphere, is

$$F_{\text{rad}} = (1 + \tau_{\text{IR}}) \frac{L}{c} \quad (15)$$

where the pre-factor assumes the cloud is optically thick in the UV/optical, but not necessarily in the IR. If the lifetimes are short, of order a few Myr, then $L \propto M_*$, because most SNe have not exploded; for a standard stellar population with the same IMF assumptions as our models, $L \approx 1137 L_{\odot} (M_*/M_{\odot})$. Since the average surface density of clouds is within a narrow range, it is convenient to define $\langle \Sigma \rangle = \beta_2 M / (\pi R_e^2)$ ($\langle \Sigma \rangle$ is the mass-weighted average Σ , β_2 again just depends on the mass profile). Setting $F_{\text{grav}} = F_{\text{rad}}$, we obtain

$$\frac{M_*}{M_{\text{cloud}}} \approx 0.04 \beta_{0.7} \frac{\langle \Sigma \rangle_{100}}{1 + \tau_{\text{IR}}} \quad (16)$$

where $\beta_{0.7} = (\beta_1 \beta_2)^{-1}/0.7$ ($= 0.95, 1.07, 1.12$ for a constant-density, Plummer, or Hernquist 1990 profile) and $\langle \Sigma \rangle_{100} = \langle \Sigma \rangle / 100 M_{\odot} \text{pc}^{-2}$.

This simple argument reproduces the efficiencies at low cloud masses, where these assumptions hold, and τ_{IR} is small, for the typical observed average surface densities of such clouds ($\langle \Sigma \rangle_{100} \sim 1$). The predicted efficiency does increase at higher $\langle \Sigma \rangle$, which could in principle lead to a runaway collapse if there were no offsetting force. However, at sufficiently high $\Sigma \gtrsim 1000 M_{\odot} \text{pc}^{-3}$, τ_{IR} becomes larger than unity even for the smoothed average surface density. More accurately the typical $\tau_{\text{IR}} \approx c^2 \kappa_{\text{IR}} \langle \Sigma \rangle$ where c^2 is a “clumping fudge factor” that accounts for the excess rise in density around each stellar cluster/core sub-region, a well as contributions from other feedback mechanisms (typical effective $c \sim 2 - 5$).

Once $\tau_{\text{IR}} \gg 1$, the efficiency should asymptote to a maximum

$$\frac{M_*}{M_{\text{cloud}}} \rightarrow 0.4 c^{-2} \beta_{0.7} \kappa_5^{-1} \quad (\tau_{\text{IR}} \gg 1) \quad (17)$$

where $\kappa_5 = \kappa_{\text{IR}} / 5 \text{cm}^2 \text{g}^{-1} \sim 1$. Given modest $c \sim$ a couple, and the fact that our simulations rarely reach such extreme densities, this matches reasonably well the “upper limit” to the star formation efficiencies we find; together, these values bracket the range in the simulations.

Cloud lifetimes follow from these integrated efficiencies, as

the time needed to form this number of stars, $\Delta t = M_*/\dot{M}_*(\text{cloud})$. For an observed instantaneous SFR of a one or two percent per free-fall time, it takes a few free-fall times to form this mass and disrupt the cloud (in this limit, of course, we insert this efficiency in our SFR model, so the lifetime is not predicted in a fully a priori sense). However, in Paper I, we showed that the *global* star formation rate did not depend on the efficiency employed in our model. Since it takes a free-fall time to assemble a GMC, and a free-fall time to disrupt it, even if we assume a large efficiency, the cloud will live one to two free fall times.

In the most massive cloud complexes, the lifetime reaches as large as $\gtrsim 30\text{Myr}$ and is no longer short compared to stellar evolution timescales. Since massive stars are dying, instead of $L \propto M_*$, we have $L \propto \dot{M}_*$. In this limit, for a constant star formation rate $L/\dot{M}_* \approx 5.7 \times 10^9 L_\odot / (M_\odot \text{yr}^{-1})$. Inserting this into the derivation above requires an instantaneous SFR $\dot{M}_* \approx 0.8 M_\odot \text{yr}^{-1} (M_{\text{cloud}}/10^8 M_\odot) \beta_{0.7} \langle \Sigma \rangle_{100} (1 + \tau_{\text{IR}})^{-1}$. This then requires a time $t_{\text{lifetime}} \sim t_{\text{dyn}}$ to dissociate the cloud (and must act in less than a few dynamical times so the momentum is not dissipated); if we require the total momentum injected at this rate equal the binding momentum of the cloud, we obtain $t_{\text{lifetime}} \approx 1.4 \beta' t_{\text{ff}}$ (where β' again depends very weakly on the mass profile and $\langle t_{\text{ff}} \rangle \equiv (3\pi/32 \langle \rho \rangle)^{1/2}$), giving

$$\frac{M_*}{M_{\text{cloud}}} \approx 0.04 \beta' \frac{\langle \Sigma \rangle_{100}}{1 + \tau_{\text{IR}}} \left(\frac{t_{\text{ff}}}{4\text{Myr}} \right) \quad (18)$$

$$\approx 0.04 \beta'' \frac{\langle \Sigma \rangle_{100}^{1/2}}{1 + \tau_{\text{IR}}} \left(\frac{R_e}{10\text{pc}} \right)^{1/2} \quad (19)$$

Note that for similar- $\langle \Sigma \rangle$ clouds, the characteristic dynamical time increases with cloud mass as $t_{\text{ff}} \propto R_e^{0.5} \propto M_{\text{cloud}}^{0.25}$. We therefore expect more massive clouds to have larger absolute lifetimes, a correlation clearly evident in Figure 19. Moreover, according to Equation 18, the integrated star formation efficiency (in massive clouds, at least) should also be a weakly increasing function of the cloud mass $\propto M_{\text{cloud}}^{0.25}$. We also see this trend in our simulations, with efficiencies rising from $\approx 1\%$ to $\approx 10\%$ from $M_{\text{cl}} \lesssim 10^5 M_\odot$ to $M_{\text{cl}} \gtrsim 10^8 M_\odot$, or $M_{*,\text{formed}}/M_{\text{cloud,max}} \propto M_{\text{cloud,max}}^{(0.2-0.3)}$ (see also the discussion in Murray et al. 2010).

Figure 19 compares the cloud star formation efficiencies in runs without feedback. In *absolute* units, the lifetimes are not necessarily much longer – many live $\sim 10\text{Myr}$; however the population with lifetimes $\sim 1\text{Myr}$ disappears and a large tail of clouds (often in global structures such as spiral arms) appears with lifetimes $\sim 100\text{Myr}$. But, recall that in the feedback-free cases, the dense gas collapses rapidly. As such, the range of lifetimes in units of the free-fall time $\propto \rho^{-1/2}$ is much more broad, with clumps living as long as $\sim 10 - 100 t_{\text{ff}}$. The distributions are very broad because it is often local regions within the clump running away to high densities, so the average $\langle \rho \rangle$ may or may not reflect this to varying degrees in a cloud. The more robust indicator is the integrated star formation efficiencies. As expected, from the runaway global SFR in these models, the star formation efficiency per-cloud is $\sim 10 - 100\%$, with a mean of $\sim 40\%$ (it is not 100% because there is always some low-density material associated with clouds, which is left at even lower densities once dense regions have all collapsed). Feedback is necessary to reproduce the observed per-cloud cloud lifetimes and star formation efficiencies.

Considering each feedback mechanism in turn, our results essentially mirror those for the cold gas and GMC density distributions. In all models, radiation pressure is important to resist collapse; removing it in the HiZ case gives results nearly identical

to the feedback-free case. And runs in all models with *only* radiation pressure enabled give similar results. In the MW and SMC cases, gas heating on $\sim 1\text{Myr}$ timescales from “fast” stellar winds and photo-ionization can contribute comparably to cloud dissociation (removing radiation pressure does not result in total collapse if they remain, though the average star formation efficiency is slightly higher), and the longer-lived clouds in these models tend to be dissociated when SNe turn on (a few Myr).

9 DISCUSSION

We have implemented a model for stellar feedback in SPH simulations of galaxies that incorporates physically motivated treatments of a number of the key feedback processes: radiation pressure from UV, optical, and IR photons; the momentum injection, gas heating, and gas recycling from SNe (Types I & II) and stellar winds; and HII photoionization-heating. Our treatment of radiation pressure is calibrated by comparison to more detailed radiative transfer calculations (Appendix A). Our model of the ISM also includes molecular cooling, a simple treatment of HII destruction, and allows star formation only at very high densities within giant molecular clouds ($n \gg 100 \text{cm}^{-3}$).

In this paper, we study the consequences of these feedback models for the global structure of the ISM in disk galaxies (velocity dispersions, Toomre Q , etc), the phase structure of the ISM, and the properties of GMCs. We simulate four representative galaxy models to bracket the diversity of star-forming galaxies observed locally and at high redshift (Table 2; Figs. 1-5). In a companion paper, we study the galaxy-scale outflows driven by stellar feedback and show that galactic winds appear to remove the bulk of the gas from their host galaxies.

With physically plausible stellar feedback mechanisms enabled, we show that star-forming galaxies generically approach a quasi steady-state in which the properties of the ISM are self-regulated by the turbulence driven by stellar feedback. GMCs form by self-gravity and survive for a few dynamical times before they are disrupted by stellar feedback; during this time, GMCs turn a few percent of their mass into stars (Fig. 19). The resulting galaxy-integrated star formation rates are in reasonable agreement with the Kennicutt-Schmidt law (Fig. 7; see also Paper I) and the global galaxy properties (dispersion, scale heights, Toomre Q parameter; Fig. 9) and phase distribution (Fig. 11) of the ISM are consistent with observations.

The ISM phase distributions calculated in this paper are of course still limited in accuracy both by standard numerical restrictions and by the inability of any galaxy-scale calculation to capture small-scale mixing processes and the effects of (saturated) thermal conduction. Nonetheless, much of the ISM dynamics and phase structure we find is a consequence of supersonic turbulence driven by stellar feedback. Such turbulence is reasonably well modeled numerically by SPH (based on comparisons to grid-based methods; e.g., Kitsionas et al. 2009; Price & Federrath 2010; Bauer & Springel 2011). Based on this and preliminary comparison with other codes, we expect that the inclusion or exclusion of different feedback mechanisms will result in much larger differences than the details of the numerical method.

9.1 The Problems of Feedback-Free Models

The structure of the ISM in the presence of stellar feedback is markedly different than in calculations that do not have any stellar feedback. In the latter case, the gas rapidly radiates away its vertical

thermal support and any gravitationally-induced turbulent fluctuations are damped on a crossing time. This leads to runaway collapse of the gas and star formation well in excess of the Kennicutt-Schmidt relation ($\dot{M}_* \sim M_{\text{gas}}/t_{\text{dyn}}$; Fig. 7). Dense star-forming regions within GMCs collapse without limit, producing a large non-lognormal excess of high-density gas (Fig. 12). These GMCs have very low virial parameters relative to observations (Fig. 17) and turn $\sim 10 - 50\%$ of their gas into stars into just a few cloud dynamical times (Fig. 19).

In other words, turbulence from global gravitational instabilities and the collapse of GMCs does not appear sufficient to maintain low star formation efficiencies and prevent runaway collapse of the ISM (neither globally nor within GMCs). This result has been found in other simulations with sufficiently high resolution to follow individual GMCs (see e.g. Bournaud et al. 2010; Tasker 2011; Dobbs et al. 2011). Although our calculations do not include inflow of gas from the IGM and thus we cannot explicitly assess whether such accretion can help maintain turbulence in galactic disks, the fact that the runaway is *local*, and occurs even while the disk maintains a large nominal gas velocity dispersion, suggests that gas inflow will not change these conclusions.

We caution that some properties of the ISM can be reasonable in feedback-free models, but for the wrong reasons. For example, without feedback disks still eventually reach $Q \sim 1$ (Fig. 9); this is true even without star formation so long as cooling is included. However, without feedback this occurs because of two processes that do not occur in real galaxies: first, all of the dense gas rapidly turns into stars, leaving only a small, tenuous gas mass behind that can more easily maintain $Q \sim 1$; second, in doing so, the dense gas collapses without limit to $\gtrsim 10^6 \text{ cm}^{-3}$ regions that become so small that they dynamically act like the collisionless stellar disks.

In our simulations without stellar feedback, the *global* collapse of GMCs is eventually arrested by angular momentum.¹² The resulting GMCs have roughly similar median surface densities and Larson’s law scalings to models with feedback (Fig. 15), but dynamically the GMCs are rotationally supported disks instead of triaxial clouds. Moreover three-dimensional collapse still runs away, especially in dense sub-regions. Thus the median surface densities of GMCs are similar with and without feedback, but the mass in dense molecular gas and the per-cloud SFRs are an order-of-magnitude larger in the absence of feedback. Finally, while clouds can in many cases be disrupted over $\sim 10 \text{ Myr}$ by shear in the disk, during this time the runaway collapse of the gas has turned an order-unity fraction of the GMC mass into stars (Fig. 19). As a result, although models without feedback can give rise to $Q \sim 1$ disks with several observed disk and GMC scaling relations, gravity alone cannot (in our calculations) regulate the structure of the ISM in a way that is similar to models with explicit stellar feedback.

9.2 How Does Feedback Regulate Star Formation?

What maintains the low star formation efficiency in the presence of feedback? One interpretation is that the instantaneous star formation efficiency of $\sim 1\%$ per dynamical time can be explained as a consequence of the statistics of the lognormal turbulent density field (Nordlund & Padoan 1999; Vázquez-Semadeni et al. 2003; Li et al. 2004; Krumholz & McKee 2005). More recent – and much higher resolution – numerical work has highlighted, however, that

star formation in such models proceeds more rapidly than previously appreciated ($\sim 30\%$ per dynamical time) if turbulence is driven solely on large scales (Padoan & Nordlund 2011). In these calculations, the rate of star formation is indeed set by the mass of gas above a critical density that can collapse; however, when self-gravity and rapid cooling are included in simulations with sufficient dynamic range, self-gravitating regions can “detach” from the large scale flow and collapse without limit. Even if their internal instantaneous SFR per dynamical time remains low, such self-gravitating regions quickly reach such high densities (short t_{dyn}) that the global SFR per dynamical time becomes much larger than observed.

This dynamical decoupling of high density regions is very similar to what occurs in our simulations without feedback. Recall, these maintain a similar large-scale velocity dispersion as models with feedback. Bournaud et al. (2010) also explicitly showed that high-resolution galaxy models with and without feedback maintain similar turbulent power spectra, but that the turbulent cascade from large scales is unable to dissociate clumps on small scales once they have become self-gravitating. This leads to large deviations from a lognormal density distribution (Fig. 12), which leads to a star formation efficiency that is an order of magnitude larger than observed.

The difficulties of models in which turbulence is driven solely on large scales (via self-gravity or some other mechanism) points to the critical role of stellar feedback processes that can regulate star formation on *small* scales (e.g., by disrupting GMCs). Moreover, the high star formation efficiency found in high-resolution “turbulent box” simulations and feedback-free galaxy simulations suggests that the feedback required to dissociate dense, self-gravitating regions (GMCs and cores within them) regulates the SFR rather differently than simple homogeneous turbulence driven on large scales.

Which feedback mechanisms prevent the runaway collapse seen in the no-feedback models and in models in which turbulence is driven solely on large scales? We show that this depends on the physical properties of the galaxy model, in particular the density of the ISM. In high-density regions (typical of the global ISM of starbursts and high-redshift galaxies and the interiors of GMCs), we find that radiation pressure is the dominant feedback mechanism (especially multiple-scatterings of IR photons). Lower-mass clouds (more prevalent in the MW and SMC models), with lower mean densities, can be similarly disrupted by HII photoionization (e.g., Matzner 2002). In Paper I we showed that radiation pressure alone leads to galaxy models that lie roughly along the Kennicutt-Schmidt relation; including the additional feedback mechanisms in this paper typically results in smaller (factor $\sim 2 - 3$) global SFRs by suppressing the collapse of gas into GMCs and by expelling more gas in galactic winds. However, these additional feedback mechanisms have relatively little effect on the integrated lifetimes or star formation efficiencies of GMCs themselves.

In lower-density regions of the ISM (typical of MW-like systems and dwarf galaxies), *global* self-regulation is much more strongly affected by heating processes (Fig. 7). Removing radiation pressure in these regimes can still lead to runaway collapse of the dense star-forming gas. However, although dense regions run away, the feedback from the resulting star formation can act on the remaining lower-density gas to limit further collapse and help globally regulate the star formation. Overall, SNe are the most important heating mechanism, since their integrated energetics dominate over stellar winds and photoionization-heating; however, within GMCs, stellar winds and photo-ionization are typically more im-

¹² This collapse might be very different in the presence of magnetic fields which can torque the GMCs and remove this angular momentum.

portant because they act on \lesssim Myr timescales while SNe do not explode until a few Myr later – longer than the GMC lifetime.

9.3 Generic Consequences of Strong Stellar Feedback

As discussed in §9.1, we find that gaseous star-forming disks robustly self-regulate at $Q \sim 1$, which in turn sets the required velocity dispersion σ and the disk scale height (Fig. 9). This is independent of the details of feedback coupling mechanisms. In particular, energy/momentum input in excess of what is needed for $Q \sim 1$ will be “lost” (in e.g. galactic winds) or eventually dissipated (since cooling times are short), and any gas with $Q \ll 1$ will collapse, turning into stars and triggering more efficient feedback.

Likewise, we find that the properties of GMCs largely reflect the conditions for gravitational collapse starting from a $Q \sim 1$ disk. More precisely, this is true provided that feedback makes GMCs relatively short-lived, so that their instantaneous conditions are not that different from those “at formation.” In this context the $\sim M^{-2}$ mass function of GMCs is a consequence of the scale-free nature of gravity, with a cutoff near the global Jeans mass (Fig. 14). The observed size-mass and linewidth-size ($\delta v \propto R^{0.5}$) relations of GMCs reflect conditions for collapse in a supersonically turbulent $Q \sim 1$ disk (Figs. 15-16). This in turn requires a weak dependence of GMC densities on the mean density of the galactic disk, such that the linewidth-size relation normalization scales with the surface density of the disk as $\delta v/R^{0.5} \propto \Sigma^{0.5}$.

The fact that the GMC properties – and some of the average disk properties – are largely determined by the conditions for gravitational collapse accounts for why other calculations with different physics reproduce many of the same GMC/disk properties. The key criterion is that feedback is sufficient to both disrupt GMCs and maintain the ISM in a marginally stable state against collapse. If this can be satisfied, galaxy-averaged SFRs are set by the number of young stars needed to supply the necessary feedback, independent of how those stars form. As a result, the global SFR – and thus the global Schmidt-Kennicutt law – emerges relatively independent of the assumed micro-scale (high density) star formation law, density threshold, or efficiency. In Paper I we varied these parameters widely and explicitly showed they have no effect on the SFR. Here, we similarly find that explicit models for molecular chemistry in the local SFR and cooling function have no effect on the SFR for the galaxies we model (Fig. 8).

In low-resolution numerical simulations, an explicit treatment of the molecular fraction can make large differences to the SFR, because such models are really implicit models for the fraction of gas at high densities. But in our calculations GMCs are resolved, and star formation occurs only at the highest densities within them ($n \gg 100 \text{ cm}^{-3}$), which are already overwhelmingly molecular. At our resolution, in fact, most molecular gas is non-star forming. As long as a cooling channel is available, gas will eventually collapse to the densities needed to self-shield and form sufficient young stars to regulate the galaxies’ SFR via feedback. An explicit treatment of the molecular chemistry is thus only dynamically important at low enough metallicities that the cooling time by any channel becomes long relative to the dynamical time, roughly $Z \ll 0.01 Z_{\odot}$ (see also Glover & Clark 2012.)

These conclusions are reassuring in the sense that they suggest that our models are unlikely to be inaccurate on large scales, even if they are still missing some important physics. For example, magnetic fields and/or cosmic rays may contribute comparably to the ISM pressure in many galaxies. However, given that our results are robust to variations in the “microphysics” of how, precisely, feed-

back and cooling are implemented – and self-regulation at $Q \sim 1$ implies they will, in equipartition, contribute only $\sim 10 - 30\%$ level corrections to the SFR needed to maintain stability – they are unlikely to significantly alter our conclusions.

The phase structure of the ISM is much more sensitive to the microphysics of stellar feedback than global disk or GMC properties. Without feedback, there is a runaway collapse of some of the gas at the highest resolvable densities $n \gg 10^4 \text{ cm}^{-3}$, even though the amount of gas in GMCs and at modest densities $n \sim 1 - 100 \text{ cm}^{-3}$ is similar to models with feedback (Fig. 12). Based on the calculations in this paper and in Paper I we conclude that the fraction of the ISM mass at high densities varies continuously with feedback strength, with more efficient feedback implying less gas at high densities (e.g., Fig. 8 of Paper I). This is because the SFR itself adjusts depending on the efficiency of feedback and the SFR is set by the amount of mass in the high density ISM. The dense gas is particularly sensitive to radiation pressure: removing this support allows GMCs to collapse to much smaller radii and higher densities, particularly in high surface density systems where photoionization feedback is less effective (Fig. 6 & 15). These results strongly suggest that observational probes of high density molecular gas (e.g., HCN) are particularly sensitive probes of the dominant stellar feedback mechanisms in galaxies. We will pursue this connection quantitatively in future work.

ACKNOWLEDGMENTS

We thank Dusan Keres, Todd Thompson, and Lars Hernquist for helpful discussions. Support for PFH was provided by the Miller Institute for Basic Research in Science, University of California Berkeley. EQ is supported in part by the David and Lucile Packard Foundation. NM is supported in part by NSERC and by the Canada Research Chairs program.

REFERENCES

- Audit, E., & Hennebelle, P. 2010, *A&A*, 511, A76+
- Avila-Reese, V., Colín, P., González-Samaniego, A., Valenzuela, O., Firmani, C., Velázquez, H., & Ceverino, D. 2011, *ApJ*, 736, 134
- Ballesteros-Paredes, J., Klessen, R. S., Mac Low, M.-M., & Vazquez-Semadeni, E. 2007, in *Protostars and Planets V*, University of Arizona Press, Tucson, ed. B. Reipurth, D. Jewitt, & K. Keil, 63–80
- Ballesteros-Paredes, J., Vazquez-Semadeni, E., Gazol, A., Hartmann, L. W., Heitsch, F., & Colin, P. 2011, *MNRAS*, 416, 1436
- Bauer, A., & Springel, V. 2011, *MNRAS*, in press, arXiv:1109.4413
- Bell, E. F., & de Jong, R. S. 2001, *ApJ*, 550, 212
- Bolatto, A. D., Leroy, A. K., Rosolowsky, E., Walter, F., & Blitz, L. 2008, *ApJ*, 686, 948
- Bond, J. R., Cole, S., Efstathiou, G., & Kaiser, N. 1991, *ApJ*, 379, 440
- Bournaud, F., Elmegreen, B. G., & Elmegreen, D. M. 2007, *The Astrophysical Journal*, 670, 237
- Bournaud, F., Elmegreen, B. G., Teyssier, R., Block, D. L., & Puerari, I. 2010, *MNRAS*, 409, 1088
- Buat, V., et al. 2007, *ApJS*, 173, 404
- Ceverino, D., & Klypin, A. 2009, *ApJ*, 695, 292
- Chevalier, R. A., & Gardner, J. 1974, *ApJ*, 192, 457
- Cole, S., Lacey, C. G., Baugh, C. M., & Frenk, C. S. 2000, *MNRAS*, 319, 168

- Colín, P., Avila-Reese, V., Vázquez-Semadeni, E., Valenzuela, O., & Ceverino, D. 2010, *ApJ*, 713, 535
- Cortese, L., et al. 2006, *ApJ*, 637, 242
- Dobbs, C. L. 2008, *MNRAS*, 391, 844
- Dobbs, C. L., Burkert, A., & Pringle, J. E. 2011, *MNRAS*, 413, 528
- Erb, D. K., Steidel, C. C., Shapley, A. E., Pettini, M., Reddy, N. A., & Adelberger, K. L. 2006, *ApJ*, 646, 107
- Evans, N. J., et al. 2009, *ApJS*, 181, 321
- Evans, II, N. J. 1999, *ARA&A*, 37, 311
- Federrath, C., Klessen, R. S., & Schmidt, W. 2008, *ApJL*, 688, L79
- Förster Schreiber, N. M., et al. 2006, *ApJ*, 645, 1062
- Forster Schreiber, N. M., et al. 2009, *ApJ*, 706, 1364
- Förster Schreiber, N. M., et al. 2011, *ApJ*, 739, 45
- Fukui, Y., Kawamura, A., Minamidani, T., Mizuno, Y., Kanai, Y., Mizuno, N., Onishi, T., Yonekura, Y., Mizuno, A., Ogawa, H., & Rubio, M. 2008, *ApJS*, 178, 56
- Genzel, R., et al. 2008, *ApJ*, 687, 59
- Glover, S. C. O., & Clark, P. C. 2012, *MNRAS*, 2154
- Goodman, A. A., Pineda, J. E., & Schnee, S. L. 2009, *ApJ*, 692, 91
- Governato, F., et al. 2007, *MNRAS*, 374, 1479
- Harper-Clark, E., & Murray, N. 2011, in *Computational Star Formation*; Cambridge University Press, ed. J. Alves, B. G. Elmegreen, J. M. Girart & V. Trimble, Vol. 270 (Cambridge, UK: Cambridge University Press), 235–238
- Hernquist, L. 1990, *ApJ*, 356, 359
- Heyer, M., Krawczyk, C., Duval, J., & Jackson, J. M. 2009, *ApJ*, 699, 1092
- Heyer, M. H., Carpenter, J. M., & Snell, R. L. 2001, *ApJ*, 551, 852
- Hopkins, P. F., Hernquist, L., Martini, P., Cox, T. J., Robertson, B., Di Matteo, T., & Springel, V. 2005, *ApJL*, 625, L71
- Hopkins, P. F., Quataert, E., & Murray, N. 2011a, *MNRAS*, 417, 950
- . 2011b, *MNRAS*, in press, arXiv:1110.4638 [astro-ph]
- Iglesias-Páramo, J., et al. 2006, *ApJS*, 164, 38
- Imara, N., Bigiel, F., & Blitz, L. 2011, *ApJ*, 732, 79
- Jonsson, P. 2006, *MNRAS*, 372, 2
- Jonsson, P., Groves, B., & Cox, T. J. 2009, *MNRAS*, in press [arXiv:0906.2156]
- Katz, N., Weinberg, D. H., & Hernquist, L. 1996, *ApJS*, 105, 19
- Kennicutt, Jr., R. C. 1998, *ApJ*, 498, 541
- Kitsionas, S., et al. 2009, *A&A*, 508, 541
- Koda, J., Sawada, T., Hasegawa, T., & Scoville, N. Z. 2006, *ApJ*, 638, 191
- Kroupa, P. 2002, *Science*, 295, 82
- Krumholz, M. R., & Gnedin, N. Y. 2011, *ApJ*, 729, 36
- Krumholz, M. R., Klein, R. I., & McKee, C. F. 2011, *ApJ*, 740, 74
- Krumholz, M. R., & McKee, C. F. 2005, *ApJ*, 630, 250
- Krumholz, M. R., & Tan, J. C. 2007, *ApJ*, 654, 304
- Kuhlen, M., Krumholz, M., Madau, P., Smith, B., & Wise, J. 2011, *ApJ*, in press arXiv:1105.2376
- Leitherer, C., et al. 1999, *ApJS*, 123, 3
- Li, P. S., Norman, M. L., Mac Low, M.-M., & Heitsch, F. 2004, *ApJ*, 605, 800
- Li, Z.-Y., & Nakamura, F. 2006, *ApJL*, 640, L187
- Mac Low, M.-M., & Klessen, R. S. 2004, *Reviews of Modern Physics*, 76, 125
- Mannucci, F., Della Valle, M., & Panagia, N. 2006, *MNRAS*, 370, 773
- Matzner, C. D. 2002, *ApJ*, 566, 302
- McGaugh, S. S. 2005, *ApJ*, 632, 859
- McKee, C. F., & Ostriker, E. C. 2007, *ARA&A*, 45, 565
- McKee, C. F., & Ostriker, J. P. 1977, *ApJ*, 218, 148
- Murray, N., Quataert, E., & Thompson, T. A. 2010, *ApJ*, 709, 191
- Noll, S., Burgarella, D., Giovannoli, E., Buat, V., Marcellac, D., & Muñoz-Mateos, J. C. 2009, *A&A*, 507, 1793
- Nordlund, Å. K., & Padoan, P. 1999, in *Interstellar Turbulence*; Cambridge University Press, ed. J. Franco & A. Carraminana (Cambridge, UK: Cambridge University Press), 218–+
- Ostriker, E. C., Gammie, C. F., & Stone, J. M. 1999, *ApJ*, 513, 259
- Ostriker, E. C., McKee, C. F., & Leroy, A. K. 2010, *ApJ*, 721, 975
- Ostriker, E. C., Stone, J. M., & Gammie, C. F. 2001, *ApJ*, 546, 980
- Padoan, P., & Nordlund, Å. 2011, *ApJ*, 730, 40
- Padoan, P., Nordlund, A., & Jones, B. J. T. 1997, *MNRAS*, 288, 145
- Pei, Y. C. 1992, *ApJ*, 395, 130
- Pilkington, K., Gibson, B. K., Calura, F., Brooks, A. M., Mayer, L., Brook, C. B., Stinson, G. S., Thacker, R. J., Few, C. G., Cunnama, D., & Wadsley, J. 2011, *MNRAS*, 417, 2891
- Pineda, J. E., Rosolowsky, E. W., & Goodman, A. A. 2009, *ApJL*, 699, L134
- Press, W. H., & Schechter, P. 1974, *ApJ*, 187, 425
- Price, D. J., & Federrath, C. 2010, *MNRAS*, 406, 1659
- Price, D. J., Federrath, C., & Brunt, C. M. 2011, *ApJL*, 727, L21
- Reddy, N. A., Steidel, C. C., Pettini, M., Adelberger, K. L., Shapley, A. E., Erb, D. K., & Dickinson, M. 2008, *ApJS*, 175, 48
- Robertson, B. E., & Kravtsov, A. V. 2008, *ApJ*, 680, 1083
- Rosolowsky, E. 2005, *PASP*, 117, 1403
- Rosolowsky, E., Engargiola, G., Plambeck, R., & Blitz, L. 2003, *ApJ*, 599, 258
- Sargsyan, L. A., & Weedman, D. W. 2009, *ApJ*, 701, 1398
- Scalo, J., Vazquez-Semadeni, E., Chappell, D., & Passot, T. 1998, *ApJ*, 504, 835
- Solomon, P. M., Rivolo, A. R., Barrett, J., & Yahil, A. 1987, *ApJ*, 319, 730
- Somerville, R. S., & Primack, J. R. 1999, *MNRAS*, 310, 1087
- Springel, V. 2005, *MNRAS*, 364, 1105
- Springel, V., White, S. D. M., Tormen, G., & Kauffmann, G. 2001, *MNRAS*, 328, 726
- Stinson, G., Seth, A., Katz, N., Wadsley, J., Governato, F., & Quinn, T. 2006, *MNRAS*, 373, 1074
- Swinbank, A. M., Papadopoulos, P. P., Cox, P., Krips, M., Ivison, R. J., Smail, I., Thomson, A. P., Neri, R., Richard, J., & Ebeling, H. 2011, *ApJ*, 742, 11
- Tacconi, L. J., et al. 2010, *Nature*, 463, 781
- Takeuchi, T. T., Buat, V., Heinis, S., Giovannoli, E., Yuan, F., Iglesias-Páramo, J., Murata, K. L., & Burgarella, D. 2010, *A&A*, 514, A4+
- Tasker, E. J. 2011, *ApJ*, 730, 11
- Tasker, E. J., & Tan, J. C. 2009, *ApJ*, 700, 358
- Teyssier, R., Chapon, D., & Bournaud, F. 2010, *ApJL*, 720, L149
- Thacker, R. J., & Couchman, H. M. P. 2000, *ApJ*, 545, 728
- Torrey, P., Cox, T. J., Kewley, L., & Hernquist, L. 2012, *ApJ*, 746, 108
- Vazquez-Semadeni, E. 1994, *ApJ*, 423, 681
- Vázquez-Semadeni, E., Ballesteros-Paredes, J., & Klessen, R. S. 2003, *ApJL*, 585, L131
- Williams, J. P., & McKee, C. F. 1997, *ApJ*, 476, 166
- Wong, T., et al. 2008, *MNRAS*, 386, 1069

Zuckerman, B., & Evans, II, N. J. 1974, ApJL, 192, L149

APPENDIX A: NUMERICAL TESTS OF THE LONG-RANGE RADIATION-PRESSURE MODEL

The model we introduce in § 2.1.5 for the treatment of long-range radiation pressure forces requires several simplifying assumptions, in lieu of the ability to perform full on-the-fly radiation hydrodynamics with dust. In this Appendix, we test these assumptions in detail to calibrate our simplified model.

A1 Calibration of the Model

First, we wish to check whether our calculation returns a reasonable approximation to the correct column densities and extinction of each star particle, and the corresponding rate at which the stellar momentum couples to the gas.

We estimate the line-of-sight extinction of sources with our local column density estimator defined in Equation 6, which uses the local density and density gradient. If the column is dominated by gas close to the sources, this should be a good approximation to the true column towards incident gas particles. Figure A1 compares this estimator to the exact line-of-sight column density integrated between each source and every gas particle in the simulation. We calculate the latter in post-processing at a given instant, integrating over the full simulation gas distribution. The top panel in Figure A1 compares the distribution of columns towards all sources, while the bottom panel shows the fraction of column density ratios (local estimate/true) averaged over all sources. The results Figure A1 are for our “standard” (all feedback enabled) HiZ model at a random time once the disk is in quasi steady-state, but the results are similar at all times and in the other simulations (modulo the absolute value of the typical columns). We focus on the HiZ case because it is the simulation where the radiation pressure has the largest effect, and therefore is most sensitive to any errors in the model.

The two methods yield quite similar column density distributions. The local estimator yields a slightly broader and more uniform distribution, which is expected since it introduces some errors that broaden the distribution. This is evident in the distribution of $N_H(\text{estimated})/N_H(\text{true})$, which has a relatively narrow Gaussian core. The dispersion in that distribution is reassuringly small – a factor of ≈ 2 – and most important the mean value is about unity. The biggest difference appears at very low columns: below $N_H \sim 10^{20} - 10^{21} \text{ cm}^{-2}$, there is a comparable column contributed from passing through almost any part of a typical galaxy disk, so the “true” columns are likely to have contributions from large radii that are not accounted for in our local estimator. This is manifest as the non-Gaussian “tail” towards lower $N_H(\text{estimated})/N_H(\text{true})$. However only a relatively small fraction of the stellar luminosity ($\sim 10 - 20\%$) samples this tail in the distribution.

If we consider all sources by age separately, the youngest stars tend to have the highest local column densities, and therefore be most accurately approximated by our local column estimator. This is because they tend to be located in the sites of star formation (near dense gas) and often have not cleared away all of the surrounding gas and dust with feedback. If we repeat the comparison in Figure A1 for “old” stars with age $> 10^7$ yr ($> 10^8$ yr), we find a median $N_H(\text{estimated})/N_H(\text{true})$ of ~ 0.7 (~ 0.5), a scatter of a factor ~ 4 (~ 10). This is because the older stars, having cleared

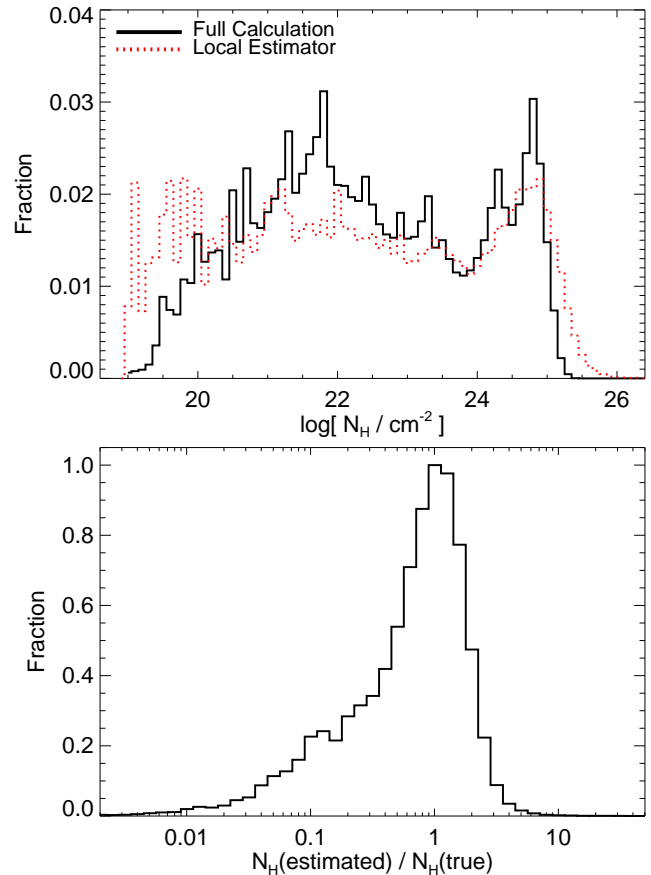


Figure A1. *Top:* Distribution of column densities between all sources (stars) and absorbing gas particles in a standard (all feedback enabled) HiZ simulation. We compare the columns estimated using the local on-the-fly estimator used in real time in the code (based on the local density and density gradient) and that from a full (post-processing) integration over the gas distribution between all stars and gas. The differences in time are minimal. The HiZ model is shown because it is most sensitive to radiation pressure, but the other models are qualitatively similar. *Bottom:* Distribution of the ratio $N_H(\text{estimated})/N_H(\text{true})$ averaged over all sources (weighted by their contribution to the bolometric luminosity). The local estimator we employ provides a good approximation to the true columns, with an accurate mean and factor ~ 2 scatter. This is because columns tend to be dominated by gas near each star. The largest errors occur at the lowest columns, which tend to have comparable contributions from gas at much larger radii (this gives the “tail” in the lower panel), but these tend to be older stars that are no longer in gas-rich star-forming regions, and so contribute only $\sim 10\%$ of the luminosity.

away the dense gas from which they formed, can have larger contributions to the column from gas at very large distances. In principle, we could adopt an age-dependent “fudge factor” to account for this, but this introduces a number of additional uncertainties. In practice, since the older stars contribute fractionally less to the total luminosity especially in the UV, which is the band most sensitive to the column density estimator, this does not introduce much bias in the luminosity-weighted N_H distribution. As a result, the effect on the actual momentum coupled is small.

Figure A2 shows the consequences of our local estimator for the emergent SED and the typical SED seen by each gas particle. First, consider the emergent spectrum. Using the SUNRISE code (Jonsson 2006), we can calculate the emergent spectrum from the galaxy along a large number of sightlines, uniformly sampling

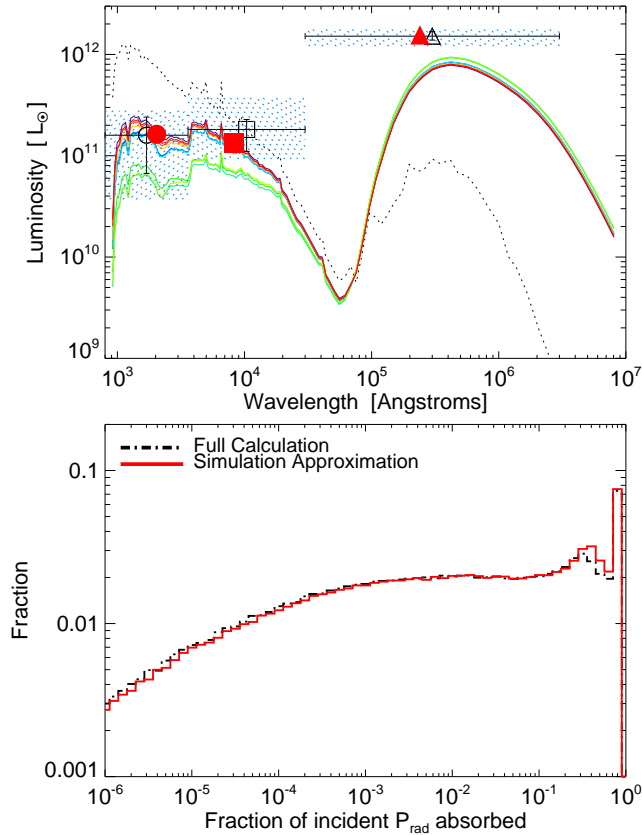


Figure A2. *Top:* Comparison of the emergent SED estimated with the on-the-fly simulation approximations and a full radiative transfer calculation using the SUNRISE code. For the same HiZ snapshot as Figure A1, we plot the full emergent spectrum (plotted as λL_λ) calculated with RT (solid lines); we show 10 of random sub-sampled sightlines). For comparison, the spectrum without any attenuation is shown as the black dotted line. Integrating over our three wavelength intervals (UV/Optical/IR), the resulting integrated luminosity is shown (open black points; circle/square/triangle for UV/Optical/IR, respectively) with horizontal error bars showing the wavelength range of integration and vertical error bars showing the $\pm 1\sigma$ range across all sightlines. Red filled points show the average luminosity in each band estimated using the simulation approximations. Shaded blue areas show the $\pm 1\sigma$ observed range of luminosities in each band, for observed galaxies with the same bolometric luminosity. The local approximation predicts fluxes in each band within the 1σ range of sightlines from a full RT calculation; both agree well with the observed “average” SEDs of galaxies with similar SFR. *Bottom:* Distribution of coupled momentum (specifically, distribution across all gas particles of the radiation pressure momentum absorbed relative to the incident flux, which depends on the SED shape and opacities). We compare the simulation approximation and results again from a full RT calculation. The two distributions agree to within $\sim 10\%$.

the sightlines to e.g. gas particles outside the disk. We do so using the exact same assumptions as in our simplified model about the scaling of dust-to-gas ratio with metallicity and emergent SED from all star particles as a function of age and metallicity from STARBURST99. Figure A2 shows these results (as well as the unprocessed spectrum) for a random subset of ten sightlines. Again, this is prohibitive to calculate in real-time, so we do so in post-processing for the same snapshot considered in Figure A1. Next, recall that we simplify our calculation in the radiation pressure by integrating over three frequency ranges L_{UV} ($\lambda < 3600\text{\AA}$), L_{Opt} ($3600\text{\AA} < \lambda < 3\mu$) and L_{IR} ($\lambda > 3\mu$). We therefore integrate the emergent SUNRISE spectra over each range, and plot the result-

ing median luminosity in each range as well as its dispersion (here $14 - 86\%$ intervals).

Figure A2 also compares this ‘exact’ SED calculation to the approximate result given by our local estimator. Specifically, using the results from STARBURST99 to estimate the initial L_{UV}/L_{Opt} for each star particle, we attenuate each according to the local column density estimator calculated for the particle (eqn. 5) and assume all of the absorbed energy in each of the UV and optical ranges is re-radiated as L_{IR} . The resulting SED agrees well with the full radiation transfer calculation; at all wavelengths it is within the 1σ sightline-to-sightline scatter of the full calculation, and generally within a factor of < 2 of the mean in each waveband. In the IR, which contains most of the energy, the accuracy is much better, $\sim 10\%$ (the largest uncertainties come when the net attenuation is very large). It is important to compare these theoretical fluxes to those measured in similar observed galaxies. In § A3 below, we discuss a variety of observational constraints on the fraction of the luminosity observed to escape in the UV/optical/IR, for galaxies of similar bolometric luminosity and/or SFR to the HiZ model considered here. From the references discussed there, we estimate an average empirical SED shape (shaded blue bands in Fig. A2), which is reasonably consistent with the model predictions.

Given the agreement in the emergent SED, we would expect the local model to reasonably capture the stellar momentum that couples to the gas. Figure A2 tests this explicitly. For the same simulation, we use the full radiative transfer results to calculate (in post-processing at a given instant) the net momentum deposition from radiation absorbed in each gas particle (using the full spectrum and dust opacity curve). We compare this to the actual coupled momentum using the simulation code approximations. Since we already know the total photon momentum is the same in either case, it is convenient to normalize the absorbed momentum by the incident momentum flux. This then tests whether the differences in emergent spectral shape (from our local column estimator), and the approximation of three wavebands instead of a full spectrum, as well as neglect of re-radiation changing the spatial distribution of emission on kpc scales, ultimately make a difference to the coupled momentum. Figure A2 shows that the differences are small, at the level of tens of percent. This is smaller than the systematic uncertainties in our method (e.g., dust properties, unresolved clumping).

A2 The Effects of Photon “Leakage”

One subtle complication is that the ISM is probably inhomogeneous on small scales well below what we model. In principle, that can allow photons to “leak out” from the region around their parent star at a rate much higher than the nominal $\exp(-\tau_0)$ expectation which we use above to estimate the attenuated spectrum. In Paper I we discuss how this leakage in the IR can affect the short-range radiation pressure term (and show the effects are generally small for the cases modeled here). Here, the question is how this might modify the initial attenuation of optical and UV photons used to treat the long-range radiation pressure forces.

If a medium with mean opacity τ_0 has a “true” column density distribution $P(\tau|\tau_0)$ across all sightlines, then the escape fraction is just

$$f_{\text{esc}} = \int \exp(-\tau) dP(\tau|\tau_0). \quad (\text{A1})$$

Fortunately, in Paper I we show that we can make a reasonable estimate of $dP(\tau|\tau_0)$. In ultra-high resolution simulations, we calculate $dP(\tau|\tau_0)$ with ~ 1000 lines-of-sight for each molecular cloud,

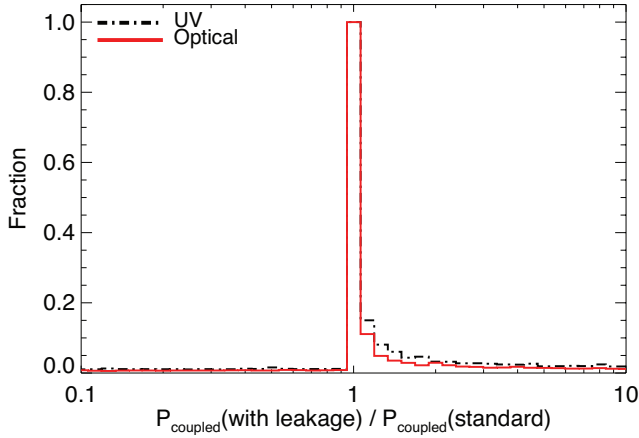


Figure A3. Effects of allowing for photon “leakage” – i.e. assuming that the ISM is clumpy and porous on sub-resolution scales. We plot the ratio of coupled momentum from the UV and optical wavebands – the distribution of this quantity is measured over all gas particles for a given instant in the same HiZ simulation. The “standard” model takes the local column density estimator as-is, and estimates the escape fraction from the spectrum of each star with $f_{\text{esc}} = \exp(-\tau)$ for each waveband. The “with leakage” model assumes that each star is actually surrounded by an (un-resolved) distribution of columns following Equations A1-A3 and uses this to calculate f_{esc} . The allowance for leakage only makes a difference when the average opacity is large, at which point the contribution (in either case) to the global total luminosity in the relevant band is small. As a result it has a negligible effect on our results.

and find the resulting column density distribution (per cloud) can be well-approximated with a near-universal function

$$dP(\tau|\tau_0) \approx \frac{1}{2\sigma} \exp\left(-\frac{|\ln(\tau/\tau_0)|}{\sigma}\right) \frac{d\tau}{\tau} \quad (\text{A2})$$

with $\sigma = 0.25 - 1.0$ (median 0.5). This is also similar to the distribution estimated in even higher resolution simulations of individual GMCs and sub-cloud clumps (see Ostriker et al. 2001), and to observational estimates (Wong et al. 2008; Goodman et al. 2009). If the ISM is self-similar, then for any given τ_0 the true τ distribution is given by the function above; we then solve for f_{esc} :

$$f_{\text{esc}} = \frac{\tau_0^{-1/\sigma}}{2\sigma} \left[\tau_0^{1/\sigma} E_{1+1/\sigma}(\tau_0) + \Gamma\left(\frac{1}{\sigma}\right) - \Gamma_{1/\sigma}(\tau_0) \right] \quad (\text{A3})$$

where the E and Γ are incomplete exponential integral and Gamma functions. The exact functional form, however, is not important: the behavior is simple in two limits. For $\tau_0 \ll 1$, this function is very close to $\exp(-\tau_0)$, since most sightlines are optically thin (actually $f_{\text{esc}} \rightarrow \exp(-\tau_0/[1 - \sigma^2])$, a slightly *lower* value, owing to the presence of some dense sightlines). For $\tau_0 \gg 1$,

$$f_{\text{esc}} \rightarrow \frac{1}{2} \Gamma[1 + \sigma^{-1}] \tau_0^{-1/\sigma} \quad (\text{A4})$$

i.e. the escape fraction declines as a power-law $\propto \tau_0^{-1/\sigma}$, rather than as an exponential $\exp(-\tau_0)$. This is straightforward to understand – f_{esc} in this limit is essentially just the fraction of sightlines which are optically thin.

Figure A3 shows the effects of replacing $f_{\text{esc}} = \exp(-\tau_0)$, our usual estimator of attenuation, with this modified f_{esc} , in the HiZ simulation. We specifically show the distribution of coupled momentum on all gas particles from the UV and optical wavebands. There is no significant difference. The reason is simple. For intermediate or low τ_0 , the escape fractions are large and very similar regardless of sub-structure. For high τ_0 , they can be very dif-

ferent, but they are both still very small. At $\tau_0 \sim 100$ (common for the optical opacities in dense star-forming regions), for example, the power-law f_{esc} is much larger than $\exp(-\tau_0)$, but is still $\sim 10^{-7} - 10^{-4}$ (for $\sigma = 0.25 - 0.5$), so the amount of escaping optical light is still totally negligible compared to gravity. In short, the total UV/optical light seen by a given gas particle tends to be dominated by the stars that have low τ_0 (even if they are rare), not by the small leakage from stars with high τ_0 . For the same reasons, repeating the experiment above but with a log-normal distribution assumed for $dP(\tau|\tau_0)$ (instead of the power-law distribution above) also makes no difference.

A3 Comparison to Purely Empirical SED Models

The average SED shape as a function of galaxy star formation rate or bolometric luminosity is well-studied (see e.g. Cortese et al. 2006; Iglesias-Páramo et al. 2006; Buat et al. 2007; Reddy et al. 2008; Sargsyan & Weedman 2009; Noll et al. 2009; Takeuchi et al. 2010). Specifically, using the relations in Cortese et al. (2006) between L_{UV} , L_{IR} , and H -band luminosity, with the same templates discussed therein to make the (small) correction between their wavebands and ours, we expect a typical luminosity fraction in each interval (f_{UV} , f_{Opt} , f_{IR}) equal to (0.05, 0.2, 0.75) for the HiZ, (0.13, 0.40, 0.47) for the MW, (0.3, 0.3, 0.4) for the SMC, and (0.07, 0.23, 0.7) for the Sbc models. We stress that all of these values have factor $\gtrsim 2$ scatter even in narrowly-selected galaxy samples. This SED is shown for the HiZ model in Figure A2. Although the Cortese et al. (2006) sample is low-redshift, a similar result is obtained if we consider the high-redshift relation studied in Reddy et al. (2008). The shaded range in Figure A2 corresponds to the empirical scatter in the luminosity at each band at fixed L_{bol} (estimated as the 14 – 86% interval from the observed samples). The observed SED shape agrees well with the integrated fractions predicted by our models and the more detailed radiative transfer calculation. We find similar agreement for each of the other galaxy models as well.

One way we can test our long-range radiation pressure model is to calculate the bolometric luminosity and incident force on gas as in § 2.1.5 but to specify the SED shape of each star particle (the emergent $L_{\text{UV}}/L_{\text{Opt}}/L_{\text{IR}}$), to be a constant determined by the observed integral values for each galaxy model. This will of course gloss over spatial and temporal differences in the SED shape, but it has the advantage that we can directly take the SED motivated by observations for all “typical” particles.

In Figure A4 we compare the star formation history for each of our standard galaxy models to such a calculation with a fixed attenuated SED. It is reassuring that the results are similar. Of course, this is not that surprising given that the predicted SED (f_{UV} , f_{Opt} , f_{IR}) from our simple attenuation model is similar to those observed in each galaxy type. Moreover, since the acceleration by the diffuse stellar radiation is primarily important only for gas that is out of the midplane, it turns out not to be a very bad approximation to assume that the typical particle sees much the same spectrum that the typical observer would see.

For contrast, we also compare in Figure A4 the results if we were to enforce a uniform SED shape with a higher UV/optical fraction than is actually observed – which will substantially boost the coupled momentum. For the HiZ, Sbc, and MW models, this serves to dramatically suppress the SFR (especially at late times, because more of the gas is blown out of the disk in a wind). The SMC however is sufficiently low-luminosity that this has only a weak effect. This comparison highlights at least two important points. First, on large scales, systems are generally not optically

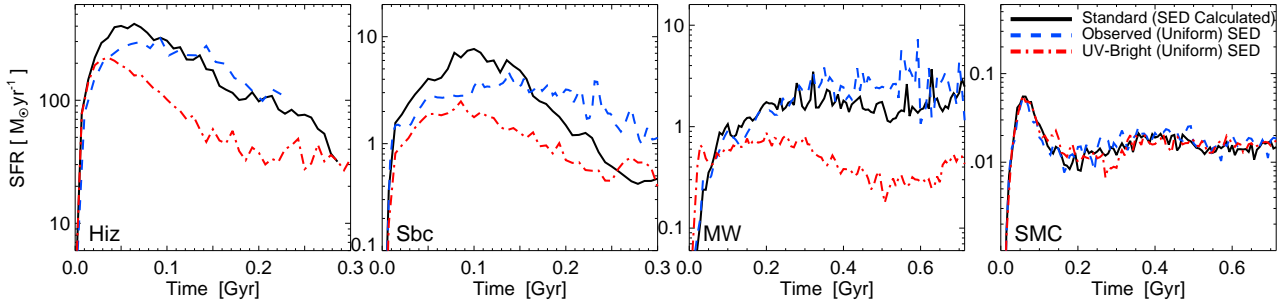


Figure A4. Comparison of our standard long-range radiation pressure model (where the attenuation and SED shape of each star particle is calculated) to one in which we simply force the SED shape to match a specific empirical template. We show the resulting SFR versus time (as Figure 7) for each of the HiZ/Sbc/MW/SMC models. In each, we compare our standard model (black) in which the SED shapes are self-consistently calculated on-the-fly, to a model where the SED shape (L_{bol} is still determined self-consistently) is forced to a constant fixed value chosen to match the observed mean SED shape for similar observed galaxies to each model (blue). These choices correspond to a relative proportion of L_{bol} in the UV/optical/IR bands of (0.05, 0.2, 0.75), (0.07, 0.23, 0.7), (0.13, 0.4, 0.47), (0.3, 0.3, 0.4) for the HiZ/Sbc/MW/SMC cases. In each case, the self-consistent and empirically fixed models give SFRs in reasonable agreement; this is because the emergent SEDs calculated with the full models tend to agree well with the typical observed values (Figure A2). However factor $\lesssim 2$ differences do arise, largely because the empirical model does not allow spatial and/or time-dependent variations in the emergent SED (for example, very young stars in the galaxy nucleus tend to be much more obscured than older stars in the galaxy outskirts). We also compare a model with fixed UV/optical/IR fractions, but much higher UV/optical fractions than actually observed (red): (0.25, 0.3, 0.45) for the HiZ/Sbc/MW cases and (0.4, 0.4, 0.2) for the SMC. This artificially boosts the long-range radiation pressure, and significantly suppresses the SFR in the HiZ/Sbc/MW models (the effect is weak in the SMC case, because radiation pressure is relatively unimportant). Accounting for attenuation changing the SED shapes and consequently radiation pressure is critical; but small differences between empirical values and our simulation values are not dominant uncertainties in the model.

thick in the IR and so, unlike inside of GMCs, it is the UV/optical photons that tend to be absorbed and provide the radiation pressure force, so it is important that any model be able to reasonably approximate the average attenuation around stars in a self-consistent manner. Second, if there are times when dust obscuration is relatively weak, for example at very high redshifts (owing to low metallicities) or perhaps after phases of strong AGN feedback (either the AGN blowing away or dissociating the dust), then the long-range radiation pressure from stars can be dramatically boosted (even while the short-range effects are weakened), enhancing global outflows. Since this in turn removes more material, there is the possibility of unstable runaway that could substantially enhance quenching in such systems.

APPENDIX B: RESOLUTION & CONVERGENCE TESTS

In Figure B1, we perform a spatial and mass resolution test for our HiZ simulation. We compare low, intermediate, standard, and high-resolution simulations of otherwise identical HiZ runs with all feedback enabled.¹³ We also compare, at low resolution, two additional runs with the same mass resolution but force resolution varied by a factor of ≈ 5 . The star formation history converges reasonably quickly; the differences at the peak of the SFR are small even at low resolution. This is expected and discussed in detail in Paper I; since the equilibrium SFR is feedback-regulated, set by the balance of momentum injection with dissipation, it depends primarily on integral quantities (the total momentum injection $\propto L \propto \dot{M}_*$, approximately). As a result, it converges relatively quickly. In all cases, the higher-resolution runs begin to rise in SFR (and generally converge to their equilibrium structure) slightly earlier – this simply owes to

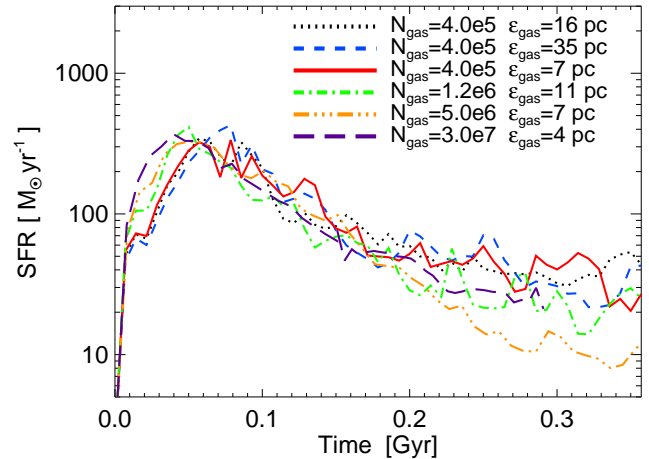


Figure B1. Resolution tests. We plot the SFR vs time as Figure 7. We consider a “standard” (all feedback enabled) HiZ model at a series in mass and force resolution (N_{gas} is the number of gas particles in the star-forming disk, which determines the mass resolution; ϵ_{gas} is the force softening). The SFR converges quickly because it depends on the integral constraint of momentum feedback ($\propto L \propto \dot{M}_*$) balancing gravity (differences at late times owes to more efficient winds at higher resolution). Recall, the Jeans length in these galaxies is several hundred pc (Jeans mass $\gtrsim 10^8 M_{\odot}$), so *all* of these models formally resolve the Jeans scales. At lower resolution, our prescriptions do not have clear physical meaning.

the fact that the most rapidly collapsing spatial scale resolved is on a smaller timescale as we go to higher resolution. At late times, the higher-resolution simulations have a slightly lower SFR; this owes to their blowing slightly more efficient galaxy-scale outflows.

¹³ For technical reasons to ensure quantities such as random number generation were identical in these runs, this set was run on the same set of processors and so does not overlap with our standard HiZ run shown earlier; but the results from that run are completely consistent with the standard-resolution case here.